NATIONAL ACADEMY OF SCIENCES OF THE REPUBLIC OF ARMENIA

INSTITUTE OF RADIOPHYSICS AND ELECTRONICS

Galstyan Ogsen

MAGNETO-OPTICAL THIN FILMS FOR MAGNETIC FIELDS VISUALIZATION

PhD Thesis

Applying for the competition of scientific degree of candidate of Phys.-Math. Science on specialty A.04.03-Radiophysics

Scientific supervisor

Doctor of Phys.-math. Sci., corr. member of NAS RA

A. A. Hakhoumian

ASHTARAK – 2015

CONTENT

INTRODUCTION

This dissertation is dedicated to the blessed memory of my father.

The theme actuality

Humans start the process of perception of the world from the very first moment of their lives. To understand the environment we use our sense organs: eyes, ears, tongue, skin, and nose. Human eye is an optical instrument which reacts to the light and converts it to the electro-chemical impulses in neurons. The range of wavelengths that can be detected by human eye is about 390 to 700 nm. All kinds of radiations outside of this spectrum are invisible for a naked eye. To overcome the problem of a "naked eye" and examine our environment people invented different kind of equipment and tools which give us an opportunity to see "invisible" things such as: electric and magnetic fields.

In 1845 Michael Faraday discovered that a light and magnetic field can interact in an interesting way in a particular medium. This effect is called Faraday effect (FE) [1]. The plane of linearly polarized light is rotated in a magneto-optical medium when a magnetic field is applied parallel to the propagation direction of a light. This phenomenon is a basis for a magneto-optical imaging (MOI) technique, which is a nondestructive and label-free evaluation technique to visualize magnetic fields induced by specimen under test (SUT) with high contrast and high spatial resolution.

For the visualization of magnetic fields several techniques have been used, such as magnetic force microscopy (MFM) [2], superconducting quantum interface device (SQUID) microscopy [3], Hall effect sensors [4] and magneto-resistive sensors [5]. In comparison with mentioned methods MOI technique has several advantages, such as: easy experimental setup, fast measurement and a wide range of operating temperature. The design, imaging performance and applications of MOI for noninvasive characterization of different kinds of SUT will be described further.

The MOI technique has attracted considerable attention as a sensor platform for use in monitoring of electronic devices [6], imaging of magnetic domains and magnetic fields

distribution in different SUT [7], inspecting the surface and subsurface defects in metallic specimens [8], detection of magnetic vortex phenomenon in superconductors [9] and etc. Recent advances in research of magnetics have revealed a possibility of a new technology using an electron spin as an information carrier. This gives the idea of a new emerging field of spintronic equipment, which are anticipated to be the next generation devices. There are publications which show that spin transport and spin Hall effect can be visualized using MOI [10, 11]. Thus in future MOI can be a great tool for the monitoring of spintronic devices.

In MOI systems magneto-optical mediums are used as indicator thin films. The sensitivity and quality of the MOI directly depends on the characteristics of indicators. The most important parameters of thin films which are required for the enhancement of the sensitivity of MOI are the following: high Faraday rotation (FR) angle, low optical absorption, in-plane magnetic anisotropy and appropriate thickness of films which can increase FR and decrease transmittance of a light through it at the same time. Due to a high dynamic response of indicator thin films (less than 10^{-9} seconds) MOI technique can be used for real time magnetic field visualization. One of the most desired materials which can be used for the preparation of indicators in MOI is yttrium iron garnet (YIG or $Y_3Fe_5O_{12}$) and its substituted structures such as bismuth substituted yttrium iron garnet (Bi-YIG or $Bi_xY_{3-x}Fe_5O_{12}$).

In the scope of this research we focus on the ways to find easy implementation routes to prepare magneto-optical thin films with highest possible FR, which in result enhances the sensitivity of MOI system. There are several methods to prepare magneto-optical thin films, such as: liquid phase epitaxy (LPE) [12], the sputtering method [13], pulsed laser deposition (PLD) [14], the sol-gel method [15], metal-organic chemical vapor deposition method (MOCVD) [16] and the metal-organic decomposition method (MOD) [17]. For a synthesis of films we used the MOD method because it is inexpensive, simple and allows us to have a precise control on the composition of the MOD solution and the formation over the large area.

As it will be shown MOD is a promising method for the garnet thin films and yttrium orthoferrite (orthorhombic and hexagonal) thin films preparation on amorphous glass substrates because it does not require high temperatures or long time annealing to produce the desired materials. Our results indicate, that particularly for yttrium orthoferrite films, it becomes possible

to crystallize an orthorhombic phase of yttrium orthoferrite by substitution of yttrium with appropriate concentration of bismuth. This class of materials are considered to be very unique because of their magneto-optical and photocatalytic applications.

The goals of this work are the following:

1. On the basis of MOD method develop technology for the preparation of $Bi_xY_{3-x}Fe_5O_{12}$ thin films. Investigate structural and magneto-optical properties of prepared films.
2. Investigate the possibility of preparation of magneto-optical thin films with high Faraday rotation angle on glass substrates using MOD method.
3. Investigate magneto-optical properties of $Bi_xY_{3-x}Fe_5O_{12}$ thin films grown on amorphous glass substrates and use these films to develop experimental setup for the visualization of magnetic fields.

The scientific novelties of this thesis are the following:

1. We found that pre-crystallization step in a heat treatment schedule of MOD process can improve structural and magneto-optical properties of thick Bi-YIG films.
2. We found appropriate synthesis conditions and heat treatment schedules for the fabrication of $Bi_xY_{3-x}Fe_5O_{12}$ (x=1, x=2, x=2.5) indicator films with different concentrations of substituted Bi on amorphous glass substrates using MOD method.
3. For the first time magnetic fields were visualized using $Bi_2Y_1Fe_5O_{12}$ indicator films, prepared directly on amorphous glass substrates by MOD method using low post-annealing (620 °C) temperatures.
4. We were the first to report the preparation of yttrium orthoferrite thin films on glass substrates by MOD method using low crystallization temperature.

Scientific and practical values of implemented investigations are the following:

1. We developed MOI system is an inexpensive and easily applicable experimental tool for the visualization of magnetic fields with 0.6 Oe sensitivity and 0.5 μm range spatial resolution.
2. The method of preparation of Bi-YIG and orthoferrite thin films on amorphous glass substrates can be widely applied in magneto-optics, electronics, microwave devices and spintronics.

The main scientific provisions of the work are the following:

1. Pre-crystallization process is crucial for the preparation of high quality Bi-YIG thick films by MOD method.
2. The FR of Bi-YIG thin films with high level of bismuth substitution could be increased by the lowering temperature of post-annealing process.
3. $Bi_2Y_1Fe_5O_{12}$ indicator films with high magneto-optical figure of merit (FOM) can be prepared directly on amorphous glass substrates using low crystallization temperatures.
4. The selective crystallization of an orthorhombic (o-$YFeO_3$) or (h-$YFeO_3$) phases of $Bi_xY_{1-x}FeO_3$ yttrium orthoferrite thin films can be obtained by adjusting the level of Bi substitution.

Approbation of the results:

The principal statements and results of the dissertation are discussed in seminars of Signal processing and UHF devices laboratories of Institute of Radiophysics and Electronics of NAS RA, UHF Radiophysics and Telecommunications Chair in Yerevan State University, in Microwave Photonics Laboratory in Sogang University and presented in IRPhE 2014 (2-3 october, Aghveran, Armenia) conference.

Published papers:

There have been published 6 papers on the topic of thesis. 5 in international scientific journals and 1 proceeding of international conference.

Structure and volume of the dissertation:

The dissertation work includes: an Introduction, 3 Chapters, Conclusion, and References. It consists of 100 pages including 58 figures, 4 tables, and 100 references.

CHAPTER 1. THEORETICAL BACKGROUND. FARADAY EFFECT.

§1.1. Magneto-optical effects.

FE was the first magneto-optical effect to be observed. This effect confirmed the electromagnetic nature of light. FE was discovered in a heavy flint glass and has since been observed in water, quartz and several gases. Comparing to other materials, it is several times stronger for ferromagnetics. In case of ferromagnetic materials magneto-optical effects can even appear without applying an external magnetic field. FE has been observed not only for optical frequencies but also for microwave and radio frequencies. Figure 1.1.1 shows schematic diagram of FE when linearly polarized light propagates through magneto-optical medium.

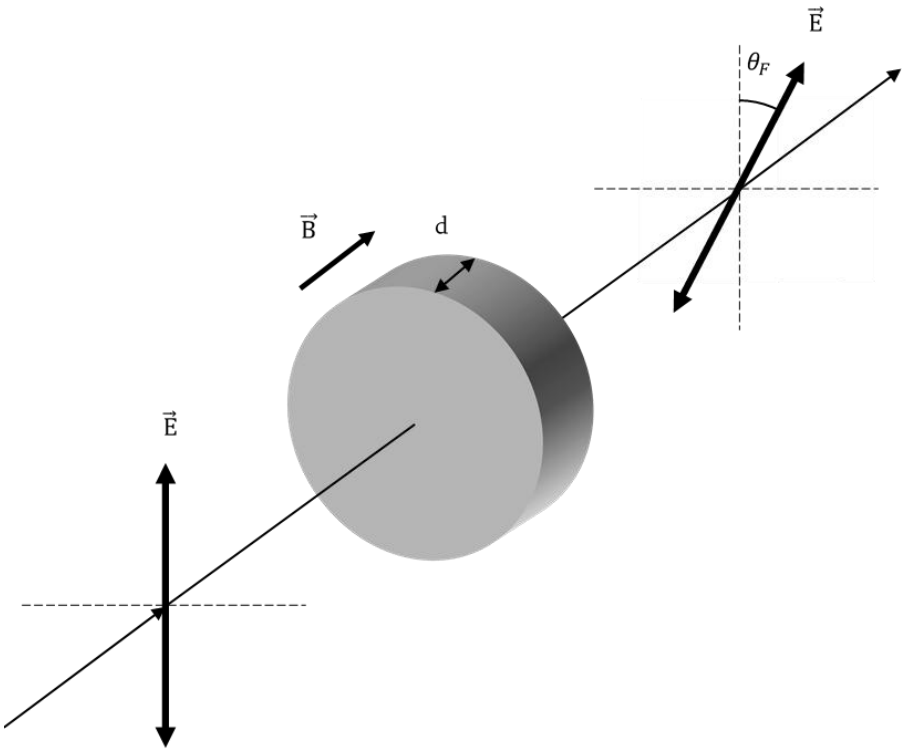

Figure 1.1.1*. FE taking place when linearly polarized light propagates through a medium which is magnetized along the propagation direction of light.* $\vec{E}$ *- Electric field of a light,* $\vec{B}$ *- Magnetization of a medium, d - the length of a medium,* θ_F *-the FR angle.*

The angle of FR θ_F is given by:

$$\theta_F = VBd \tag{1.1.1}$$

where V is a characteristic of the magneto-optical medium called the Verdet constant. It is a function of the wavelength of propagating light, temperature and refractive index of the material. B-is the magnetization of a medium and d is the path length of the medium. In other words V is the rotation per unit path length per unit applied magnetic field.

Later in 1888 Kerr discovered a similar effect. When linearly polarized light reflects from the surface of a magnetized medium the polarization vector of light rotates. Both the magneto-optical Kerr effect and magneto-optical FE provide the possibility to develop powerful tools for optical monitoring of the state of magnetization of different samples. Depending on the direction of magnetization to the surface of a magneto-optical medium, there are 3 geometries of a magneto-optical Kerr effect: polar, longitudinal and transverse. Figure 1.1.2 shows different geometries of a magneto-optical Kerr effect.

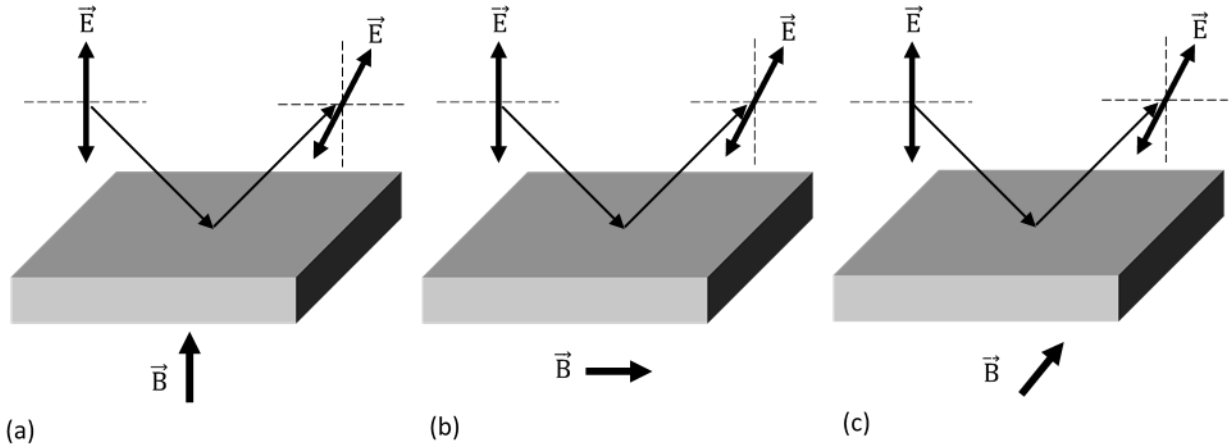

Figure 1.1.2. *Magneto-optical Kerr effects taking place when linearly polarized light is reflected from the surface of a medium which magnetization is in one of 3 directions. (a) represents polar configuration of Kerr effect, (b) longitudinal and (c) transverse.* $\vec{E}$ *- Electric field of a light and* $\vec{B}$ *- Magnetization of a medium*

In 1902 German physicist W. Voigt discovered that birefringence take place (Voigt effect) when light is passing through a vapor and magnetic field is applied perpendicularly to the

propagation direction of a light. The main difference between FE and Voigt effect is that FE depends linearly on applied magnetic field, while Voigt effect is quadratic. When a liquid plays the role of a medium in case of vapor the effect is much stronger and is known as the Cotton-Mouton effect.

It is worth to mention that the phenomenon of rotation of the polarization vector was first observed by D. Arago in 1811. He discovered that the polarization vector rotated when light propagated through quartz in the direction parallel to optical axis. This property of quartz is called natural optical activity. The most important difference between optical activity or the FE in the optically active materials and magneto-optical FE is the following: in case of magneto-optical FR the effect is non-reciprocal, which means that for the propagation in the direction of magnetic field and in the opposite direction the plane of the polarization rotated at the same direction in result FR is doubled, while for optical activity, on the other hand, the resulting rotation is canceled [18].

Another interesting magneto-optical effect which was demonstrated by Kimel *et al.* in Ref. [21] can be applied for the manipulation of the spins by circularly polarized light. It is predicted that this study can open the way for the ultrafast laser-controlled magnetic writing process. A static magnetization $\vec{M}(0)$ can be induced by the high intensity laser radiation (inverse Faraday effect (IFE)):

$$\vec{M}(0) = \frac{x}{16\pi}[\vec{E}(\omega) \times \vec{E}^*(\omega)] \qquad (1.1.2)$$

where $\vec{E}(\omega)$ and $\vec{E}^*(\omega)$ are the electric field of the induced light wave and its complex conjugate, x is the magneto-optical susceptibility. Figure 1.1.3 shows that (IFE) induces magnetization δH and even can flip the polarization direction of a spin. This study demonstrates that it is possible optically, by choosing polarization state of a pump laser pulse, control spin oscillations in magnetic materials such as $DyFeO_3$ rare-earth orthoferrite. This kind of findings once again show the importance of research in the field of magneto-optics and magnetic materials.

Most of the magneto-optical effects are direct or indirect outcomes of Zeeman effect. Zeeman effect is the splitting of energy levels in an external or spontaneous magnetic field. When magnetic field is parallel to the symmetry axis of a material, relative difference of dispersion

between right circularly polarized light (RCP) and left circularly polarized light (LCP) take place because of Zeeman effect. This causes the magneto-optical phenomenon such as FE. On the other hand in ferromagnetic materials FE is 100-1000 times bigger comparing to the diamagnetic materials. This is explained by the spin-orbit interaction which is much stronger than Zeeman splitting [19,20]. Therefore, it is desirable to use transparent ferromagnetic materials in magneto-optical applications, since these materials have high magneto-optical activity. That's why most of our research was devoted to the preparation and characterization of two different type of ferromagnetic materials: rare-earth iron garnets and rare-earth orthoferrites. In both materials increase of FE is assigned to spin-orbit interactions. In the following paragraphs we will present theoretical explanations of FE for the magnetic materials.

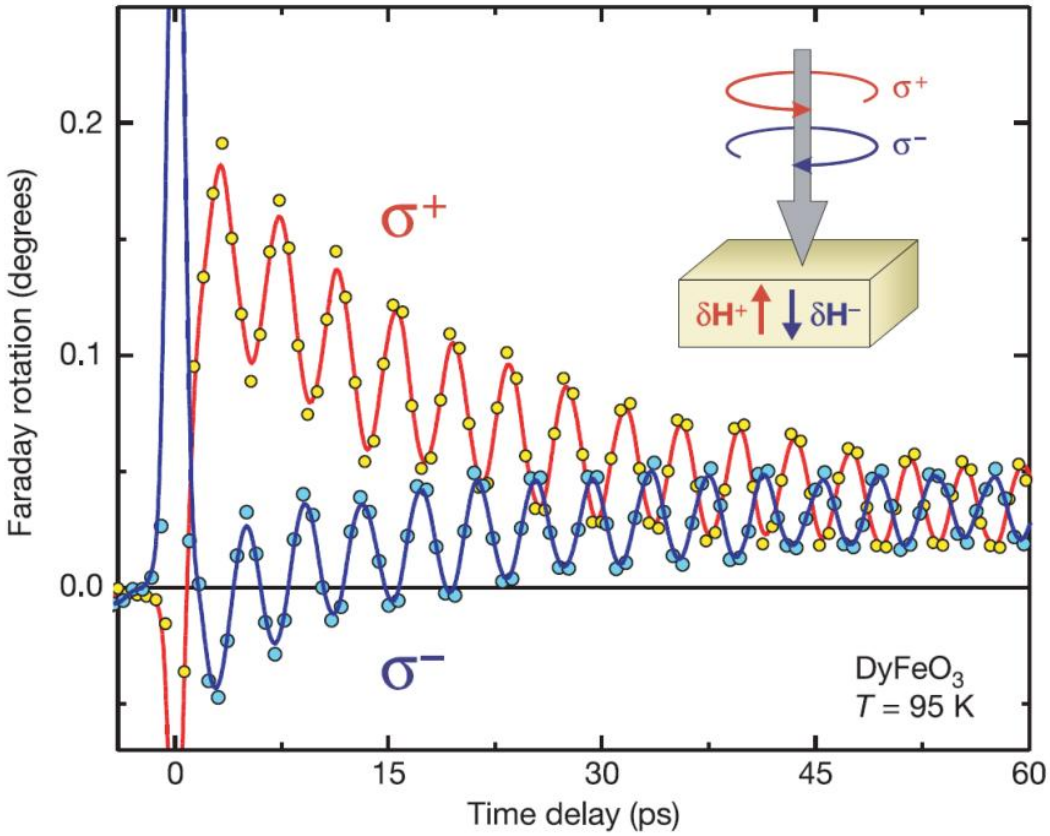

Figure 1.1.3. *Magnetic excitations in $DyFeO_3$ probed by the magneto-optical Faraday effect. Vectors δH^+ and δH^- represent the effective magnetic fields induced by RCP - σ^+ and LCP - σ^- pumps, respectively [21]. There are two effects that can be clearly seen, one is the change of the FR and depending on the time value of FR oscillates which can be assigned to the oscillations of the magnetization. This results also very important because of non-thermal control of magnetization.*

§1.2. Theory of Faraday effect

In this paragraph we will derive FR equation, depending on the elements of the dielectric tensor of a magneto-optical medium such as a YIG. We mainly used theoretical and phenomenological descriptions which also can be found in Ref. [19, 22-25]. The same theoretical model, which will be presented for the FE, can be applied also for the magneto-optical Kerr effect.

First let's formulate the problem. Linearly polarized electromagnetic wave propagating through a dielectric material under the influence of external magnetic field changes its state of a polarization after exiting the medium. To solve this kind of a problem one needs to start with Maxwell equations written in a general form:

$$\nabla \times \vec{H} = \frac{1}{c}\frac{\partial \vec{D}}{\partial t} + \frac{4\pi}{c}\vec{J} \tag{1.2.1}$$

$$\nabla \times \vec{E} = -\frac{1}{c}\frac{\partial \vec{B}}{\partial t} \tag{1.2.2}$$

$$\nabla \cdot \vec{B} = 0 \tag{1.2.3}$$

$$\nabla \cdot \vec{D} = 4\pi\rho_0 \tag{1.2.4}$$

where $\vec{E}$ and $\vec{H}$ are electric and magnetic field intensities respectively, $\vec{D}$ and $\vec{B}$ are electric and magnetic flux densities respectively, ρ_0 electric charge density and $\vec{J}$ electric current density and c is speed of light.

If we assume that material is a linear dielectric then material equations will have a form:

$$\vec{D} = [\varepsilon]\vec{E} \tag{1.2.5}$$

$$\vec{B} = [\mu]\vec{H} \tag{1.2.6}$$

$$\vec{J} = [\sigma]\vec{E} \tag{1.2.7}$$

where $[\varepsilon]$ is the dielectric tensor, $[\mu]$ is the permeability tensor and $[\sigma]$ is the conductivity tensor. In our case we have a propagation of wave in a ferrimagnetic where conductivity is very small because of insulating properties of ferrimagnets so it can be ignored. In the scope of this thesis we are only interested in the FE for optical wavelengths, where $[\mu]$ can be taken equal to unity. For the ferrimagnets the properties of $[\varepsilon]$ can be derived phenomenologically from the considerations of a symmetry. Let's take a coordinate system where a ferrimagnet with a cubic symmetry is

magnetized along the OZ axis. OX and OY directions for the cubic crystal are equivalent. Then for a transparent ferrimagnet $[\varepsilon]$ will be:

$$[\varepsilon] = \begin{pmatrix} \varepsilon & +i\varepsilon_1 & 0 \\ -i\varepsilon_1 & \varepsilon & 0 \\ 0 & 0 & \varepsilon_z \end{pmatrix} \tag{1.2.8}$$

Presence of the external magnetic field or spontaneous magnetization of a medium gives rise to a gyrotropy of a medium, so the non-diagonal ε_1 components of dielectric tensor are not equal to zero. Finally we also assume that there is no free charge built up so $\rho_0 = 0$.

From the system of Maxwell equations (1.2.1-1.2.4) one can solve the wave equation using plane wave approximation and find the values of dielectric tensor elements. Non-diagonal elements related to the refractive indices $n_\pm$ of LCP and RCP lights:

$$n_\pm{}^2 = \varepsilon \pm \varepsilon_1 \tag{1.2.9}$$

From equation (1.2.13) it follows that phase velocities of a propagation of a LCP (V_+) and RCP (V_-) components of linearly polarized light wave are different:

$$V_+ = \frac{c}{n_+} \tag{1.2.10}$$

$$V_- = \frac{c}{n_-} \tag{1.2.11}$$

which in result brings the phase difference between them and plane of the linearly polarized wave will be rotated by the FR angle:

$$\theta_F = \frac{\omega(n_+ - n_-)z}{c} \tag{1.2.12}$$

To sum up, FR is the phase difference between the RCP and LCP components of a linearly polarized wave. Fig. 1.2.1 shows that linearly polarized light can be represented as a sum of LCP and RCP lights. So the FR comes from the phase difference of these components of linearly polarized light.

If $\varepsilon \gg \varepsilon_1$ then from equations (1.2.9) and (1.2.12) for the FR dependency from dielectric tensor elements will be:

$$\theta_F = -\frac{\omega\varepsilon_1}{c\sqrt{\varepsilon}} z \tag{1.2.13}$$

So called specific FR[1] which is the FR per medium z thickness will be:

$$\theta_F = -\frac{\omega\varepsilon_1}{c\sqrt{\varepsilon}} \tag{1.2.14}$$

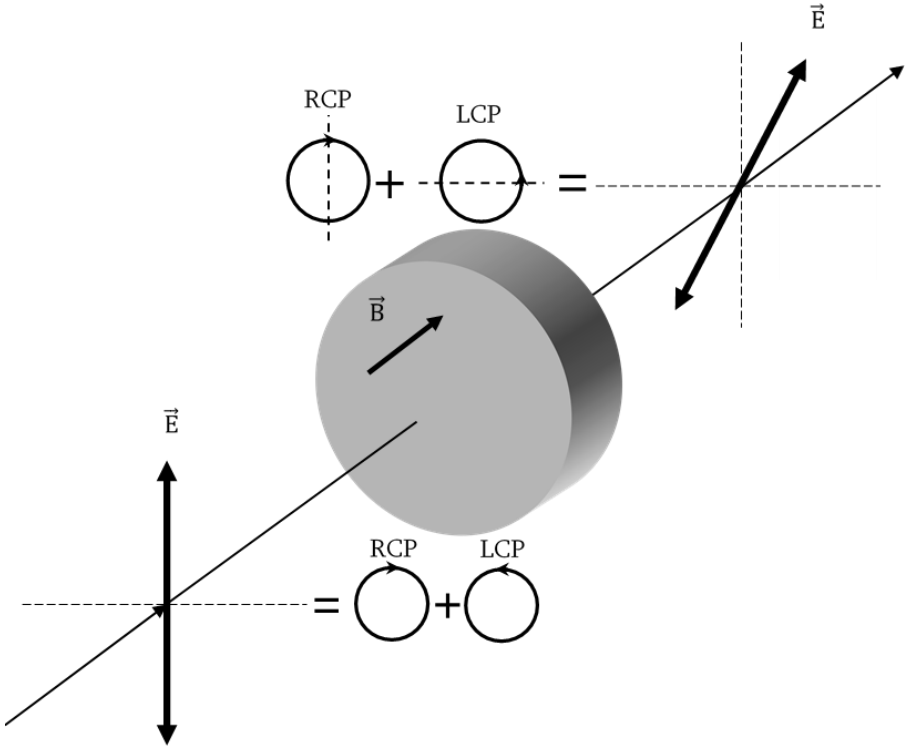

Figure 1.2.1. *Schematic diagram of Faraday rotation in case of transparent approximation as a phase difference between Left circularly -LCP and right circularly polarized RCP lights. LP - Linearly polarized light which can be represented as a sum of RCP and LCP components.*

Formula (1.2.13) is derived for the following configuration: FR took place for the electromagnetic wave propagating along the direction of the magnetization of a medium. If exiting electromagnetic wave somehow will be reflected and again propagated through the material in the opposite direction, the plane of a light will rotate at the same direction, which means resulting FR will be doubled. For example, if magneto-optical medium is capable to rotate the plane of a linearly polarized light by 45°, then one can use them for the development of optical

[1] Along the scope of the thesis talking about FR we will understand specific FR

isolators [18, 25]. The basic operation principle of optical isolators is shown in Fig. 1.2.2. It is typically used to prevent unwanted feedback into a light source.

Non-reciprocal property is also true for microwave frequencies of electromagnetic waves propagating through described magnetized mediums. This allows the creation of radio-frequency devices such as two-port isolators, and three- or four port circulators [25].

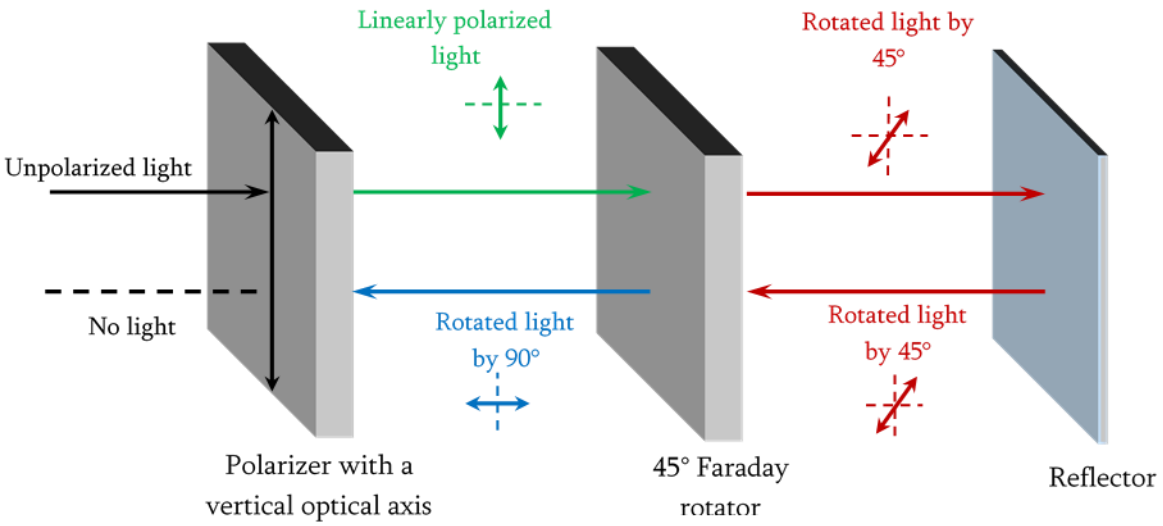

Figure 1.2.2. *The working principle of optical isolators. The plane of linearly polarized light is rotated by 90° after two passes through the magnetized 45° Faraday rotator.*

In general, components of the dielectric tensor are complex because of the absorption of a medium.

$$\varepsilon = \varepsilon' + i\varepsilon'' \tag{1.2.15}$$

$$\varepsilon' = n^2 - k^2 \tag{1.2.16}$$

$$\varepsilon'' = 2nk \tag{1.2.17}$$

k is the extinction coefficient. The $k_{\pm}$ extinction coefficients cause different absorptions of the LCP and RCP components. This gives rise to another phenomenon which is magnetic circular dichroism. In result, while exiting from a medium, a light will be also elliptically polarized, which

is quantitatively described by the Faraday ellipticity. So for non-transparent ferrimagnetic material FR and Faraday ellipticity will be:

$$\theta_F = \frac{\omega(n_+ - n_-)}{c} = Re\left(\frac{\omega\varepsilon_1}{c\sqrt{\varepsilon}}\right) \tag{1.2.18}$$

$$\eta_F = \frac{\omega(k_+ - k_-)}{c} = Im\left(\frac{\omega\varepsilon_1}{c\sqrt{\varepsilon}}\right) \tag{1.2.19}$$

Fig. 1.2.3 shows schematic diagram of a FR and Faraday ellipticity effects. So the non-diagonal component of the dielectric tensor not only describes the FE, which in other words is magnetic circular birefringence, but also Faraday ellipticity or magnetic circular dichroism. Using equations (1.2.15-1.2.17) for non-diagonal components we have:

$$\varepsilon_1' = \frac{c}{\omega}(n\theta_F - k\eta_F) \tag{1.2.20}$$

$$\varepsilon_1'' = \frac{c}{\omega}(k\theta_F + n\eta_F) \tag{1.2.21}$$

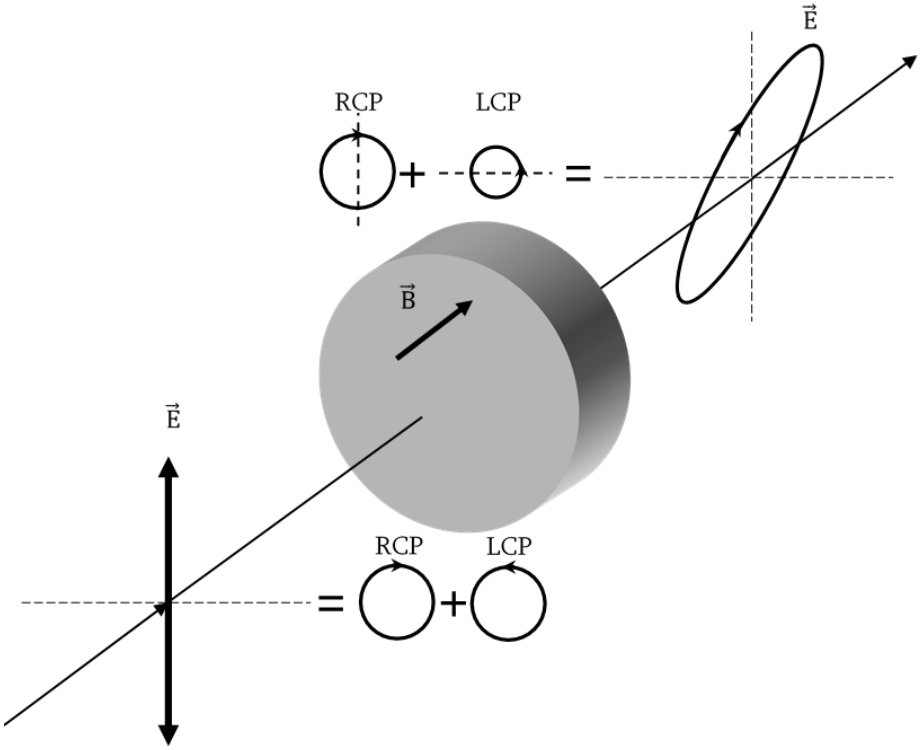

Figure 1.2.3. *Mechanism of FR and Faraday ellipticity in case of non-transparent medium. Left circularly -LCP and right circularly polarized RCP lights. LP - Linearly polarized light.*

Equations (1.2.20) and (1.2.21) show that all the dielectric tensor elements can be calculated if one can experimentally measure θ_F, η_F, n and k. This data of dielectric tensor elements depending on the wavelength can give the possibility to interpret experimental data with microscopic theory of magneto-optical effects. This way magneto-optical avtivity and the influence of Bi substitution was explained for Bi-YIG thin films [19].

Fig. 1.2.4(a) shows the FR (θ_F) spectra of $Bi_xY_{3-x}Fe_5O_{12}$ thin films prepared by LPE method in case of different concentrations of substituted Bi (x=0, x=0.1, x=0.3, x=0.5). Data presented in Fig. 1.2.4(b) was calculated using experimental measurements of θ_F, η_F, n and k and shows the wavelength dependency of non-diagonal elements of dielectric tensor for $Bi_xY_{3-x}Fe_5O_{12}$ (x=0, x=0.1, x=0.3, x=0.5) films [19]. The real parts of ε and ε_1 are assigned as ε' and ε_1' and for the imaginary parts as ε'' and ε_1'' respectively.

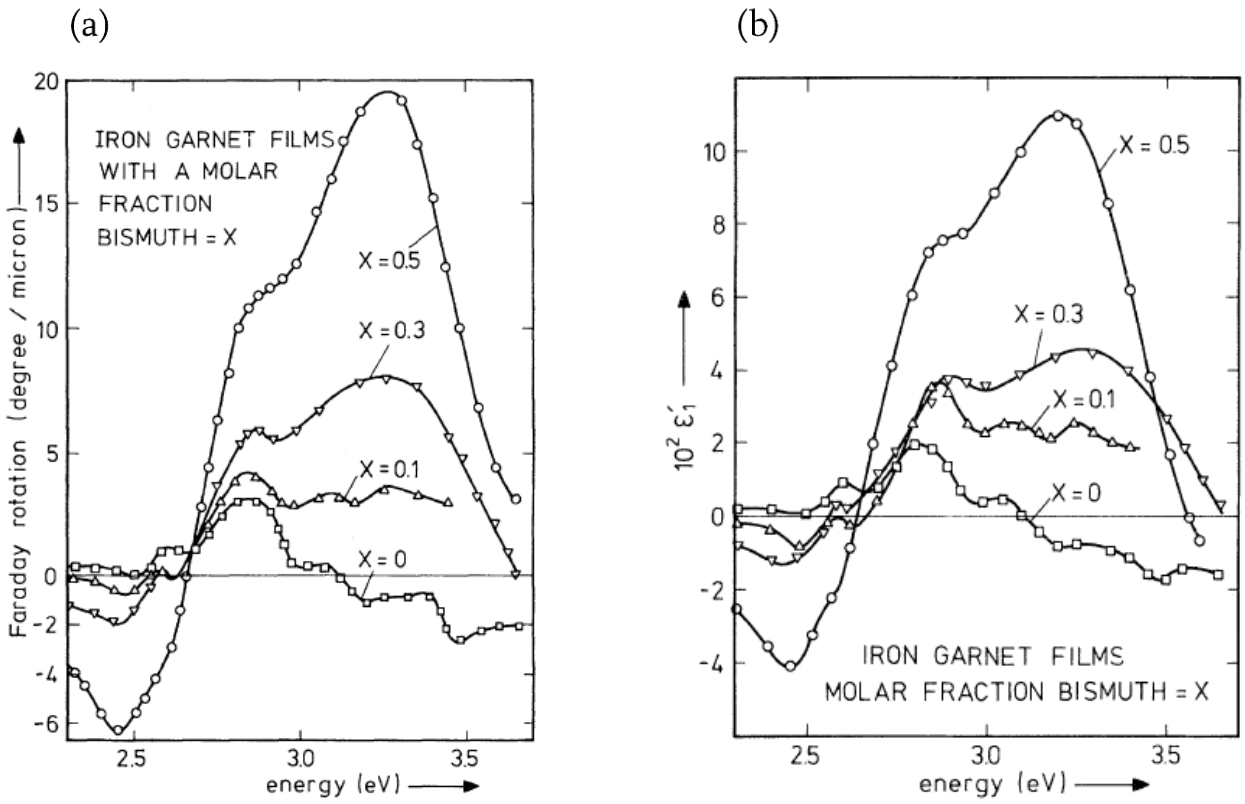

Figure 1.2.4. *(a) FR spectra of Bi-YIG LPE films with different concentrations of doped Bi (b) Non-diagonal tensor elements spectra for the same films calculated from the measurement data of θ_F, η_F, n and k [19].*

To understand the theory of magneto-optical effects for the ferrimagnets such as YIG one also needs to know the microscopic origins of these effects. In the next paragraph we will briefly present microscopic origins of FE for YIG materials.

§1.3. Microscopic origins of the Faraday effect

In the classical electrodynamical approximation the propagation of an electromagnetic wave in a material can be visualized as follows [24]. Material consists of electrons which bound to a nucleus by springs. When electromagnetic wave with ω frequency enters the medium it drives the electrons of a medium. Displaced electron from its equilibrium position will oscillate with ω frequency and reradiate. This way electromagnetic wave will propagate through a medium. In case of anisotropic materials, binding forces on electrons are different in different directions which means spring constants are different depending on the direction. Then the electron displaced from its equilibrium position by electromagnetic wave along one direction will oscillate with a different frequency than another direction.

But the electron's true nature is quantum mechanical. Crystal field is responsible for the electron bound to the nucleus. In this case dominant effect which describes electromagnetic wave interaction with an electron is electric dipole transition. The basic interactions are between rotation electric fields (RCP and LCP) and a collection of electric dipoles of a medium. There are two types of electric dipole transitions which describe magneto-optical interactions: diamagnetic and paramagnetic [26]. The names of these transitions are purely historical and has nothing to do with magnetic properties of materials.

Fig. 1.3.1 shows energy level schemes for diamagnetic and paramagnetic transitions. In case of paramagnetic transitions there is a splitting of a ground state caused by Zeeman effect. Diamagnetic transitions occur between singlet ground state and an excited state which is (2Δ) split by the combined effect of exchange field and spin-orbit coupling. The splitting is proportional to the external magnetic field. As it was said magneto-optical effects are caused by the different polarizabilities of the magnetized material for LCP and RCP. In case of paramagnetic transitions the different occupation of the ground state level is the main cause of the FR. For

diamagnetic transitions the different polarizabilities for LCP and RCP is the result of excited state splitting 2Δ [19].

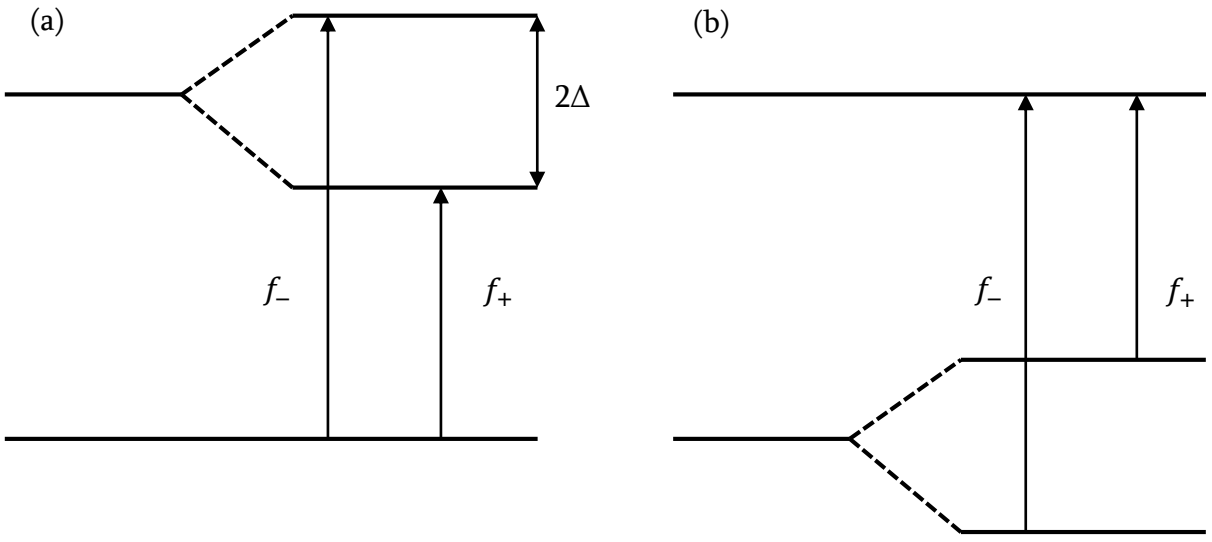

Figure 1.3.1. *Energy level schemes for (a) diamagnetic and (b) paramagnetic transitions. Splitting of states for the diamagnetic and paramagnetic transitions are caused by spin-orbital coupling and Zeeman effect respectively.* f_+ *and* f_- *are oscillator strengths for RCP and LCP lights.*

Fig. 1.3.2 shows calculated spectra of ε_1' and ε_1'' in case of diamagnetic and paramagnetic transitions. It can be shown that for diamagnetic transitions ε_1 expressed as:

$$\varepsilon_1 = \frac{\omega_p^2 f \Delta L}{2\omega_0} \frac{(\omega_0-\omega)^2-\Gamma_0^2+2i\Gamma_0(\omega_0-\omega)}{[(\omega_0-\omega)^2+\Gamma_0^2]^2} \tag{1.3.1}$$

Δ is the excited state splitting, ω_0 is the center frequency, Γ_0 is the halfwidth at half-height of the transition, f is the oscillator strength, L is the Lorentz-Lorenz local field correction [19]. The oscillator strengths for LCP and RCP when there is an excited state splitting can be expressed as [27]:

$$f_\pm \approx (f/2)(1 \pm \Delta/\omega_0)^4 \tag{1.3.2}$$

For the paramagnetic transitions ε_1 will be:

$$\varepsilon_1 = \frac{\omega_p^2 f df L}{2} \frac{\omega(\omega_0{}^2 - \omega^2 - \Gamma_0^2) + i\Gamma_0(\omega_0^2 + \omega^2 + \Gamma_0^2)}{\omega_0[(\omega_0{}^2 + \omega^2 + \Gamma_0^2) + 4\omega^2\Gamma_0^2]^2} \tag{1.3.3}$$

df is the fractional dichroism and defined as:

$$df = \frac{f_- - f_+}{f_- + f_+} = \frac{f_- - f_+}{2f} \tag{1.3.4}$$

Using the difference between the shapes of ε_1' and ε_1'' for diamagnetic and paramagnetic transitions it is possible to interpret experimental spectra of ε_1' and ε_1''.

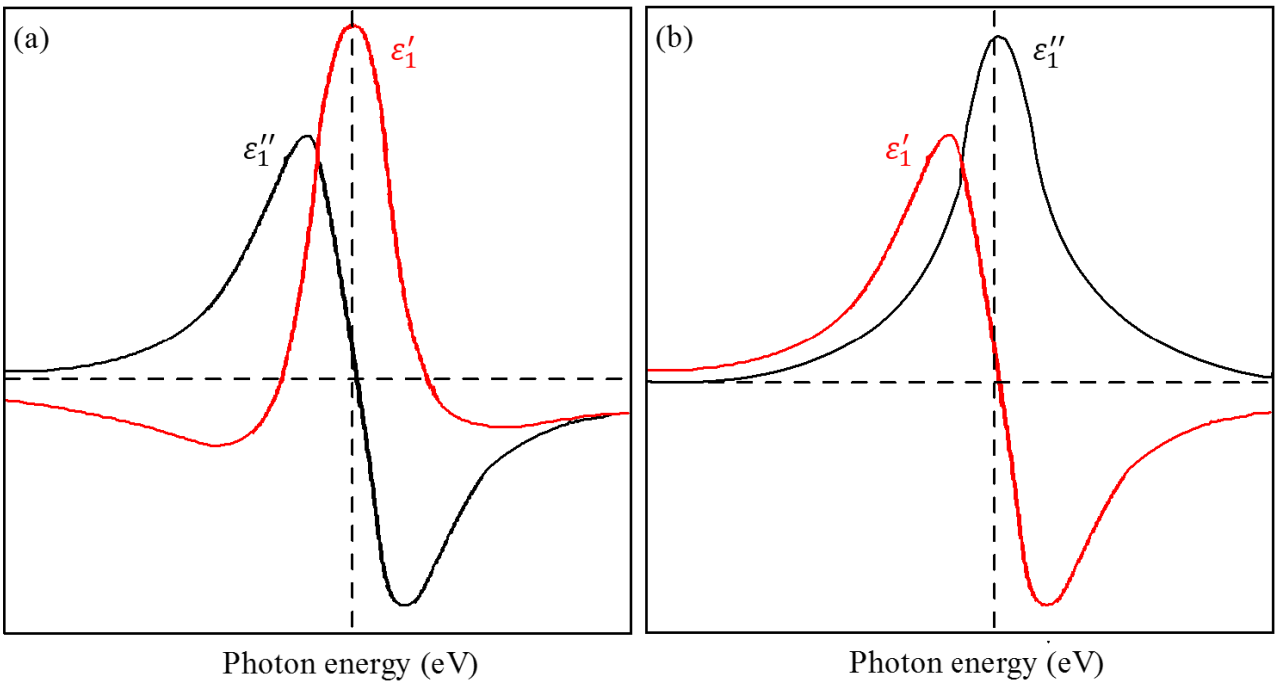

Figure 1.3.2. *Spectral dependencies of real ε_1' (red lines) and imaginary ε_1'' (black line) parts of non-diagonal dielectric tensor component ε_1 of magneto-opticaly active material for (a) diamagnetic and (b) paramagnetic transitions.*

In case of ferrimagnetic materials such as Bi-YIG Zeeman effect is excluded by the superexchange field quenching of the spin degeneracy [27] which means that there is no splitting of ground state in case of paramagnetic transitions. This brings to the logical conclusion that for Bi-YIG materials the main contribution to the magneto-optical properties can come from diamagnetic transitions. In the next chapter Bi substitution effect on the different properties of

YIG will be described but it is worth to mention that Bi-YIG materials have magneto-optical activity which is higher in orders comparing to YIG. This phenomenon somehow questioned the idea that magneto-optical activity of iron garnets can be explained only by optical transitions associated with iron and oxygen ions.

From equations (1.3.1) and (1.3.2) it can be seen that ε_1 depends on Δ and therefore excited state splitting of a diamagnetic transition is the most important parameter which can increase the FR of ferrimagnetic materials. By Wittekoek *et al* the detailed experimental and theoretical studies were published in Ref. [19] where they compared optical and magneto-optical parameters of Bi-YIG and unsubstituted YIG both for polycrystalline and monocrystalline samples. By analyzing the experimental data for non-diagonal components of YIG and Bi-YIG it was concluded that the optical transitions near 2.8 eV and 3.3 eV are the reason for the increase of FR for Bi-YIG. There were no new transitions detected on magneto-optical spectra of Bi-YIG samples comparing to YIG but it was shown that oscillator strengths and spin-orbit coupling were increased (which also increases 2Δ) with bismuth substitution. It is thought that admixture of bismuth 6p orbitals into oxygen 2p and iron 3d orbitals can be the reason for the increase of Δ since the oscillator strength goes up because there are more electrons to make a transition. This theoretical model is one of the most accepted explanations for the Bi effect on FR.

Next chapter is devoted to the characterization and preparation of magneto-optical materials in a form of thin films.

CHAPTER 2. MAGNETO-OPTICAL MATERIALS AND FILM PREPARATION

§2.1. Properties of garnet materials

The general composition of YIG can be written as:

$$\{Y_3^{3+}\}[Fe_2^{3+}](Fe_3^{3+})O_{12}^{2-} \quad (2.1.1)$$

where {} denotes a dodecahedral "c" site, [] denotes an octahedral "a" site, and () denotes a tetrahedral "d" site. YIG has a cubic crystal structure which consists of 3 cations sites with different sizes; this gives a possibility to substitute a large number of ions into the structure of YIG in a controllable way which makes YIG one of the most versatile magnetic systems known. The Curie point for YIG is about 550 K. The lattice constant for YIG is about 12.376 Å [28].

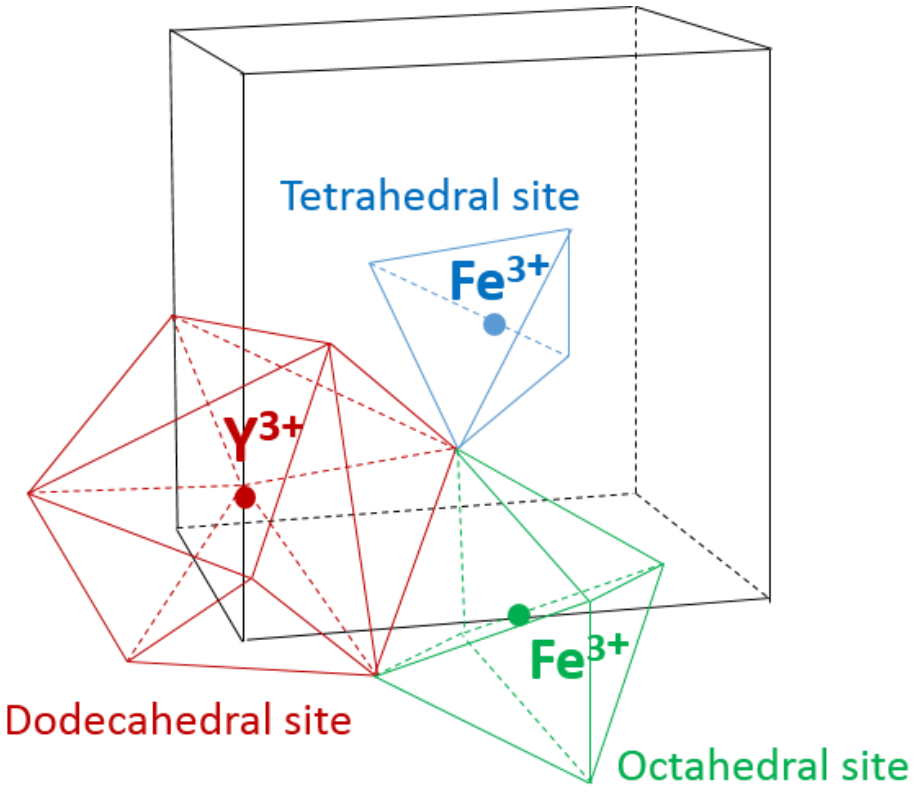

Figure 2.1.1. *Unit Cell of YIG with the different sites for cations. The interaction between Fe^{3+} ions occupying tetrahedral and octahedral sites through oxygen ions surrounding them gives a rise to the ferromagnetic properties of YIG.*

The Y^{3+} ions have zero magnetic moment and ferrimagnetic properties of YIG crystal arises from superexchange interaction between Fe^{3+} ions occupying two inequivalent octahedral and tetrahedral positions. Oxygen ions are responsible for this kind of interaction between Fe^{3+} ions. Equation (2.1.1) shows that within each formula there are two Fe^{3+} ions located on "a" site magnetized in inverse direction to three Fe^{3+} ions located on "d" sites so the resultant difference in magnetizations make these crystals ferrimagnetics. Fig. 2.1.1 shows YIG crystal unit cell [29] and different positions of cations. In general garnet materials for different applications are used as thin films deposited on different kind of substrates.

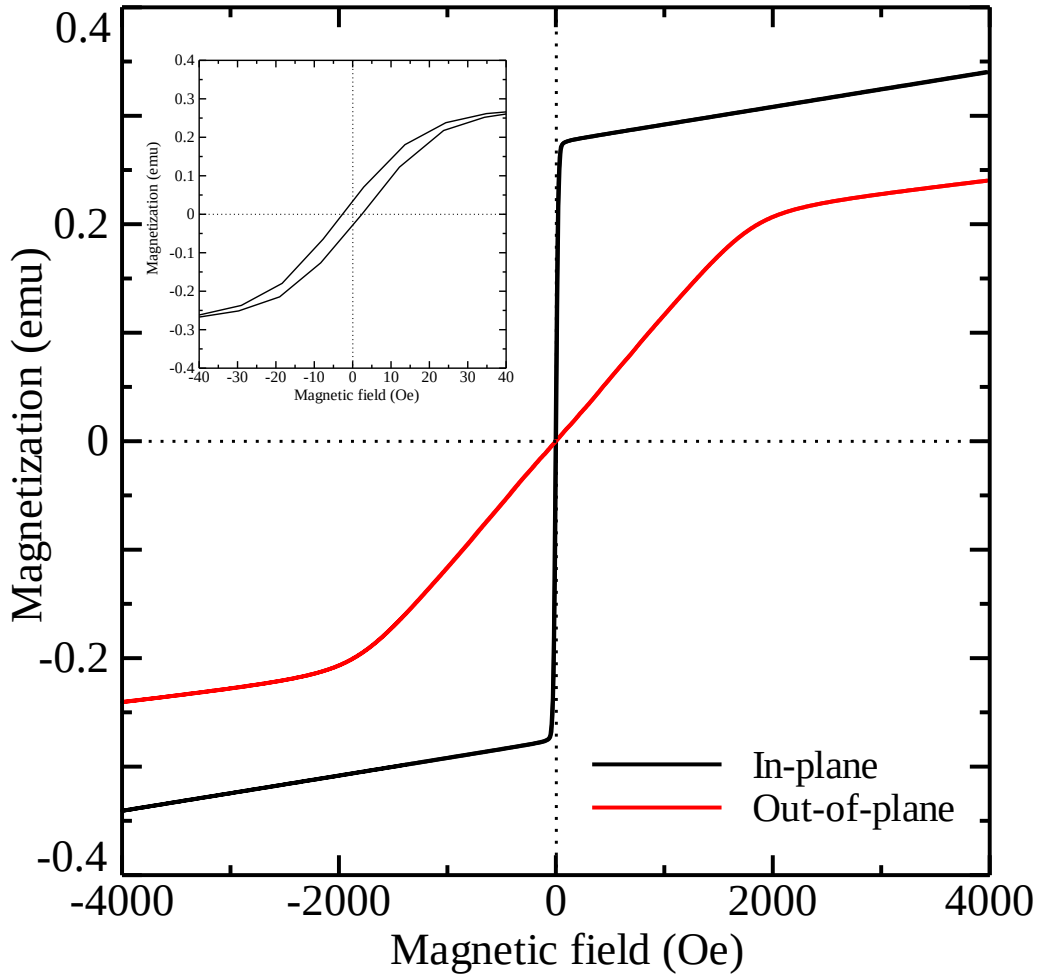

Figure 2.1.2. *Room temperature in-plane (black loop) and out-of plane (red loop) magnetization hysteresis loops of a YIG film. Inset shows in-plane hysteresis loop in smaller range in order to indicate low coercivity of films.*

Fig. 2.1.2 shows M-H hysteresis loop measured by vibrating sample magnetometer (VSM) of the YIG film prepared on a (111) oriented Gadolinium Gallium Garnet (GGG) substrate by LPE method. Under the influence of external magnetic field the magnetic moment of a garnet material has the tendency to align along a preferred direction which is called the easy axis. In Fig. 2.1.2 YIG film shows in-plane easy axis because higher magnetization was obtained at lower external magnetic field values applied along the surface of a YIG film. Non-saturating behavior of hysteresis assigned to paramagnetic nature of GGG substrates. Fig. 2.1.2 inset shows magnetization loop for the in-plane configuration of VSM for magnetic fields in the range of -40 Oe to 40 Oe. From inset one can see that coercivity of YIG films is fairly low and measured to be about ~10 Oe. Worth to mention that for the YIG films which will be used in integrated waveguide applications or MOI in-plane easy axis is very important parameter [20, 29]. Further reading on the topic of the various MO applications of YIG films can be found in Ref. [31-33].

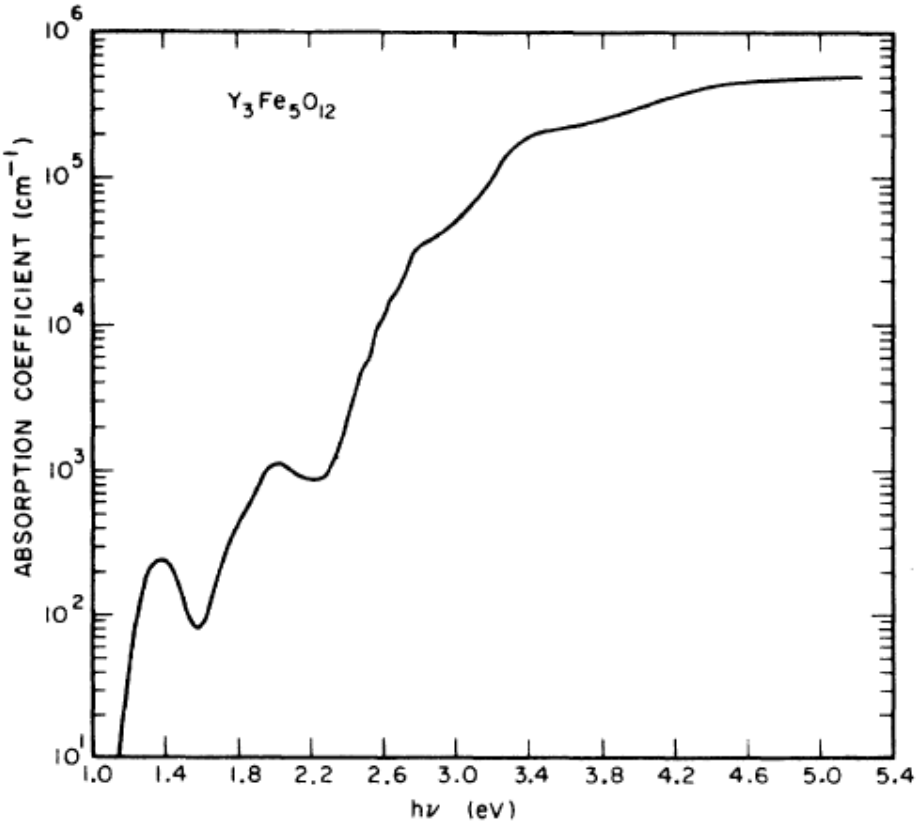

Figure 2.1.2. *Absorption spectrum of YIG obtained from experimental and Kramers-Kronig analysis [34].*

Not only high FR of YIG makes the latter a great material for magneto-optical applications but also its low optical absorption does. For the higher values of wavelength (1200 nm to 5000nm) the absorption is nearly zero. At the shorter wavelengths the absorption grows rapidly because there are no electronic transitions of the Fe^{3+} cations. Fig. 2.1.3 shows the absorption spectrum of YIG [34].

§2.2. Bi substitution effect on the properties of YIG materials

It is possible to obtain a variety of interesting physical (magnetic, magneto-optical, optical) properties of YIG by substitution of yttrium ions with other rare-earth elements or iron ions with other cations.

It is proved that non-magnetic ions can cause the change of magnetic behavior when they doped into the structure of YIG. It was shown by Geller in Ref. [35] that when the d sites are filled with Silicon (Si^{4+}) or Zirconium (Zr^{4+}) ions short-range antiferromagnetic order occurs between a-site Fe^{3+} ions. In Ref. [36] it was shown that in cobalt-substituted yttrium iron garnet $Y_3Fe_{5-x-y}Co_xGe_yO_{12}$ structures magnetic properties vary linearly depending on the level of Co^{2+} substitution. Not only magnetic properties are possible to control by the doping of different ions but also optical and magneto-optical properties. For example, in case of gallium substituted yttrium iron garnet $Y_3Fe_{2-x}Ga_xFe_{3-y}Ga_yO_{12}$ with $0 \le x+y \le 2.95$ epitaxial films and flux grown crystals it was found that wavelength independent reduction is observed in the range of 500 to 1100 nm by increasing gallium content for the optical absorption and FR [37]. For the complex structures such as Iridium substituted yttrium iron garnets $Y_{3-x}A_xFe_{5-y-z}Ir_yB_zO_{12-\delta}F_\delta$ (A=Ca^{2+}, Pb^{2+} and B=Fe^{2+}, Si^{4+}, Zn^{2+}) was found that by doping of Ir^{4+} magnetostriction could be increased [38].

In 1969 Buhrer discovered that FE in magnetic garnets with $Bi_{3-2x}Ca_{2x}Fe_2Fe_{3-x}V_xO_{12}$ structure can be dramatically increased by the doping of Bi^{3+} ions [39]. Hansen *et al.* show in Ref. [40] that FR angle of YIG materials increases by orders with further substitution of Y^{3+} ions with Bi^{3+} and the maximum value of FR can be reached for fully substituted bismuth iron garnet (BIG). Fig. 2.2.1 shows the dependence of the FR on the bismuth content at 633 nm wavelength. As it was presented in paragraph 1.3 the most accepted explanation for this effect was stated in Ref. [19].

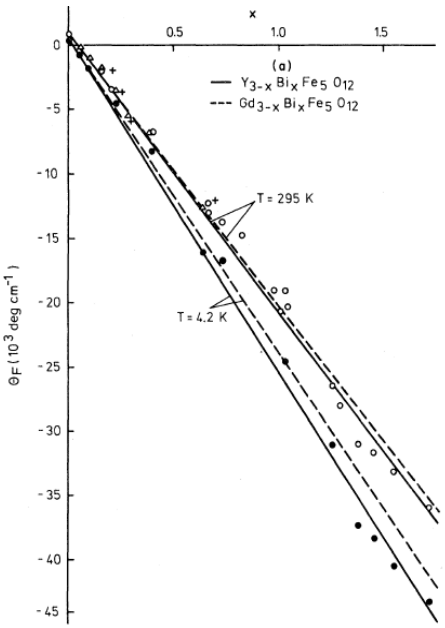

Figure 2.2.1. *Dependence of the FR on the bismuth content for Bi-YIG (solid lines) and Bi-GdIG (dashed lines) films measured at 633 nm. Circles represents data for films grown from different melts from Ref. [40].*

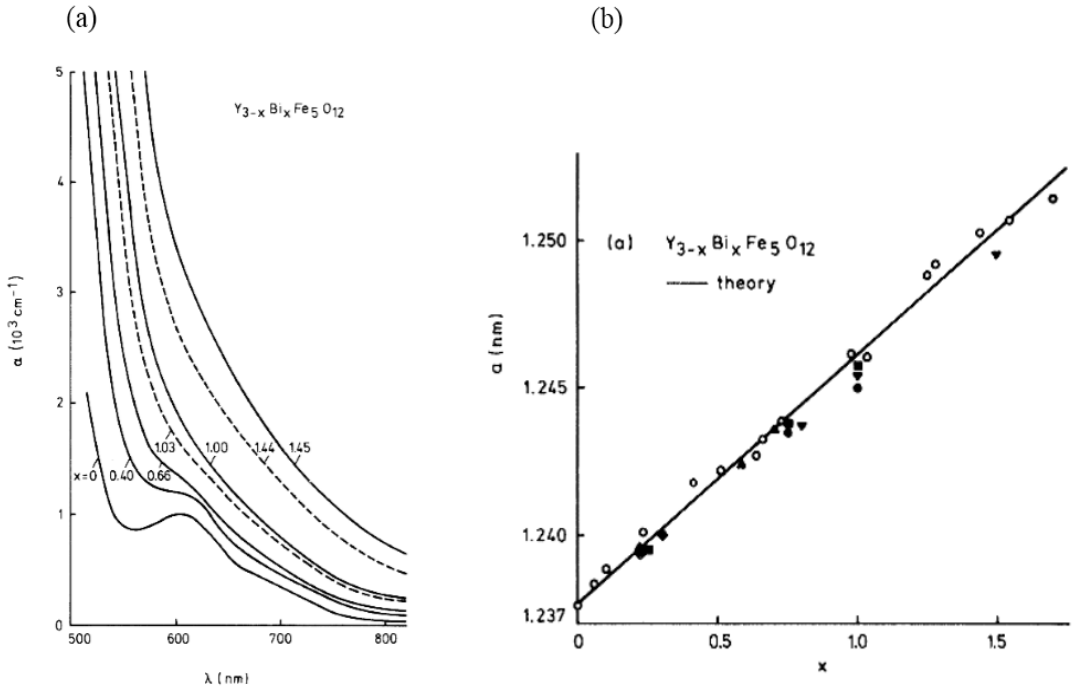

Figure 2.2.2 *(a) Optical absorption vs wavelength for different level of bismuth substitution of Bi-YIG at 295 K temperature and (b) lattice constant of Bi-YIG vs level of bismuth substitution, solid line represents calculated data, symbols are published data from Ref. [40].*

Bi substitution also has its effect on structural, magnetic and optical properties of YIG. Several publications have shown that by the increase of bismuth substitution level the lattice constant also increases [40]. This can be attributed to the larger ion radius of Bi^{3+} comparing to Y^{3+} which are about 1.123 Å and 1.017 Å respectively. For the fully substituted BIG lattice constant was measured to be about 12.62 Å. It was observed that by replacing Bi both the saturation magnetization and the optical absorptions increased. Fig. 2.2.2 shows the dependence of lattice constant and optical absorption on the substitution level of Bi published in Ref. [40].

Fig. 2.2.3(a) shows the wavelength dependencies of absorption, FR and figure of merit (FOM), which is defined as the ratio of the doubled FR to the absorption coefficient of Bi-YIG thin films prepared by PLD method. Fig. 2.2.3(b) shows FR spectra of Bi-YIG thin films with different concentrations of doped Bi and different thicknesses prepared by the MOD method. From both figures it becomes obvious that FR and FOM increased around 530 nm wavelength. This wavelength is considered to be the optimal wavelength for magneto-optical applications where Bi-YIG is used. Fig. 2.2.3(b) shows that Bi-YIG film with x=2.5 concentration of doped Bi and with a thickness of about 200 nm is much larger than thicker films with x=1-2 concentrations of Bi.

YIG materials also possess the lowest microwave losses of all known magnetic materials expressed by the smallest ferromagnetic resonance (FMR) linewidth. Mainly because of this property YIG also found its applications in newly developing field of communications: spintronics [42,43]. There are several microwave applications of YIG films. By using magnetostatic wave (MSW) propagation in YIG films it becomes possible to build microwave devices such as: delay lines, filters, resonators, convolers and correlators [44-47].

In summary the review on previous publications for garnet thin films shows that for MO applications YIG is a great material because of its high magneto-optical activity. By doping of Bi ions into the structure of YIG it is possible to obtain thin films with greater values of FR comparing to YIG films. This is the reason why a great deal of research was implemented to find easy and affordable ways to prepare Bi-YIG films which can be used as indicators for MOI. FOM, which is one of the most important parameters of garnet materials for magneto-optical applications, (further discussed in paragraph 2.5) find its highest value for highly Bi substituted

YIG around 530 nm wavelengths (green light region), so 530 nm is chosen as a wavelength for MOI in our experimental setup. It is also possible to enhance FR of Bi-YIG films by increasing thickness of films (See equation 1.1.1). All the discussed approaches for the increasing of FR of Bi-YIG films were implemented and will be demonstrated in next paragraphs. MOD preparation method of Bi-YIG films will be presented in the next paragraph.

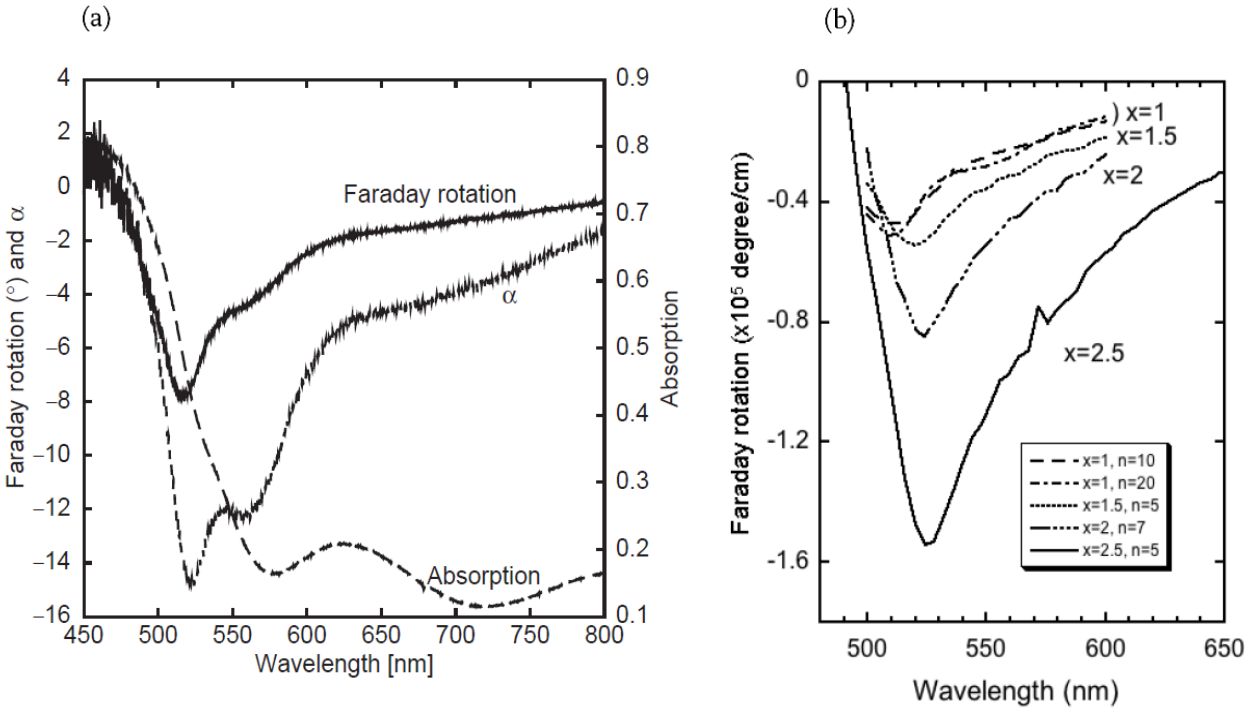

Figure 2.2.3. *(a) The wavelength dependencies of absorption coefficient, FR and FOM for Bi-YIG films prepared by PLD method [41]. The maximum value of FOM and FR is near 530 nm wavelength, (b) FR spectra of* $Bi_xY_{3-x}Fe_5O_{12}$ *(x=1, 1.5, 2, 2.5) thin films with different concentrations of substituted bismuth prepared by MOD method. n is the number of deposited layers on GGG substrate from Ref. [12]. In this case again FR is the highest near 530 nm.*

§2.3. Films preparation methods. Metal-organic decomposition method

A short review on the methods for the preparation of garnet thin films will be presented. There are several methods to prepare garnet thin films and the LPE is the most widely used method to prepare epitaxial garnet films. This method was applied in late 1960's for the first time [48]. However, one of the main disadvantages of LPE is that Bi-YIG films with high concentration

of Bi cannot be obtained using this method [12,49]. Another drawback of the LPE-YIG films is the high optical absorption due to the incorporation of lead and platinum during the synthesis of films into the garnet layer [50].

PLD is one of the most versatile methods for preparation of variety of thin films. The first experiments of PLD were conducted in 1965 by Smith *et al.* [51] and became well known in 1987 when superconducting films where successfully synthesized by Dijkkamp *et al.* [52]. The main drawback of PLD method is the complicated mechanism of the laser ablation [22]. The biggest advantage of PLD is the possibility to prepare films with complex stoichiometries. With a sufficient laser energy and appropriate wavelengths thin films of various composition can be prepared.

Among mentioned methods the chemical solution deposition (CSD) methods such as sol-gel technique [15] and MOD [17] are promising methods for the preparation of oxide thin films [41]. For the synthesis of garnet thin films we chose MOD method for several reasons:

The CSD methods have a unique advantage of homogeneity and controllability of composition.

a) The capability of thin film growth in combination with easy and simple processing.
b) MOD method uses chemically stable solvents such as carboxylic acid. This could be a promising technique keeping the above advantages along with chemical stability.
c) Film growth is based on solution coating and annealing and it does not require any specially designed instruments. This is a great advantage compared to the other methods such as LPE, sputtering method and PLD.
d) Spin coating method can be easily applied in large area deposition with uniform thickness, and can modulate the thickness of the thin film just by choosing the appropriate spin speed and acceleration time.
e) MOD method needs a relatively low temperature compared to the melting point of Bi-YIG for crystallization, so it can be used to fabricate multilayer structures and can prepare thin films on cheap substrates like glass.
f) MOD method utilizes metal carboxylates which have preferable stability and wettability with glass.

Despite these advantages, the MOD method has been less studied than other methods. In the MOD method, crystallization kinetics and physical properties are strongly dependent on the types of ligand, kinds of solution, and heating schedule [17]. To prepare high quality materials, it is necessary to understand the synthesis process in crystallization. Usually garnet films are easier to deposit on garnet substrates because morphological instabilities due to misfit stress are avoided by the use of lattice matched substrates. However, considering large size fabrication and availability, use of non-garnet substrates such as glass is necessary. For example, there is a great need for nonreciprocal devices in integrated photonic devices which makes it important to find a technique for the preparation of garnet materials on non-garnet substrates such as semiconductors or amorphous substrates [30, 53-55].

Fig. 2.3.1 shows schematic diagram of MOD process. MOD method starts either with the preparation of MOD solution or by using commercially available one. Solutions were purchased from Kojundu Chemical Laboratory. We prepared garnet thin films by spin coating of a metal-organic solution on a substrate at 3000 rpm for 30 seconds. The substrates were cleaned using standard cleaning procedures: ultra-sonication in acetone, detergent, distilled water and isopropanol for 15 min. Afterwards films were dried at 70 °C for 30 min in order to evaporate solvent. The films then need to be brought to the amorphous condition which is possible for garnet films with a pre-annealing process at 450 °C for 30 min. One can skip this step but pre-annealing has a big impact on the quality of films [56]. Before the final step of the heat-treatment schedule of the MOD process we need to repeat the previous steps to get appropriate thickness for the films. We used this cycle of steps for all the prepared samples. Then films were post-annealed in a furnace at different temperatures depending on the MOD solution composition and the substrate to achieve crystallization of the samples. All thermal treatments were done in air.

Fig. 2.3.2 shows the photographs of the MOD process step by step.

A detailed study has been conducted by Hanju *et al.* in Ref. [56,57] to understand the crystallization process of Bi-YIG powders and thin films prepared by the MOD method on amorphous glass substrates. It was found that the crystallization temperature for Bi-YIG was 700-750 °C. At lower temperature, secondary phases were crystallized. It was also observed that pre-

annealing temperature, higher than 450 °C, promoted the crystallization of secondary phases due to the formation of nuclei of secondary phases.

In the next paragraphs preparation and characterization of Bi-YIG films with different thicknesses and with different doping concentrations of Bismuth will be demonstrated. Films were prepared on glass and garnet substrates. Preparation of orthoferrite thin films using MOD method also will be presented.

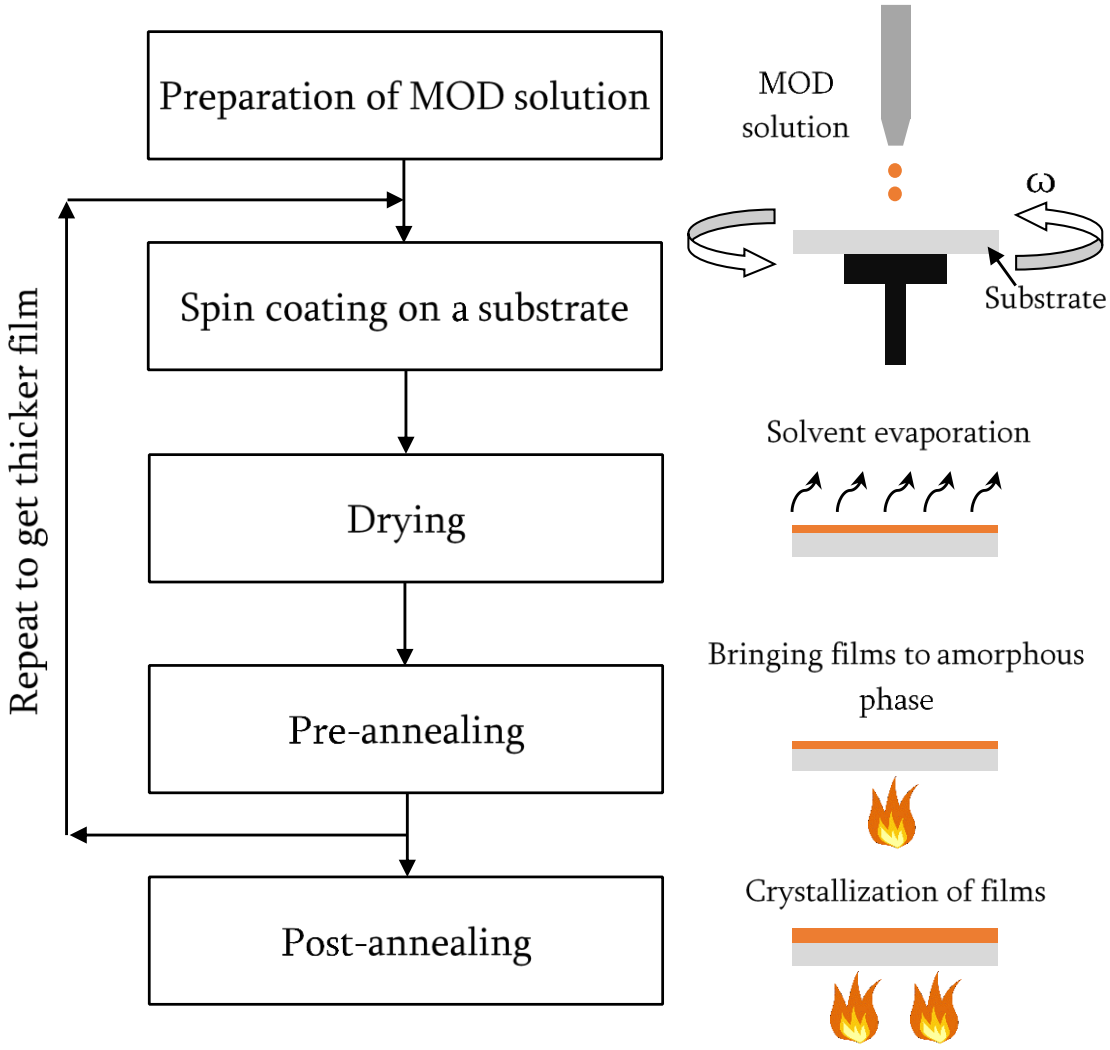

Figure 2.3.1 *Schematic diagram of MOD process. The bars describe the heat-treatment process which takes place during the preparation of films. On the right side the structural status of the film is depicted. By adjusting temperature and time of heat treatment steps depending on the MOD solution and substrate it is possible to obtain crystallized film with different crystal structure.*

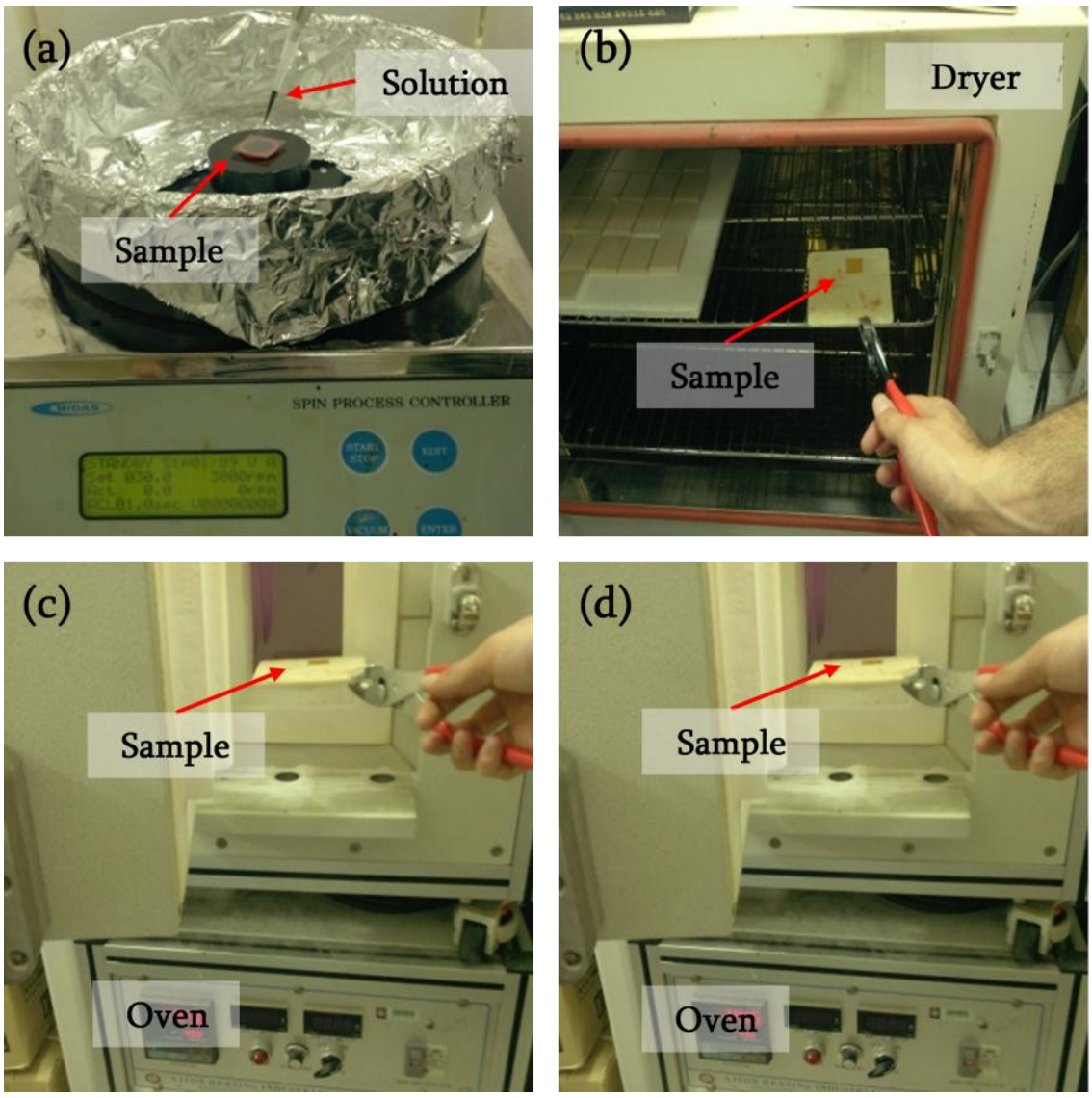

Figure 2.3.2 *Photographs of MOD process. (a) MOD solution deposition process where the samplke placed on spin coater, (b) Drying process, (c) pre-annealing process and after repeating procedures of (a), (b), (c) the final step of MOD process, (d) post-annealing process for the crystallization is applied.*

§2.4. Preparation of Bi-YIG films with different thicknesses

There have been several reports on the preparation of Bi-YIG thin films by MOD method with different concentration of Bi [20, 49, 56]. Most of the publications deal with the preparation of Bi-YIG thin films. This paragraph of the thesis will present detailed study of the preparation conditions for thick Bi-YIG films [58]. High quality Bi-YIG thick films with enhanced magneto-

optical properties can be achieved by using a short time high temperature sintering step during the sample preparation, which we call a pre-crystallization process.

The details of the preparation of thick Bi-YIG films by the MOD method and discussion of the characterization of crystalline structure, magnetic and magneto-optical properties of the samples will be presented.

The chemical composition of the MOD solution was selected to have a ratio of Bi:Y:Fe of 1:2:5 respectively in order to synthesize $Bi_1Y_2Fe_5O_{12}$ films. Each element was synthesized to organo-metallic complexes from carboxylic acids with carbon numbers from 3 to 20 by a reaction with rosin, in organic solvents such as esters.

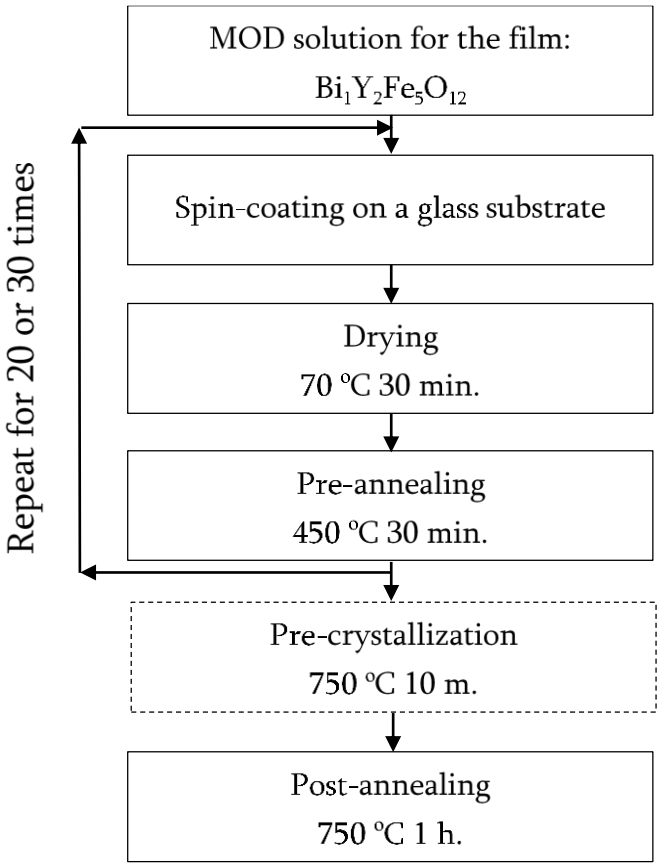

Figure 2.4.1. *The schematic of the MOD process for the preparation of thick Bi-YIG films. We did additional pre-crystallization step after every 10 repetitions of spin-coating, drying and pre-annealing. Only samples B1 and B2 were pre-crystallized.*

The cycle of deposition, drying and pre-annealing processes have been repeated 20 and 30 times to achieve the thicker films with thicknesses of 0.8 μm and 1.2 μm, respectively. After pre-annealing, the samples were pre-crystallized for 1-2 times at 750 °C for 10 minutes. Finally, samples were pots-annealed in a furnace 1 hour for the final crystallization process. Figure 2.4.1 shows the schematic diagram of the MOD process which differs from a MOD process steps showed in Fig. 2.4.1 with additional pre-crystallization process.

Samples A1 (20 times deposited Bi-YIG film) and A2 (30 times deposited Bi-YIG film) were prepared without the pre-crystallization process, while for samples B1 (20 times deposited Bi-YIG film) and B2 (30 times deposited Bi-YIG film) the pre-crystallization process was performed 1 and 2 times, respectively. As substrates we used Corning's Eagle XG borosilicate glass (shortly: XG glass). Table 1 shows FR, structural and magnetic properties of the fabricated Bi-YIG films.

***Table 1**. Magneto-optical, structural and magnetic properties of the fabricated Bi-YIG films.*

Sample	Faraday rotation (°/μm)	Grain size (nm)	Saturation magnetization ($\times 10^{-3}$ emu)	
			In plane	Out of plane
A1	-2.92	43.1	6.4	2.98
B1	-2.65	41.6	5.6	2.76
A2	-2.8	32.9	11.6	4.79
B2	-3.75	43.8	14.5	4.96

To investigate magneto-optical properties of the films FR angles have been measured. The experimental setup for FR measurements is schematically shown in Fig. 2.4.2. A semiconductor laser with 530 nm wavelength is used as a light source (L). The light, after passing the polarizer (P) traverses through the sample (S) under influence of the DC magnetic field which rotates the

plane of polarization of light. The light exiting the sample passes through the rotatable analyzer (A) and finally is detected by a photodiode (D).

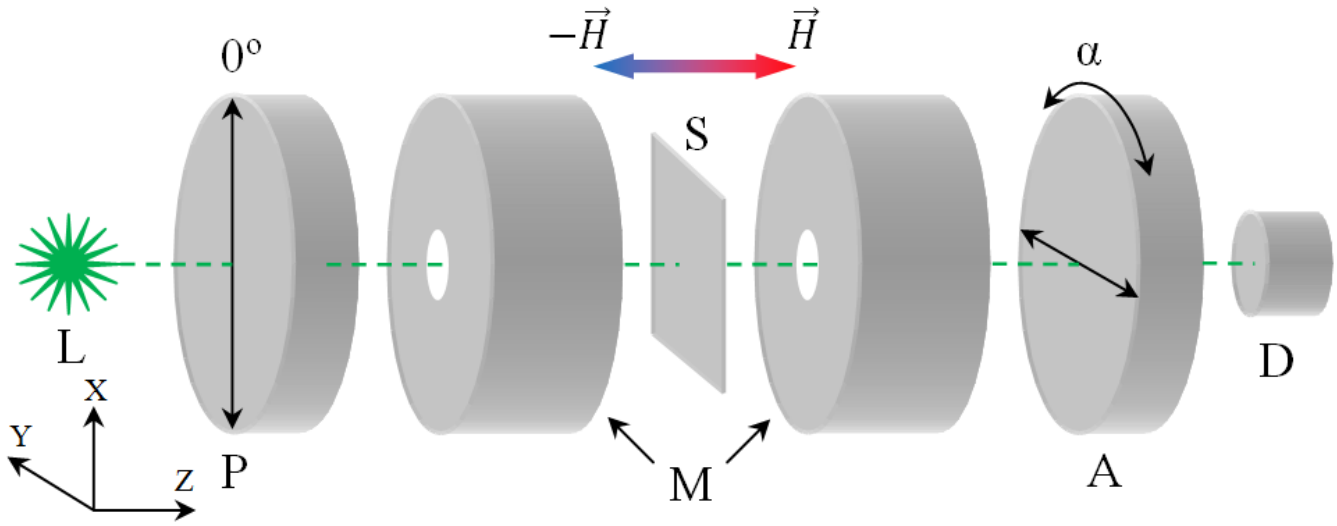

Figure 2.4.2. *The Experimental setup for the FR measurements. L- 530 nm wavelength light source, P-polarizer, M-magnets controlled by power supply, H-Saturating external magnetic field, A-analyzer, D-photodiode.*

By using Jones calculus one can derive the light intensity equation measured by the photodiode

$$I = I_{off} + I_0 \sin^2(\theta + \theta_F) \cong I_{off} + I_0(\theta + \theta_F)^2, \quad (2.4.1)$$

where I_{off} is the intensity of offset (stray) light and I_0 is the initial intensity of light. As the rotation angle of the analyzer is correlated to the FR, we measured the intensity changes according to the rotation of the analyzer around the minimum where the principal axis of polarizer and analyzer were perpendicular to each other. Two intensity curves were recorded for each sample when the external magnetic field was applied parallel and when it was antiparallel to the direction of light propagation. Then the FR angle was calculated by fitting the obtained data with a quadratic function [59]. This method of FR measurement was used for all prepared samples in a scope of this thesis.

Magnetic properties were studied by a VSM. Optical properties were examined by ultraviolet-visible (UV-vis) spectrometer. For the structural characterization and phase identification of thin films X-ray diffraction (XRD) method has been used.

Figure 2.4.3 shows the XRD patterns of fabricated Bi-YIG films. For all samples, the garnet phase peak with (420) plane was observed at 32°. Sample A1 shows a stronger garnet phase and weak secondary phase comparing to the Sample B1. The opposite behavior observes for thicker films. Sample B2 which is prepared by pre-crystallization process and shows a strong garnet phase with the secondary phase barely distinguishable compared with the Sample A2 which is fabricated without the pre-crystallization process. These results are consistent with the magneto-optical properties of the films. Bi-YIG films with better crystallization show larger Faraday rotation angle [20]. The grain size of the films calculated by the Scherrer's (2.4.2) equation and the measured Faraday rotation angle values are shown in Table 1.

$$B(2\theta) = \frac{K\lambda}{L\cos\theta} \tag{2.4.2}$$

K is a dimensionless shape factor which is equal to 0.94, λ is the X-ray wavelegth, L is the line broadening at half the maximum intensity (FWHM) and θ is the Bragg angle.

Through the XRD pattern analysis of the films, the lattice constant was measured to be 12.45 Å. Comparing this data with the dependence of lattice constant on the bismuth content in Bi-YIG films in Ref. [40] and also taking into account that the position of the garnet phase peak for all prepared films observed at the same position it can be suggested that concentration of the bismuth in chemical composition of the films is equal to 1.

Amorphous film crystallization occurs by a nucleation and growth process. For sufficiently thin films, it is expected that surface effects become more significant, since for thinner films the volume decreases and therefore the associated bulk nucleation probability also decreases, whereas the surface area and the probability of surface nucleation remains unchanged [60].

Transformation of the films from the amorphous into the crystalline phase is caused by the driving forces. Free energy of the two material states and the crystallization temperature are determined by the crystallization driving force [61]. As it is shown in Ref. [56], for Bi-YIG powder

preparation (bulk process) a higher crystallization temperature is required compared with the preparation conditions of Bi-YIG films (thin film process).

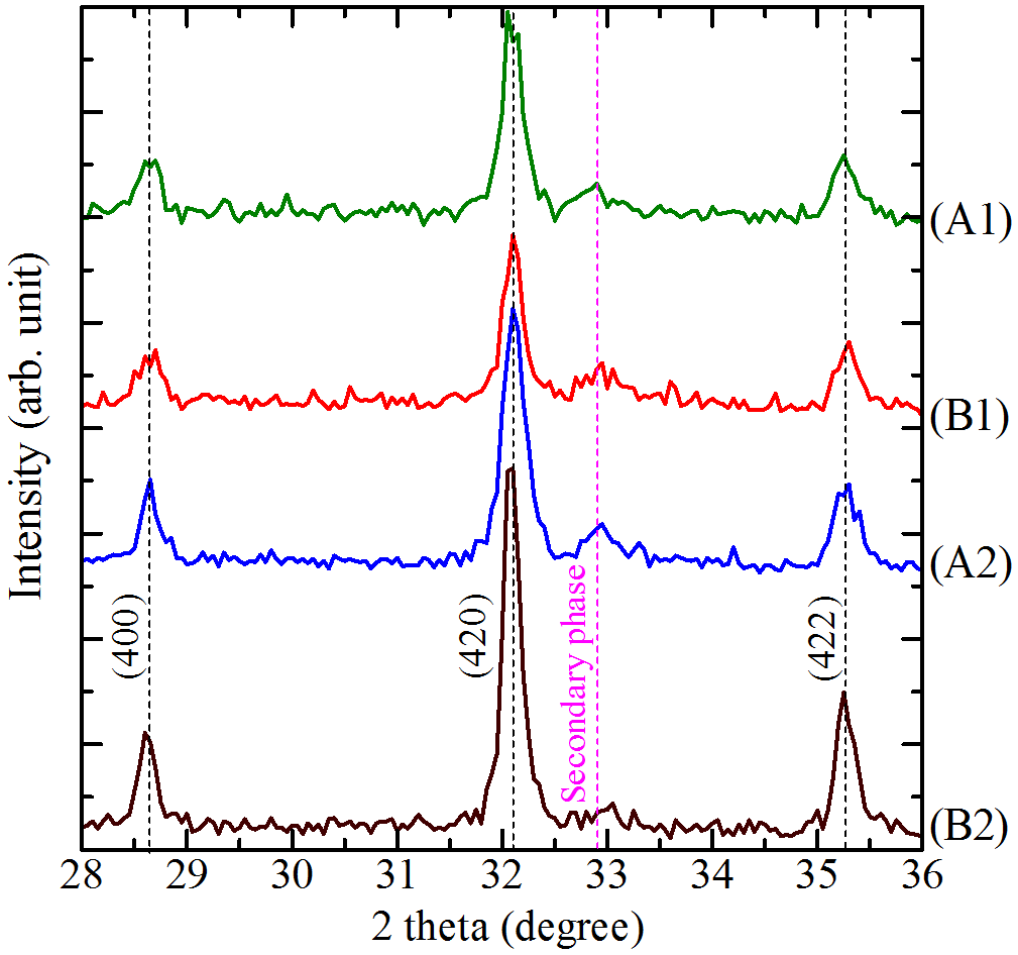

Figure 2.4.3. *X-ray diffraction pattern for the 20 times deposited thick Bi-YIG film prepared without (A1) and with (B1) the pre-crystallization step and for the 30 times deposited thick Bi-YIG film prepared without (A2) and with (B2) the pre-crystallization step. The purple dashed line indicates the position of the secondary phase peak which can be assigned to the weak yttrium orthoferrite phase crystllization. For all samples main diffraction peaks of garnet phase (400), (420) and (422) have been detected.*

We suggest that with increasing thickness of the films the process of the crystallization will be similar to the powder crystallization (bulk process), which means that higher temperature

will be required for the crystallization. But long time or high temperature sintering of the Bi-YIG film will destroy the garnet phase. Using short time pre-crystallization process with the appropriate temperature will promote nucleation from the surfaces of the intermediate layers of the thick Bi-YIG film. After a final crystallization step thick films with the strong garnet phase will be achieved.

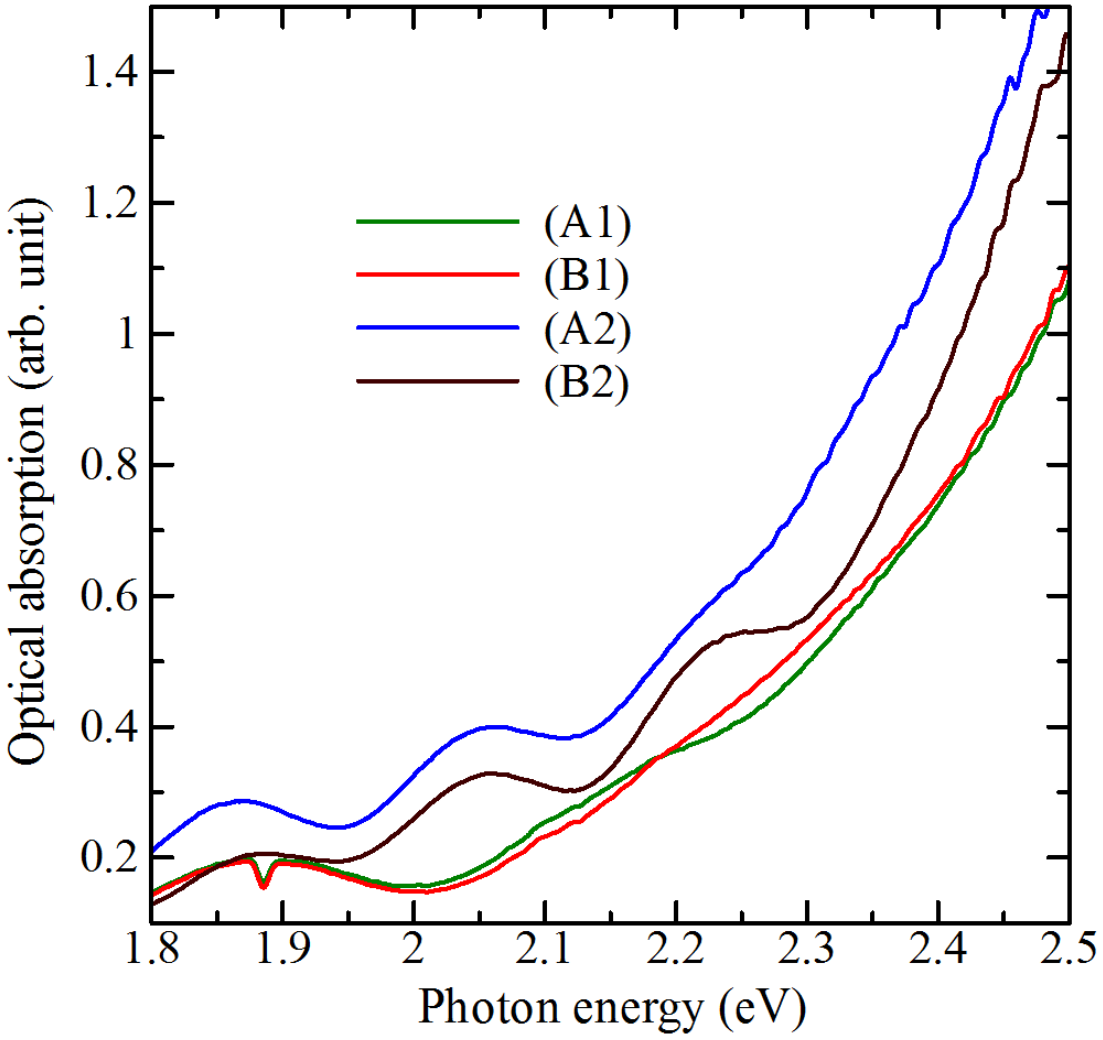

Figure 2.4.4. *Optical absorption spectra for the 20 times deposited Bi-YIG film prepared with (A1) and without (B1) pre-crystallization step and for the 30 times deposited Bi-YIG film prepared with (A2) and without (B2) the pre-crystallization step. Films with 0.8 μm thickness (A1, B1) show almost identical absorption comparing to thick films (A2, B2) where pre-crystallization process decreases absorption.*

Figure 2.4.4 shows the optical absorption spectra of prepared Bi-YIG films. The absorption behavior for 20 time deposited films was almost the same for the preparation without (A1) and

with (B1) the pre-crystallization process. However, the films deposited 30 times with the pre-crystallization step (B2) showed low absorption compared with the films prepared without pre-crystallization (A2). Decrease of the absorption of the thick Bi-YIG film prepared with the pre-crystallization step can be attributed to the lack of secondary phase in the XRD pattern.

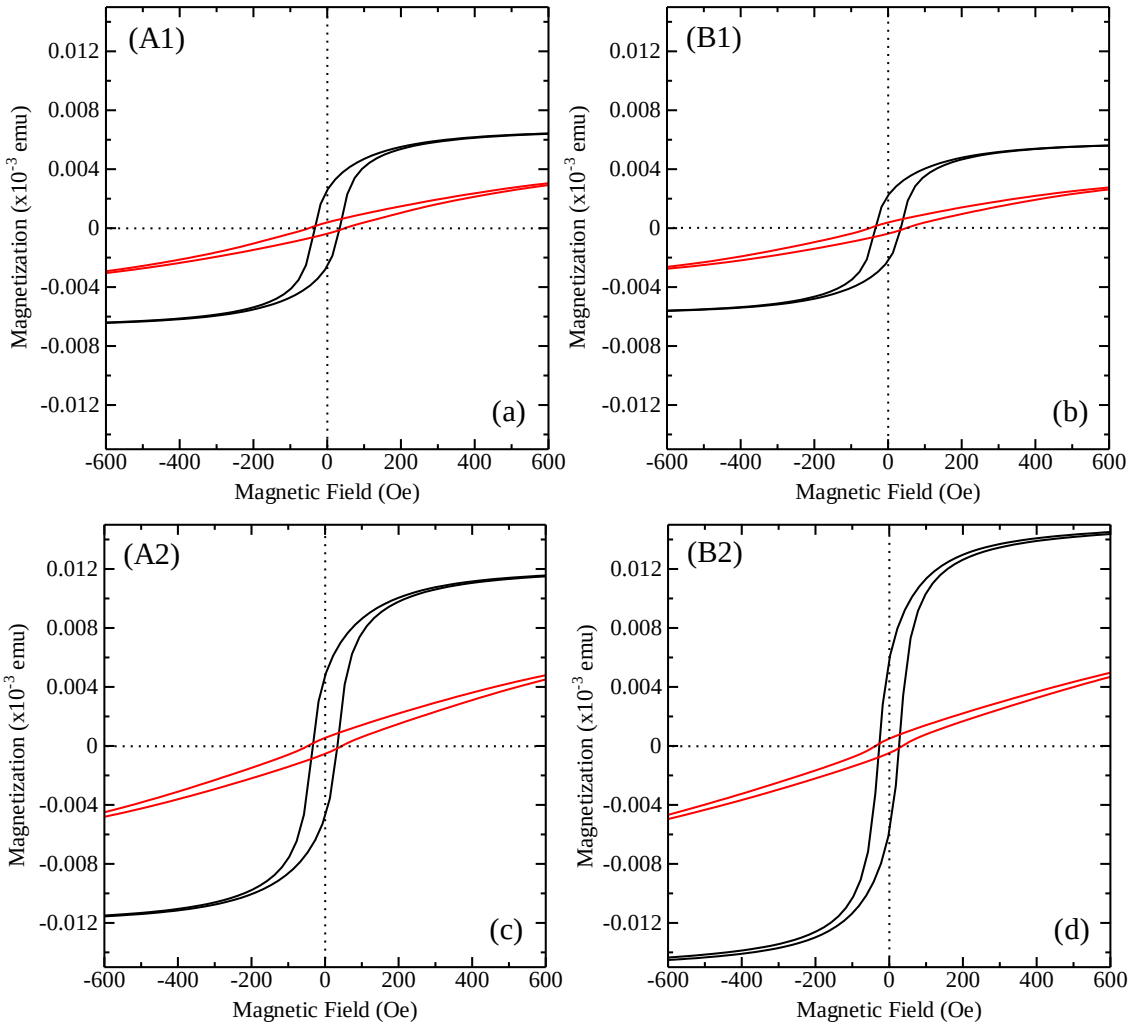

Figure 2.4.5. *Magnetization loops for the 20 times deposited Bi-YIG film prepared without (A1) and with (B1) pre-crystallization process and for the 30 times deposited Bi-YIG film prepared without (A2) and with (B2) pre-crystallization process under in plane (black lines) and out of plane (red lines) magnetic fields. Higher magnetization values were obtained for the longitudinal configuration of VSM measurement which indicates in-plane easy axis of prepared films.*

Figure 2.4.5 shows the magnetization curves for fabricated Bi-YIG films in the plane and the out of plane directions. Sample B2 (Fig. 2.4.5 (d)) shows highest magnetization saturation as shown in Table 1. We attribute these results to the lack of secondary phase in XRD pattern of the sample B2 and the stronger garnet phase comparing to other samples. In comparison to the sample B2, sample A2 shows larger coercivity which means it possesses enhanced hard magnetic properties. Along the in plane magnetic field, films were saturated at weaker magnetic fields comparing to the out of plane magnetic field. These results indicate that the easy axis of Bi-YIG films on glass substrates prepared by the MOD method is parallel to the film plane which gives the opportunity to use them as indicator films in a magneto-optical microscope [20].

Because in the scope of this thesis most of the research on the synthesis of magneto-optical films was implemented using amorphous glass substrates in Fig. 2.4.6 we would like to show the optical and magnetic properties of glass substrates. Fig. 2.4.6 (a) shows UV-vis. absorption spectra of glass substrate. One can clearly see that there is no absorption in the visible light region. Fig. 2.4.6 (b) shows VSM magnetic data of glass substrate in out-of-plane and in-plane configurations. Substrate shows a very weak diamagnetic properties and to indicate the weak magnetic contribution of a substrate and a sample holder of magnetometer we compared hysteresis loop of a Bi-YIG film with a glass substrate (Fig. 2.4.6 (c)).

In summary, polycrystalline Bi-YIG thick film of about 1.2 μm thickness has been successfully synthesized on amorphous glass substrate by the MOD method [58]. We observed that for the preparation of thick films by the MOD method pre-crystallization process is crucial. This process promoted better crystallization, high magneto-optical properties, low optical absorption and high saturation magnetization for the film. All films have magnetic anisotropy parallel to the film plane. It is suggested that the pre-crystallization process enhances surface effects in the crystallization of the thick films which gives the possibility of fabricating thick films at low temperature using thin film preparation conditions.

Because of the huge impact of heat treatment on the characteristics of Bi-YIG films in the next paragraph the study of the influence of post-annealing temperature on the magneto-optical and structural properties of Bi-YIG films will be presented.

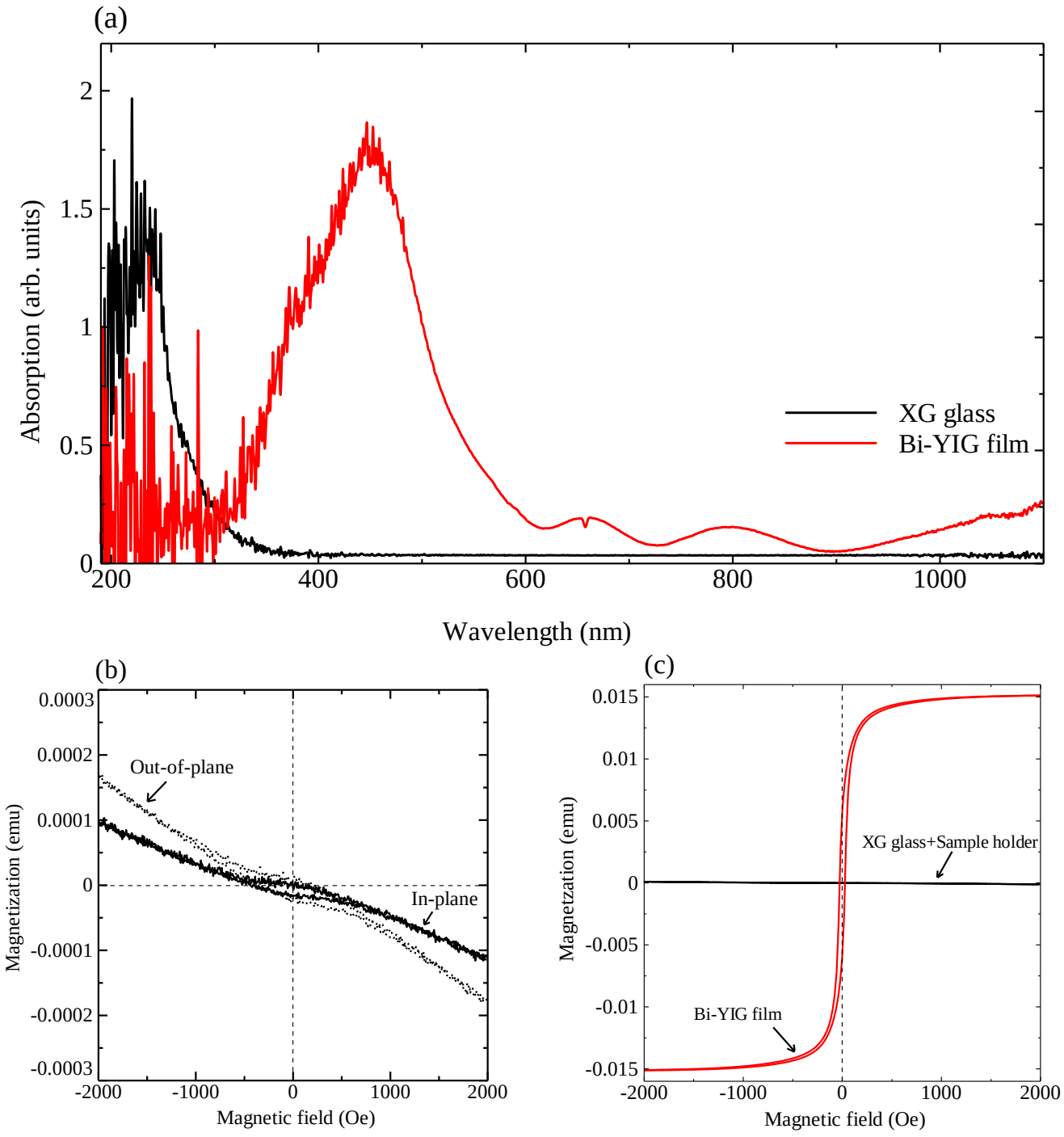

Figure 2.4.5. *Properties of XG glass substrates. (a) Absorption spectra of XG glass substrate (black line) and Bi-YIG film with 0.8 μm thickness (red line), (b) VSM magnetic data for the XG glass substrate and (c) comparison of VSM data for Bi-YIG film and XG glass substrate.*

§2.5. Effect of post-annealing on the properties of Bi-YIG films

In this paragraph the deposition of garnet layers with different levels of concentration of Bi doped into the chemical structure of YIG will be presented. As a substrate for films preparation we used XG glass. The discussion on the influence of post-annealing temperature on magneto-optical and structural properties of films will be given. We found appropriate routines of MOD process to obtain thin films with high FR angles.

We fabricated four sets of Bi-YIG thin films. Each set represents thin films with specific concentration of doped bismuth ($Bi_xY_{3-x}Fe_5O_{12}$, x=1, 2, 2.5, 3) that were prepared by using different post-annealing temperatures. Preparation parameters of samples are shown in Table 2.

The cycle of deposition, drying and pre-annealing is done with the same parameters which has described previously. This cycle of thermal treatments was implemented for 10 times for the Set 1 ($Bi_1Y_2Fe_5O_{12}$) thin films. Afterwards films were post-annealed at 600-750 °C for 1 hour in order to crystallize films.

When concentration of Bi enhances it becomes difficult to obtain films with high quality using glass substrate. One of the techniques that can be applied is the magnetic buffer layer deposition technique [58]. $Bi_1Y_2Fe_5O_{12}$ buffer layers were used for the films with $x \geq 2$ concentration of doped Bi (Set 2 with x=2, Set 3 with x=2.5 and Set 4 with x=3). For the deposition of buffer layer we implemented the cycle of thermal treatments (deposition, drying and pre-annealing) only once. Then buffer layers were post-annealed at 750 °C for 1 hour. We chose exactly this parameters of post-annealing for buffer layers because data for Set 1 samples revealed that at this temperature films with good crystallinity can be obtained. Afterwards process of the deposition of the $Bi_xY_{3-x}Fe_5O_{12}$ (x=2, 2.5, 3) film layer started. Solution was deposited, dried and pre-annealed for 10 times to achieve appropriate thickness of the films. Finally films were post-annealed in a furnace at different temperatures (Table 2). All thermal treatments were done in air. Fig. 2.5.1 shows schematic diagram of MOD process.

Table 2. *Preparation conditions and FR values of films*

Set of samples	Buffer layer $Bi_xY_{3-x}Fe_5O_{12}$	Concentration of Bismuth $Bi_xY_{1-x}Fe_5O_{12}$ (x=)	Sample	Post-annealing temperature (°C) and duration (hours)		Faraday rotation (°/μm)
Set 1	No	1	1	600	1	-0.6
			2	620		-0.8
			3	640		-1
			4	660		-1.2
			5	680		-1.6
			6	700		-2
			7	**750**		**-2.5**
Set 2	Yes	2.0	8	600	3	-4.2
			9	**620**		**-6.6**
			10	640		-5.6
			11	660		-5.6
			12	680		-5.5
			13	700		-4.5
			14	750		-4
Set 3	Yes	2.5	15	600	3	-2.4
			16	**620**		**-3.6**
			17	640		-3.3
			18	660		-2.5
			19	680		-2.6
			20	700		-2.4
			21	750		-2
Set 4	Yes	3.0	22	600	3	-
			23	620		-
			24	640		-
			25	660		-
			26	680		-
			27	700		-
			28	750		-

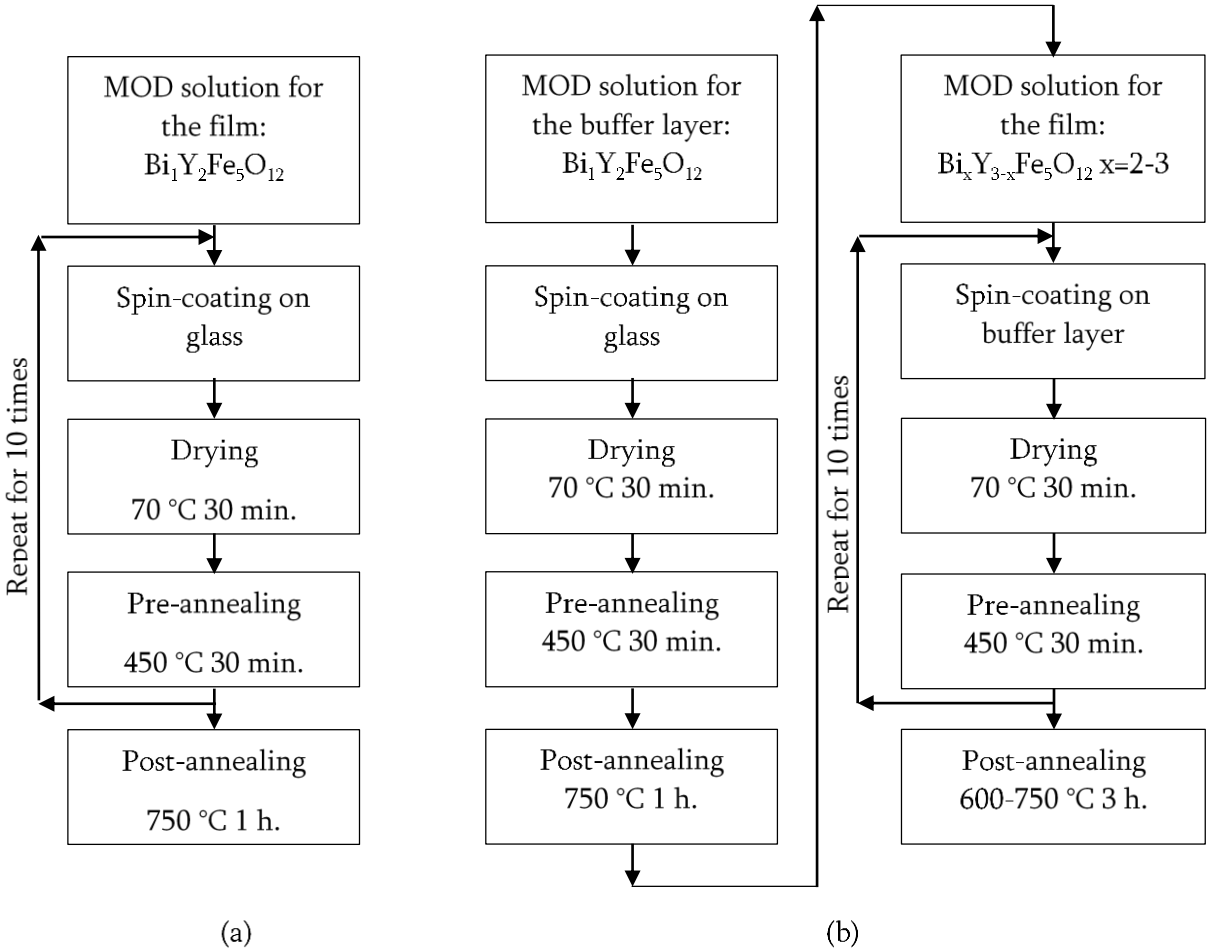

Figure 2.5.1. *Schematic diagram of MOD process (a) without buffer layer deposition and (b) with buffer layer.*

Figure 2.5.2 indicates values of FR for the films with different level of Bi substitution post-annealed at 600-750 °C. For the films with x=1 FR increases when they are post-annealed at higher temperatures. The largest FR was measured to be about -2.5 °/μm. For the higher levels of Bi substitution (x=2, 2.5) the FR curves are different in comparison with x=1. We can notice that for x=2 and x=2.5 FR is increased for the films which were post-annealed at 620 °C. But the decrease of FR for x=2.5 comparing to x=2 is interesting because FR should be increased for higher concentrations of substituted bismuth [40]. We suggest that films with x=2.5 are partially garnet which is confirmed by the XRD results. On the other hand, films with x=3 showed very weak magneto-optical properties and as it was expected XRD patterns showed no diffraction peaks. Thus, we conclude that x=3 films were amorphous.

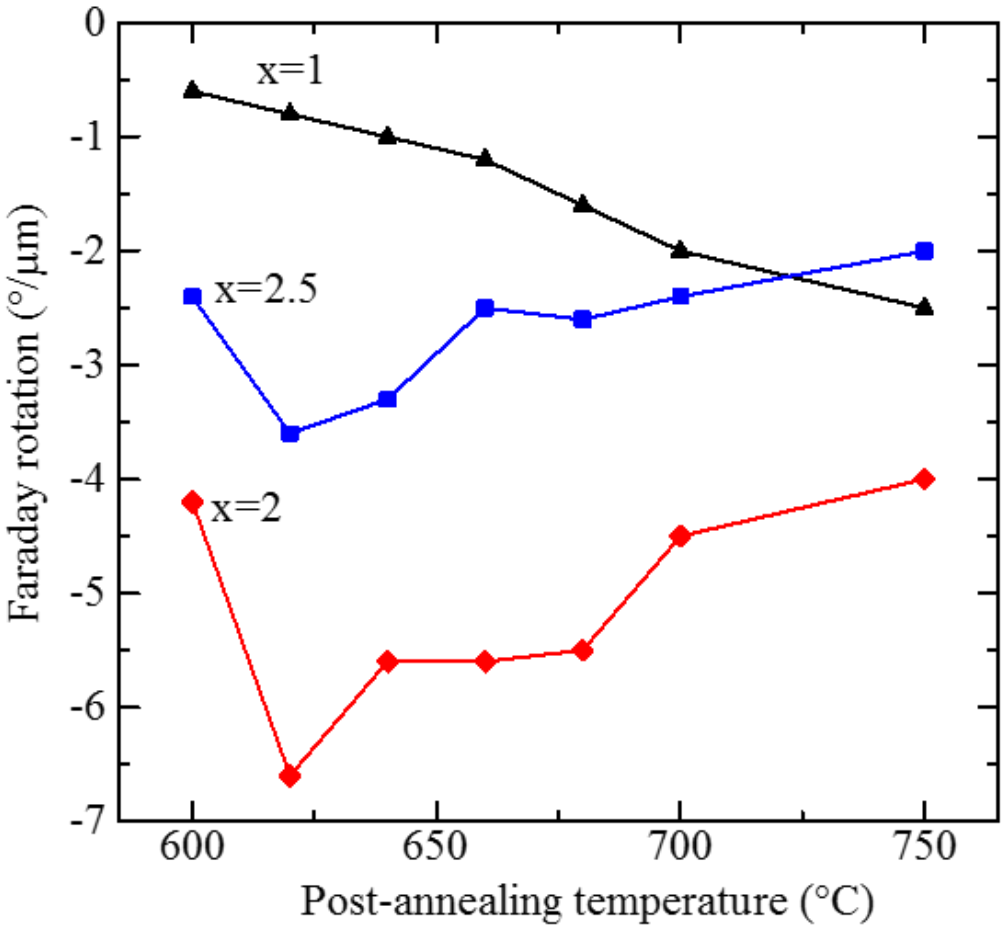

Figure 2.5.2. *Dependence of FR on post-annealing temperature of the films with different concentration of substituted Bi (x=1, x=2, x=2.5).*

Figure 2.5.3 shows XRD patterns of the films that have the highest FR angles in each set. From XRD patterns we measured lattice parameters of samples. It was shown that by the substitution of Bi in YIG thin films lattice parameter increases. By comparing measured data with other publications and theoretical data for lattice constants we can make assumptions about the level of Bi in the crystal structure of films. Samples with x=1 show X-ray diffraction peaks corresponding to the garnet phase. Lattice constant was measured to be about 1.245 nm which is in good agreement with a data published for garnet thin films prepared by LPE method [40]. Very weak secondary phase which we assigned to Yttrium orthoferrite ($YFeO_3$) appeared for the film with x=2 [62].

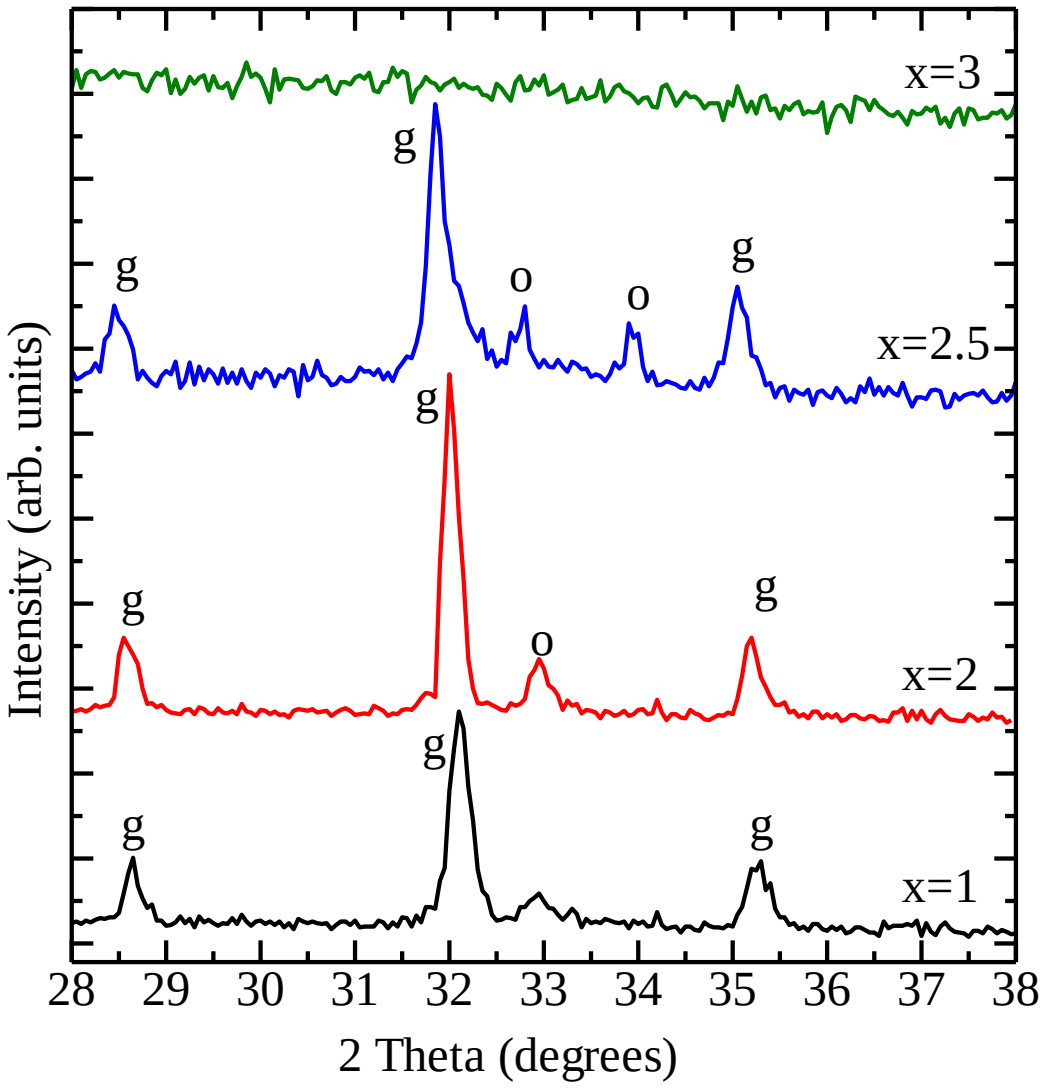

Figure 2.5.3. *XRD patterns of samples with the highest FR from each set. Assignment of diffraction peaks are indicated as following: g: garnet phase, o: YFeO3.*

$YFeO_3$ diffraction peaks became stronger for the film with x=2.5. We suggest that $Bi_{2.5}Y_{0.5}Fe_5O_{12}$ is not fully crystalized and the concentration of Bi in the crystal structure is lower than 2.5. This suggestion can be confirmed by several results: appearance of $YFeO_3$ phases on XRD pattern, low intensity of the main (420) garnet diffraction peak comparing to the x=2, lower value of a lattice parameter comparing to the theoretical and other experimental data and finally low FR comparing to the film with x=2. No diffraction peaks appeared on the XRD spectra of x=3. We compared lattice parameters calculated from the XRD patterns represented in Fig. 2.5.3 with data published in ref [40] which states that the lattice constant of $Bi_xY_{3-x}Fe_5O_{12}$ depends linearly

on the content of bismuth. Our results show little decrease of the lattice constants for $Bi_2Y_1Fe_5O_{12}$ (about 0.05 Å) and $Bi_{2.5}Y_{0.5}Fe_5O_{12}$ (about 0.06 Å).

Figure 2.5.4 indicates the doped Bi level and post-annealing temperatures for which different phases of crystallization of films are detected by XRD spectrometry. Phases of crystallization were assigned as a result of the discussion which consists of the following 3 parts:

1. Faraday rotation angle value measurement
2. Assignment of phases appeared on XRD spectra
3. Calculation and comparison with published data of lattice parameters

Figure 2.5.4 also shows that for the samples with higher level of substituted bismuth the crystallinity can be improved with a lower temperature of post-annealing (620-660 °C). Similar behavior of Bi-YIG thin films crystallization was published for the samples prepared with the sol-gel process [63]. As we note, films with better crystallinity show higher FR values. It was reported in Ref. [20] that garnet films prepared by the MOD method with better crystallinity show higher MO activity. By better crystallization of the films the orbital mixing of Fe^{3+} with Bi^{3+} increased which on the other hand increases the excited state splitting 2Δ of the Fe^{3+} [19,20]. 2Δ is the main cause of FR in Bi-YIG thin films and by increasing 2Δ higher values of FR can be obtained [20]. In our experiments films which possess very low FR angle show very weak or no garnet phase, thus by checking FR of the films it is possible to determine film preparation conditions and make predictions about the crystallinity of a sample before examining other properties.

Buffer layer deposition method was used to prepare polycrystalline Bi-YIG films on glass substrates with high level of bismuth substitution. Magneto-optical measurements showed that FR for films with x=1 can be increased with high post-annealing temperatures (about 750 °C). For films with x=2 and x=2.5 FR increased when films were post-annealed at lower temperatures (about 620 °C) [64]. From XRD measurements we concluded that films with highest FR showed better crystallinity of garnet phase. Lattice parameters of films with x=1, 2 and 2.5 were measured to be 12.45 Å, 12.5 Å and 12.54 Å, respectively. The increase of the lattice parameter with a

substitution level of bismuth is in agreement with previous publications for garnet films prepared with other methods.

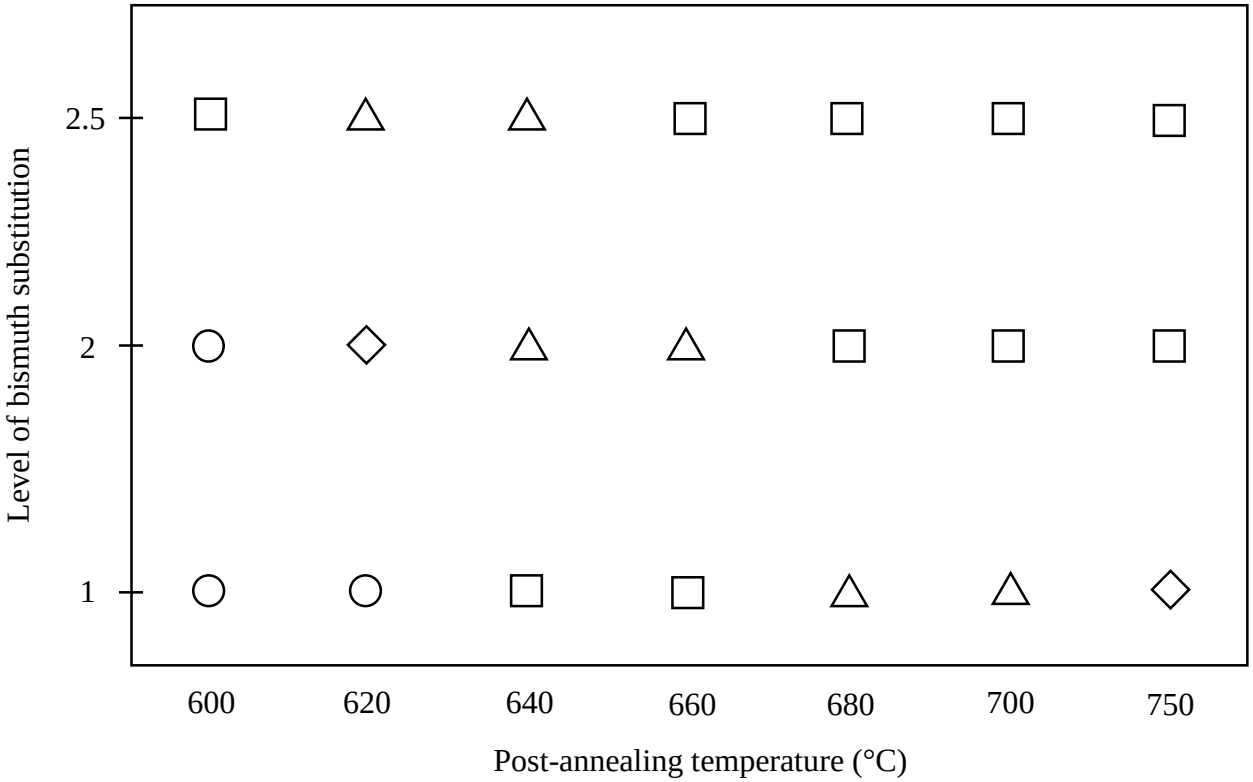

Figure 2.5.4. *Crystallographic phases of Bi-YIG thin films depending on the level of doped Bi and post-annealing temperature. Assignment of phases are indicated as following: ◊: garnet phase, Δ: garnet partially, □: other phase, o: amorphous.*

§2.6. Preparation of highly substituted Bi-YIG indicator thin films directly on glass

Using data obtained from the research presented in previous paragraph especially results which shows that for the films $Bi_xY_{3-x}Fe_5O_{12}$; x=2 higher FR and better crystallinity can be obtained at lower temperatures comparing to the $Bi_xY_{3-x}Fe_5O_{12}$; x=1 films we tried to prepare $Bi_xY_{3-x}Fe_5O_{12}$; x=2 thin films without buffer layers using low post-annealing temperatures. In order to make discussion about the quality of prepared films we also tried to synthesize $Bi_xY_{3-x}Fe_5O_{12}$; x=2 thin films on garnet substrates to compare them.

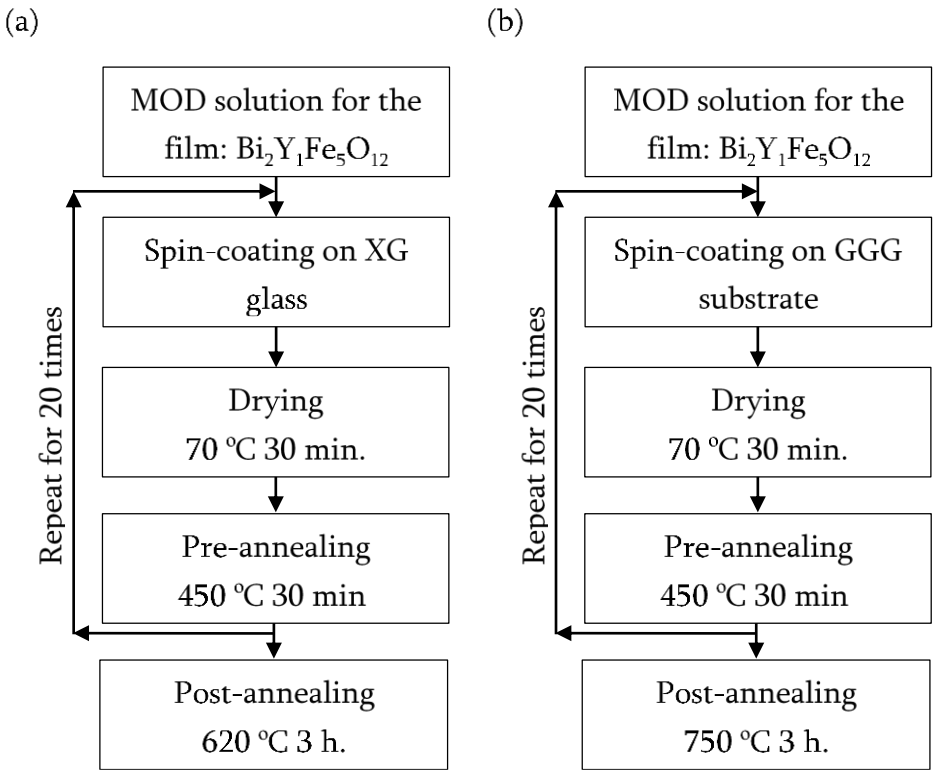

Figure 2.6.1. *Schematic diagram of MOD process (a) for Sample S2 and (b) for Sample S3.*

After intensive experiments on the conditions of synthesis we finally found appropriate MOD routines for the preparation of $Bi_2Y_1Fe_5O_{12}$ directly on glass substrates without any buffer layers using solutions which consist of liquids made from carboxylates with the desired chemical composition. The crystallization of strong garnet phase which was accompanied with a high magneto-optical activity was achieved using lower post-annealing temperature compared to $Bi_1Y_2Fe_5O_{12}$ thin films. We observed the crystallization, FR angle, magnetic and optical properties to describe the effect of synthesis conditions on sensitivity of magneto-optical indicators. Finally, we used the indicator films in a magneto-optical visualization setup.

Newly prepared 2 samples with a same concentration of Bi doping ($Bi_xY_{3-x}Fe_5O_{12}$; x=2) and different substrates will be compared with a Sample S1 which was prepared by a deposition of a $Bi_xY_{3-x}Fe_5O_{12}$; x=1 chemical solution on XG glass substrate. Sample S2 is a $Bi_xY_{3-x}Fe_5O_{12}$; x=2 on a XG glass and Sample S3 is a $Bi_xY_{3-x}Fe_5O_{12}$; x=2 on GGG substrate. Both XG glass and GGG

substrates have the same 0.5 mm thickness and 10×10 mm^2 surface area. Typical thickness of the obtained films is approximately 0.8 μm.

Figure 2.6.1 shows the preparation conditions and the schematic diagram of the MOD process for S2 and S3.

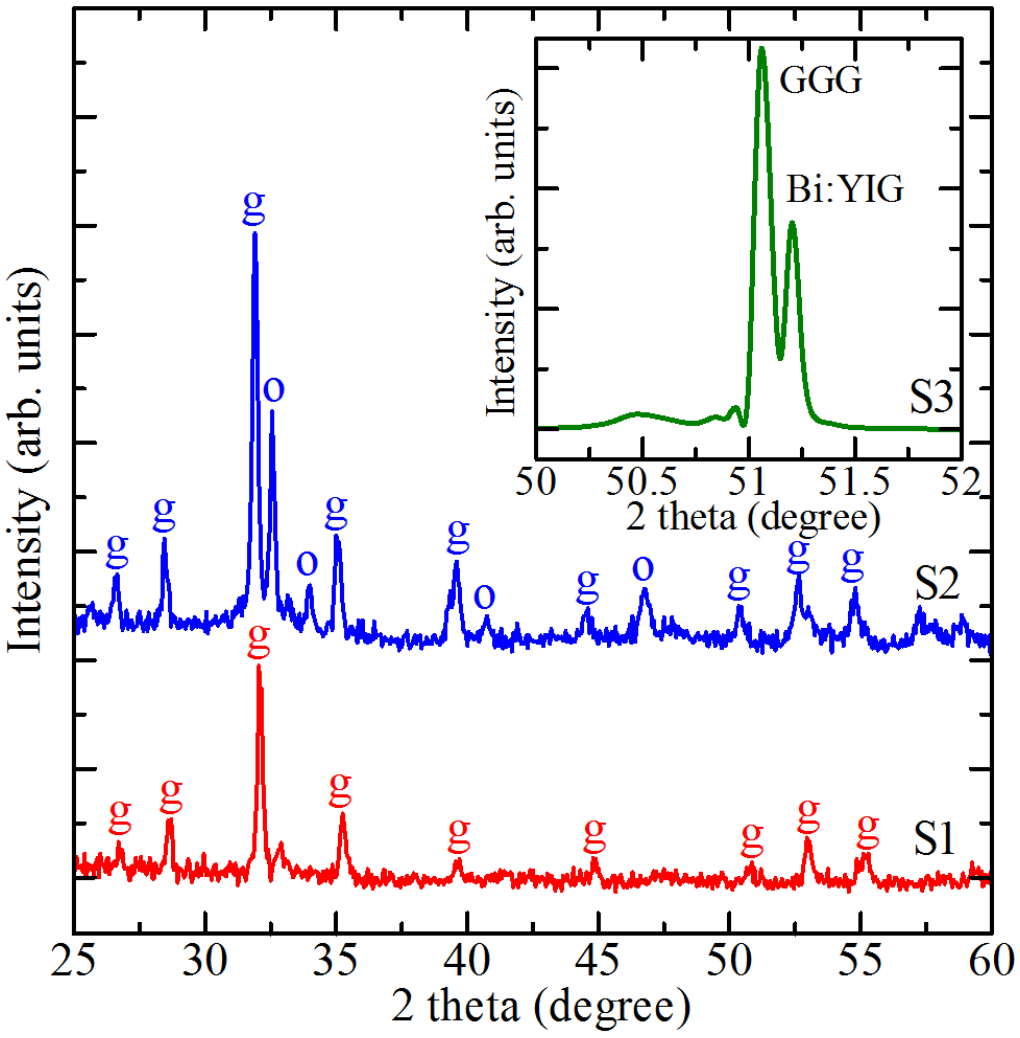

Figure 2.6.2. *XRD patterns for the prepared samples S1, S2, and S3 (inset). Assignment of diffraction peaks are indicated as follows: g: garnet phase, o: o-$YFeO_3$, GGG: Gadolinium Gallium Garnet peak, Bi:YIG: Bismuth substituted yttrium iron garnet peak.*

Films were post-annealed in a furnace at different temperatures depending on the MOD solution composition and the substrate to achieve crystallization of the samples. Sample S1 has been prepared by the MOD process conditions which were previously described for $Bi_1Y_2Fe_5O_{12}$

thin films. Figure 2.6.2 shows the XRD pattern of the prepared films. S1 and S2 were polycrystalline while S3 was single crystalline. All discovered peaks for sample S1 were assigned to the garnet phase.

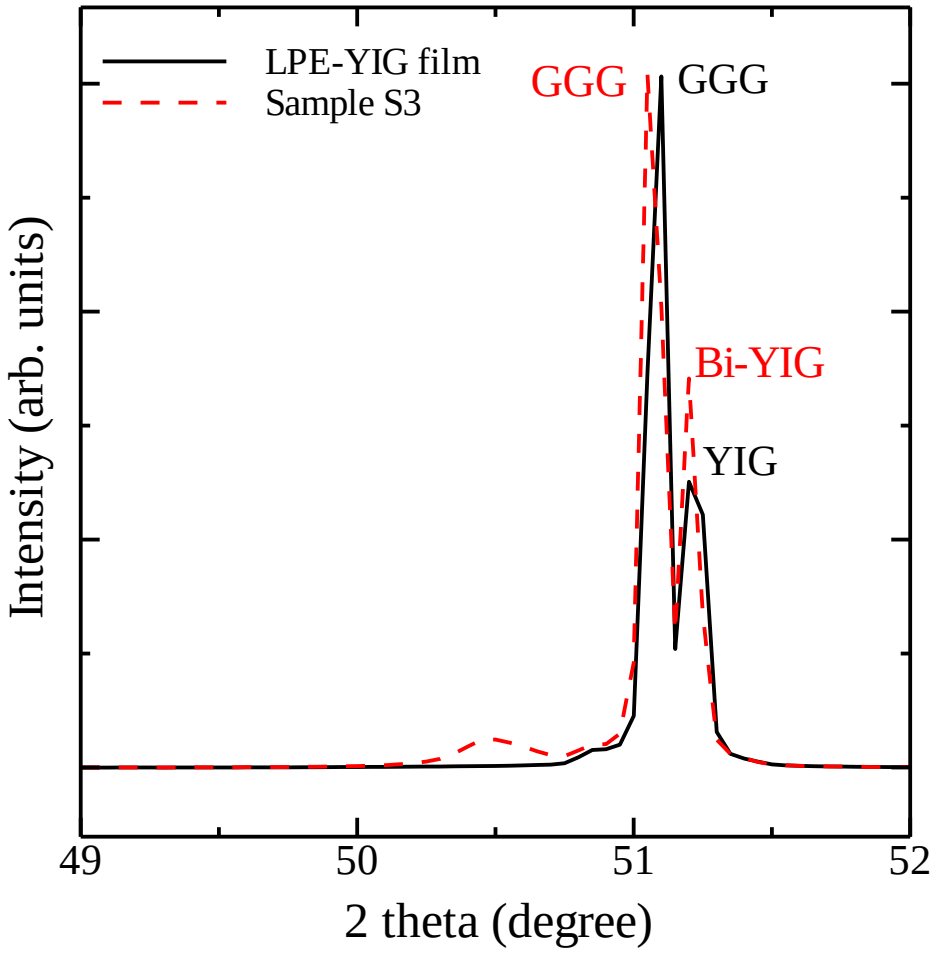

Figure 2.6.3. *Comparison of XRD patterns of sample S3 and LPE-YIG film. GGG Gadolinium Gallium Garnet peak. Bi-YIG: Bismuth substituted yttrium iron garnet peak, YIG: yttrium iron garnet peak for LPE-YIG film*

As it was mentioned in our experiments films which possess very low FR angle show very weak or no garnet phase, thus by checking FR of the films it is possible to determine film preparation conditions and make predictions about the crystallinity of a sample before examining other properties.

High FR angles and better crystallization of a garnet phase was detected for the samples with $Bi_2Y_1Fe_5O_{12}$ composition in the range of 600-640 °C post-annealing temperatures which were carried out for 1h. The temperature of crystallization is lowered by more than 100 °C compared to $Bi_1Y_2Fe_5O_{12}$ thin films. A longer time of post-annealing intensifies the garnet phase of S2 but for the films post-annealed more than 3h bending of the glass substrate starts to be noticed. We found that for the preparation of sample S2 with $Bi_2Y_1Fe_5O_{12}$ composition sintering at 620 °C temperature for 3 h is the best way to make the films with high MO activity and a strong garnet phase. There are another reports showing that additions of Bi largely decreases the crystallization temperature but also the appearance of secondary phases in the crystal structure of films becomes possible [63, 65]. It was reported that $YFeO_3$ is known as an intermediate phase during the process of thermally induced yttrium iron garnet crystallization starting from an amorphous phase [66]. In Fig. 2.6.2 one can see that strong secondary phase accompanying to the garnet phase of the sample. We assigned secondary phase peaks to orthorhombic yttrium orthoferrite o-$YFeO_3$. The inset of Fig. 2.6.2 shows the XRD pattern of single crystalline Sample S3 grown on the GGG (111) substrate. Sample S3 was post-annealed at 750 ºC for 3 h. Diffractions peaks positions are in good agreement with a data for the YIG films prepared by LPE method on GGG substrate. Fig. 2.6.3 shows XRD spectras of LPE-YIG film and Sample S3.

The indicator thin film is the core element of the MOI setup, thus to obtain high quality MO images, the prepared films should have high sensitivity which can be checked by the FOM: f,

$$f = 2\theta_F / \alpha . \tag{2.6.1}$$

Figure 2.6.4 shows optical absorption spectra of the prepared samples. With the substitution of bismuth the absorption of samples for visible wavelengths increased which degrades the sensitivity of the indicator films. On the other hand, doping of bismuth in the YIG structure greatly increases the FR so as a result the FOM of Bi-YIG increased. After measurement of FR angles and absorption spectra we calculated the FOM of samples at 530 nm (inset of Fig. 2.6.4). S3 possessed the highest FR but at the same time the optical transmittance of the sample was very low. As we can see, S2 has the highest FOM. These results are very interesting because sample S2 has a multiphase crystalline structure yet the FR angle was about -11 °/μm which is

comparable with FR values of highly doped Bi-YIG thin films prepared with other methods[94]. To the best of our knowledge, there are no reports on the preparation of $Bi_2Y_1Fe_5O_{12}$ layers directly on glass by the MOD method with such a high FR and a lower post-annealing temperature than 620 °C.

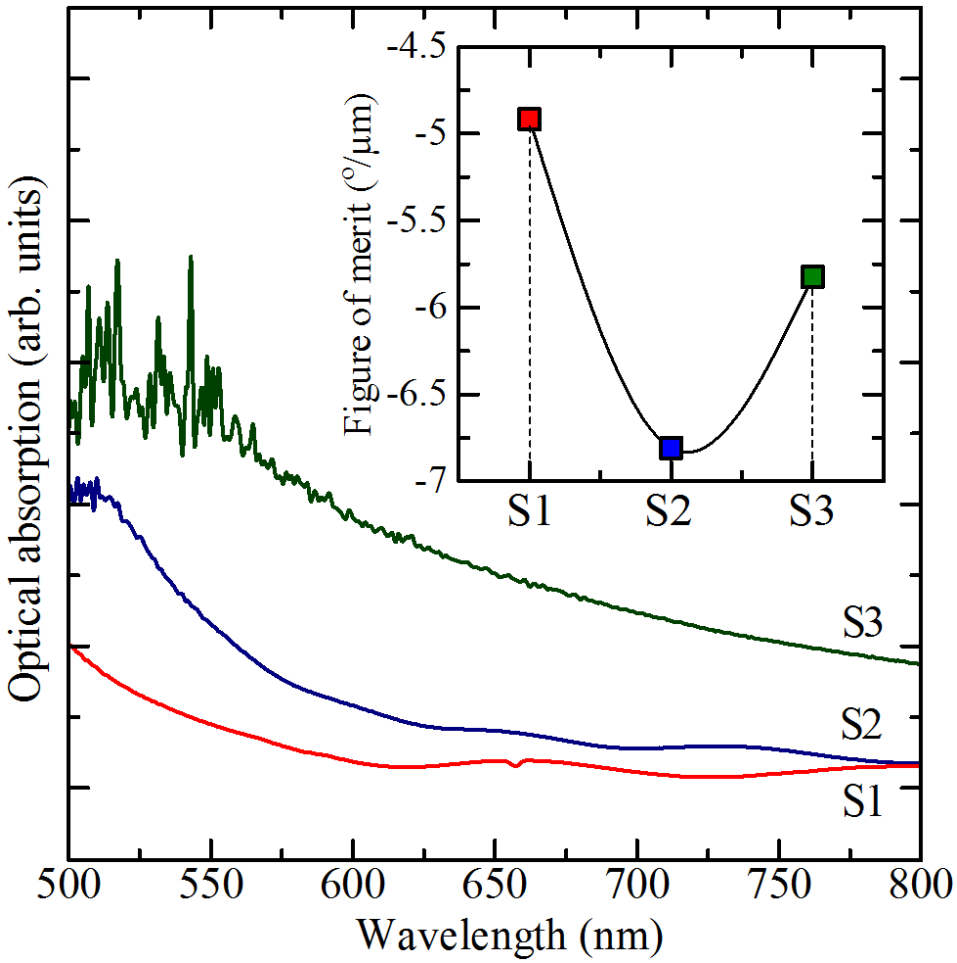

Figure 2.6.4. *Optical absorption spectra of prepared samples. The inset shows values of the FOM of the samples. One can clearly see high optical absorption of single-crystalline film which degrades FOM and in result Sample S2 possess the highest FOM.*

Figure 2.6.5 shows magnetization curves for S1, S2, and S3 (lower inset of Fig. 2.6.5) samples which were measured under external magnetic fields in the in-plane ($H_{\parallel}$) and out-of-plane ($H_{\perp}$) directions. The upper inset of Fig. 4 shows the configuration of the VSM measurement. All samples show in-plane easy axis which is crucial for MOI [67]. We came to this conclusion

because larger magnetization values obtained at weaker magnetic fields when the field is applied parallel to the surface of the film. The coercivity of samples was larger for the longitudinal configuration which also supports the claim that in-plane is the easy axis of the films.

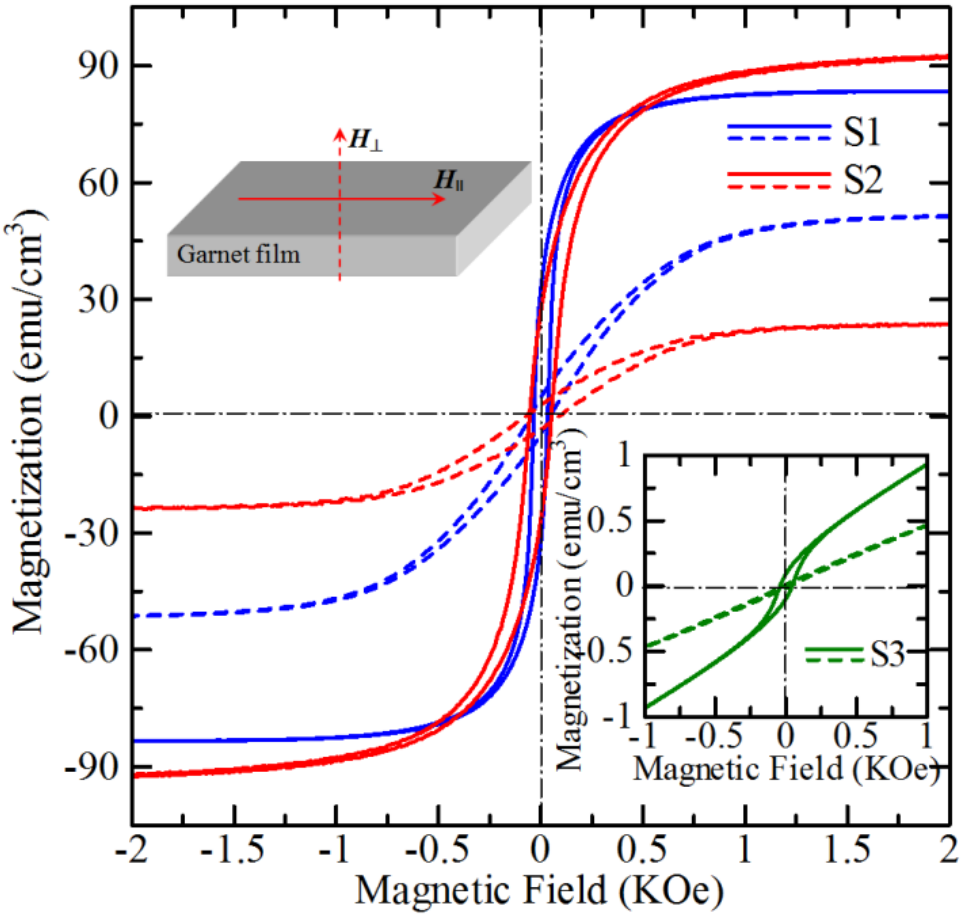

Figure 2.6.5. *Magnetization loops of the S1 and S2 samples under in-plane (solid lines) and out-of-plane (dashed lines) external magnetic fields. The upper inset shows configuration of VSM measurement. The lower inset shows the magnetization loop for the S3 sample under the same external magnetic fields.*

The curve for the sample S3 showed a paramagnetic effect, in which the film has not been saturated. While the curves for the samples S1 and S2 showed ferromagnetic behavior. This effect can be attributed to the difference of magnetic properties of the substrates on which samples have been grown. Monocrystalline GGG is paramagnetic in nature thus it has impact on the magnetic

properties of film while in case of borosilicate glass substrates contribution to the VSM data is very weak and it can be ignored [68-70]. However, our main purpose was to check magnetic anisotrpy of the films which was successfully done.

Taking into account that S2 possessed the highest FOM and an in-plane magnetic easy axis we used this sample as the magnetic field indicator for the MOI setup.

In summary we prepared high concentration $Bi_xY_{3-x}Fe_5O_{12}$ (x=2) thin films directly on glass substrates using low crystallization temperature. Though samples show secondary phases at the same time they possess a large figure of merit and in-plane easy axis which makes them attractive candidates for MOI. Using GGG as a substrate monocrystalline Bi-YIG film was prepared. XRD data clearly shows the garnet crystalline strucutre of prepared film.

§2.7. Properties of orthoferrite materials

The rare-earth orthoferrites with a general formula $RFeO_3$, where R is the rare-earth ion has attracted great research attention due to their magnetic, magneto-optical properties and transparency in the visible and near-infrared regions [71,72]. Particularly, yttrium orthoferrite (R=Y, $YFeO_3$) which has a distorted perovskite crystalline structure is an interesting material because of its wide application in sensors [73,74], magneto-optical devices [75,76] and photocatalysis [77].

Fig. 2.7.1 shows that orthorhombic unit cell of $YFeO_3$. $YFeO_3$ has a predominant antiferromagnetic interaction between iron ions but the alignment of iron moments is not perfectly antiparallel and there is a slight canting which comes from the antisymmetric Dzyaloshinsky-Moriya exchange interaction. This results in a small magnetization giving rise to weak ferromagnetism [78].

Fig. 2.7.2 shows the magnetic hysteresis loops of the nanocrystalline hexagonal and orthorhombic $YFeO_3$ samples [78]. The difference of magnetic properties of hexagonal and orthorhombic samples can be clearly noticed. Weak ferromagnetic properties of the orthorhombic sample can be observed but no saturation and paramagnetic behavior of a hexagonal sample can be detected.

Fig. 2.7.3 shows optical absorption of yttrium orthoferrites. In Fig. 2.7.3 we would like to show the difference of optical absorption spectrums in case of single-crystalline (Fig. 2.7.3 (a)) and polycrystalline yttrium orthoferrite (Fig. 2.7.3 (b)). $YFeO_3$ is one of the most transparent rare-earth orthoferrites. The extensive study on the optical and magneto-optical properties of rare-earth orthoferrites can be found in Ref. [80]. It was shown that there are similarities between magneto-optical spectrums and between optical absorption spectrums of most of the rare-earth orthoferrites. This can be explained by the fact that absorption and the FR in the optical region comes from the iron ions and not from the rare-earth ions. Fig. 2.7.4 shows the FR spectra of several rare-earth orthoferrites including $YFeO_3$ from the Ref. [81].

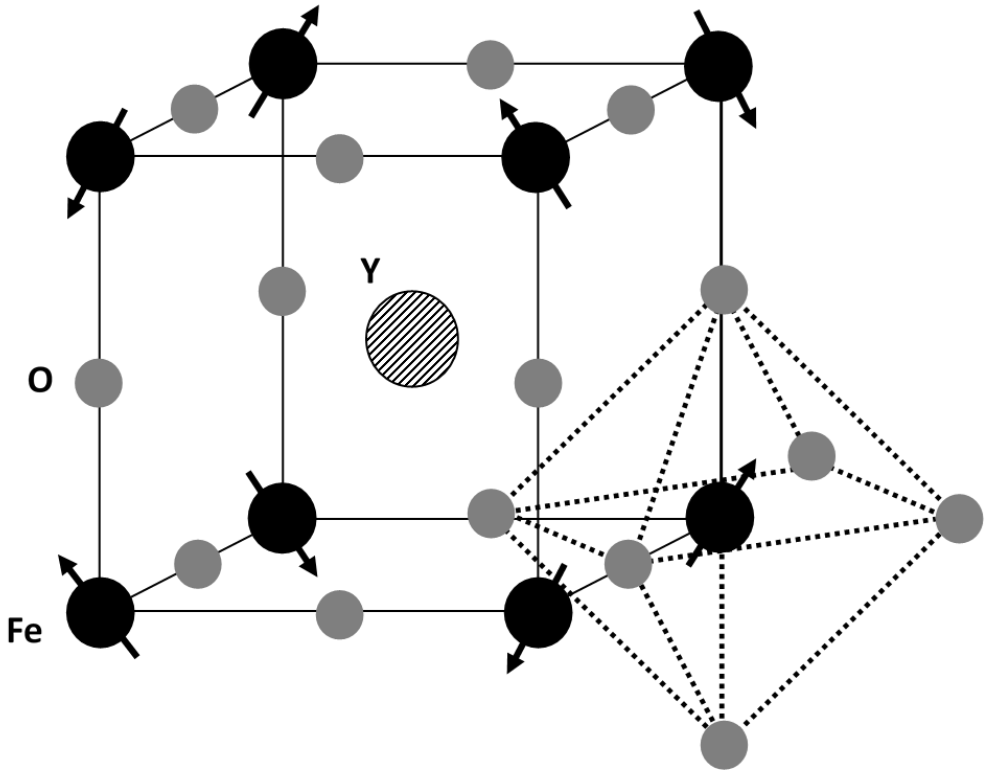

Figure 2.7.1. *Unit cell of $YFeO_3$. Fe: Iron ion, O: oxygen ion, Y: Yttrium ion. Arrows show directions of iron moments [78].*

However, there are several difficulties concerning synthesis of $YFeO_3$: the formation of secondary phases like $Y_3Fe_5O_{12}$ [82], crystallization in either orthorhombic (o-$YFeO_3$) or hexagonal (h-$YFeO_3$) structures depending on preparation conditions [79, 83, 71].

Most of the research have been carried on the bulk form of these materials because of the difficulties encountered in preparation of thin films [62]. To the best of our knowledge there are few reports available on the preparation of $YFeO_3$ thin films [62, 72, 73]. Schmool *et al.* in Ref. [62] described the preparation of the orthoferrite thin films on quartz substrates using pulsed-laser deposition method which requires high temperature (860 °C) post-deposition annealing treatment. In Ref. [72], the sol-gel synthesis method has been used. We used the MOD method for the preparation of $YFeO_3$ thin films.

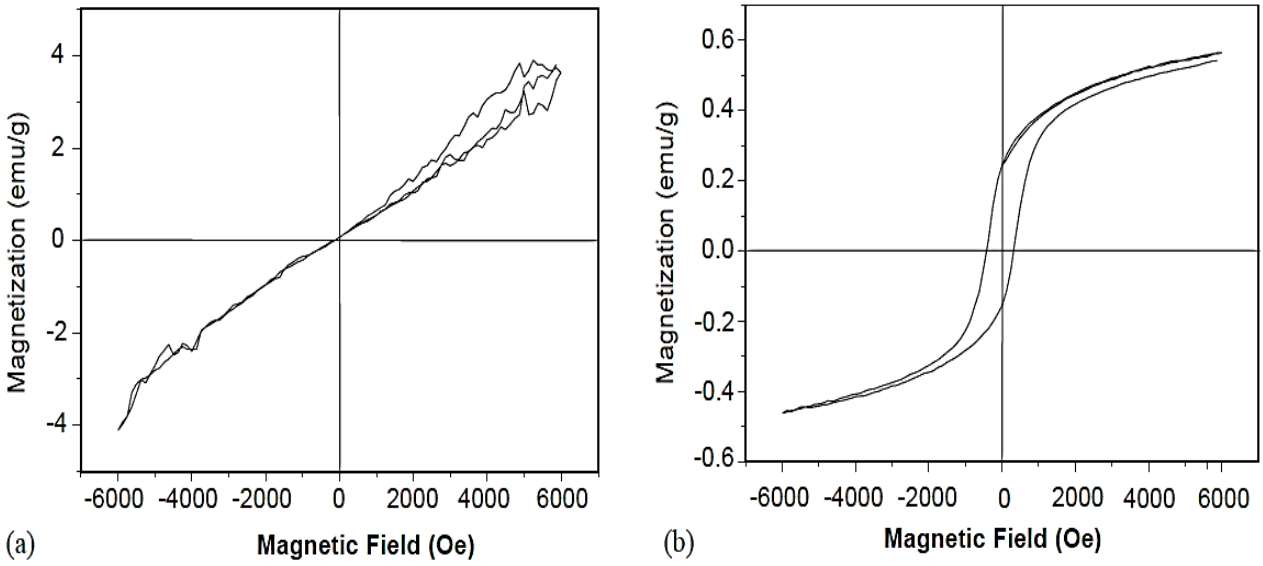

Figure 2.7.2. *Room temperature magnetization hysteresis loop of a $YFeO_3$ nanocrystal [79].*

As a substrate we used glass but the problem with the preparation of o-$YFeO_3$ thin films on such substrates is that the crystalline structure of o-$YFeO_3$ requires a relatively high temperature of crystallization [72]. High temperature or long time annealing process will cause the deformation of glass substrate. As we will show, MOD is a promising method for o-$YFeO_3$ thin films preparation on glass substrates because it does not require high temperatures or long time annealing to produce the desired material. Our results indicate that by substitution of yttrium with different concentration of bismuth the crystallization of the orthorhombic phase of $YFeO_3$ becomes possible.

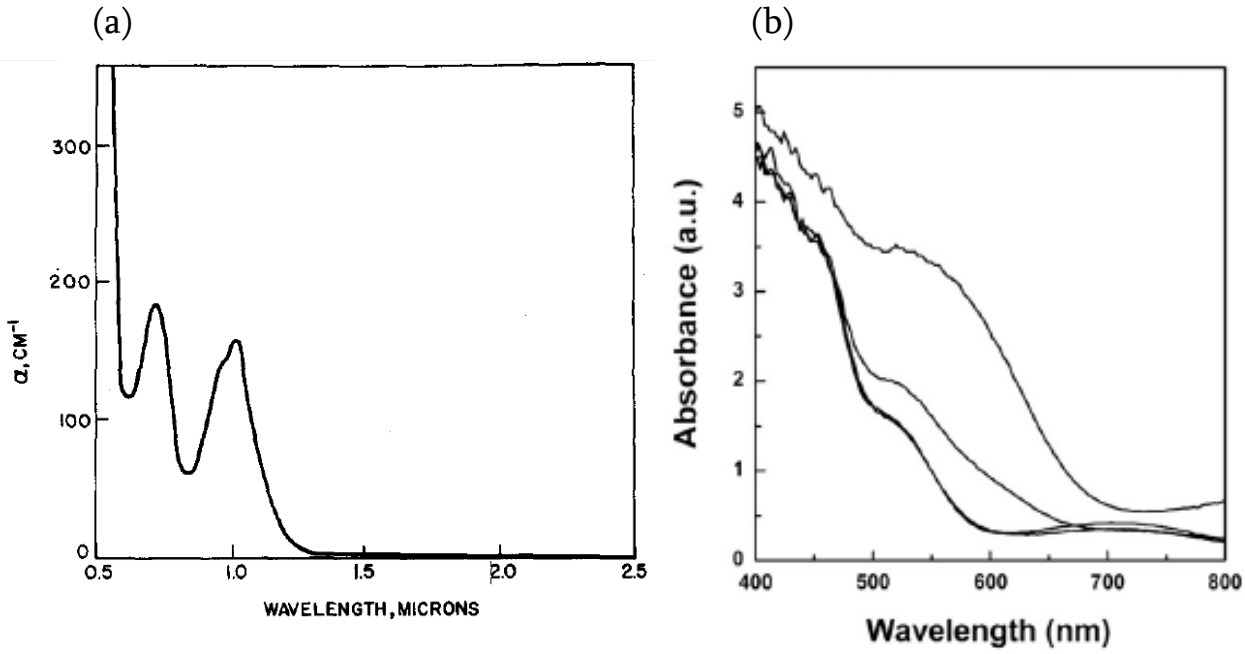

Figure 2.7.3. *Optical absorption spectras of a (a) single-crystalline $YFeO_3$ [80] and (b) polycrystalline yttrium orthoferrite [86]*

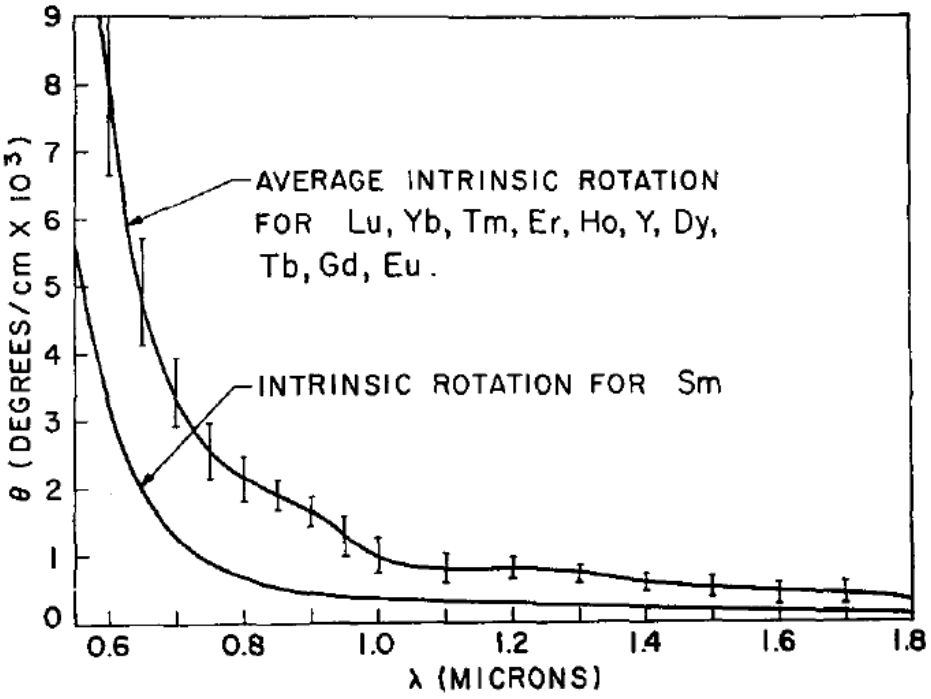

Figure 2.7.4. *FR versus wavelength for different rare-earth orthoferrites. The vertical lines shows the range of FR values for the different orthoferrites [81].*

In the next paragraph we will report the preparation conditions of $YFeO_3$ thin films by the MOD method and will discuss the impact of substitution of yttrium by different concentration of bismuth on crystallization conditions of thin films. We also investigated the magnetic, optical and magneto-optical properties of the prepared films.

§2.8. Preparation of yttrium orthoferrite thin films

Fig. 2.8.1 shows the MOD routine for the preparation of yttrium orthoferrite thin films. The strong effect of the doped different non-magnetic ions on the magnetic properties of the Bi-YIG gives the idea to research on the possible effects of the doped Bi^{3+} ions on the properties of $YFeO_3$.

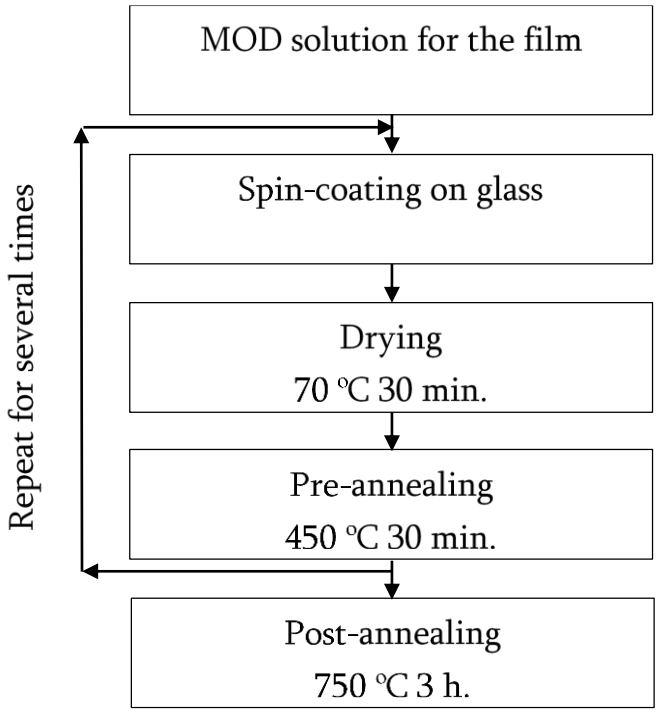

Figure 2.8.1. *Schematic diagram of MOD process for $YFeO_3$ thin films.*

Table 3 shows preparation conditions and properties of prepared samples. The same methods which have been used for the examination of the properties of Bi-YIG thin films, such as XRD characterization, VSM, FR and optical absorption measurements, have been applied for the orthoferrite thin films.

Polycrystalline samples were synthesized by the MOD method. To investigate the effect of substitution of yttrium with bismuth on the crystallization of yttrium orthoferrite thin films, the set of the samples (S1,S2-S7) with chemical formula $Bi_xY_{1-x}FeO_3$ (x=0, 0.1-0.5) have been prepared.

Table 3*.Preparation parameters, crystal structure and magneto-optical properties of synthesized samples.*

Sample	Concentration of Bismuth $Bi_xY_{1-x}FeO_3$ (x=)	Post-annealing temperature (°C) and duration (hours)		Phases observed by XRD	Faraday rotation (°/μm)
S1	0	650	3	Amorphous	-
S2	0	750	3	h-$YFeO_3$	-
S3	0.1	750	3	h-$YFeO_3$	-
S4	0.2	750	3	h-$YFeO_3$ + o-$YFeO_3$	-
S5	0.3	750	3	o-$YFeO_3$	0.3
S6	0.4	750	3	o-$YFeO_3$	0.3
S7	0.5	750	3	$Y_3Fe_5O_{12}$ + o-$YFeO_3$	0.58
S8	0.3	650	3	Amorphous	-
S9	0.3	700	3	h-$YFeO_3$ + o-$YFeO_3$	-
S10	0.3	700	4	h-$YFeO_3$ + o-$YFeO_3$	-
S11	0.3	750	2	h-$YFeO_3$ + o-$YFeO_3$	0.15
S12	0.3	750	4	h-$YFeO_3$ + o-$YFeO_3$	0.12

The sample thicknesses were about 0.4 μm. This thickness of the films is enough to find appropriate preparation conditions using XRD patterns of samples even with low intensity of diffraction peaks. All samples were dried at 70 °C, pre-annealed at 450 °C, post-annealed at 750 °C, and only sample S1 (x=0) was post-annealed at 650 °C. Figure 2.8.2 shows the XRD pattern of the prepared samples. There are no diffraction peaks for the sample S1 as expected because $YFeO_3$ requires a high crystallization temperature [72]. For the sample S2 diffraction peaks appear near 30° and 33° which can be assigned to the (101) and (102) planes of h-$YFeO_3$ [66,70]. But sample S2 possess weak ferromagnetic properties which can be related to the crystallization of other phases like o-$YFeO_3$ and $Y_3Fe_5O_{12}$. At the same time, S2 shows very strong orientation on (101) plane which can be explained by the strong hexagonal phase of the sample.

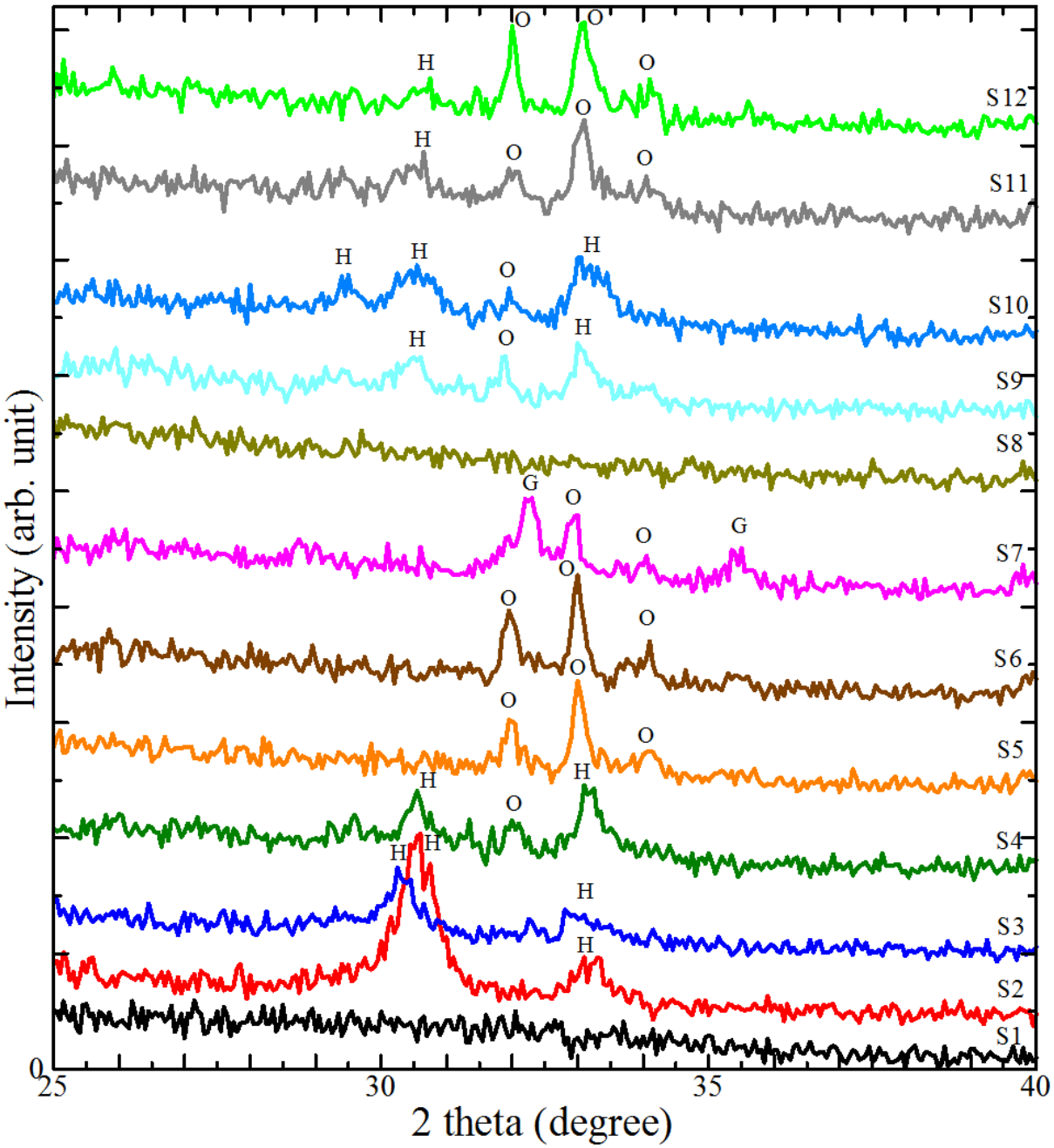

Figure 2.8.2. *X-ray diffraction patterns for the $Bi_xY_{1-x}FeO_3$ (x=) samples (T-post annealing temperature, t-post annealing time). S1: x=0, T=650 °C, t=3 h; S2: x=0, T=750 °C, t=3 h; S3: x=0.1, T=750 °C, t=3 h; S4: x=0.2, T=750 °C, t=3 h; S5: x=0.3, T=750 °C, t=3 h; S6: x=0.4, T=750 °C, t=3 h; S7: x=0.5, T=750 °C, t=3 h; S8: x=0.3, T=650 °C, t=3 h; S9: x=0.3, T=700 °C, t=3 h; S10: x=0.3, T=700 °C, t=4 h; S11: x=0.3, T=750 °C, t=2 h; S12: x=0.3, T=750 °C, t=4 h. Assignment of diffraction peaks are indicated as O: o-$YFeO_3$, H: h-$YFeO_3$, and G: $Y_3Fe_5O_{12}$.*

By starting the doping of bismuth, from the sample S3 XRD pattern one can see that hexagonal phase peaks start to become weaker, for S4 a weak diffraction peak appears at 32° which can be assigned to o-$YFeO_3$ [62]. For the XRD pattern of sample S5 3 diffraction peaks (200), (121), and (002) appeared in the region 31°-35° which correspond to o-$YFeO_3$. Sample S6 also shows diffraction peaks of the orthorhombic crystal.

To investigate the post-annealing temperature and time effect on the crystallization of o-$YFeO_3$ we prepared 5 additional samples: S8-S12 with x=0.3. Figure 2.8.2 shows XRD patterns of these samples. Sample S8 is amorphous, sample S9 shows (101), (102) XRD reflections corresponding to h-$YFeO_3$ and (200) which is an o-$YFeO_3$ reflection. These results indicate that post-annealing temperature is crucial for the crystallization of o-$YFeO_3$ thin films. Sample S10 was prepared using low temperature but long post-annealing time. It again shows a mixed phase structure with h-$YFeO_3$ diffraction peaks and a weak o-$YFeO_3$ peak. Samples S11 and S12 XRD patterns are composed of characteristic reflections of o-$YFeO_3$ with a h-$YFeO_3$ (101) peak near 30°. Phases observed in XRD patterns for all prepared samples indicated in Table 1.

Through the XRD pattern analysis of the S5 film, the lattice parameters were measured to be, a=5.905 Å, b=7.66 Å, c=5.256 Å, and V_{cell}=225.07 Å^3 which were in good agreement with data presented in Ref. [66]. The average grain size of the o-YFeO3 samples was calculated using Scherrer's equation and it was about 40 nm. Finally, we prepared a thicker film (about 0.8 μm thickness) using sample S5 preparation conditions. Figure 2.8.3 shows XRD pattern for that thicker sample which is in good agreement with data presented in previous reports of yttrium orthoferrite thin films [62, 72] and the intensity of the peak (121) is about 4 times larger comparing to sample S5 which is explained by the thickness of the samples.

Again magneto-optical activity of the samples was estimated by the measurement of FR angle. All measurements were carried at room temperature. The samples were magnetically saturated along the orthogonal direction to the film plane. It was shown by Kahn et al in Ref [75] for the most of the orthoferrites magneto-optical spectra of samples has similar shape which can be explained by the independence of spectra from the rare earth ions. It was concluded that main contribution to the magneto-optical spectra comes from the optical transitions related to the $Fe^{3+} - O^{2-}$ sublattices.

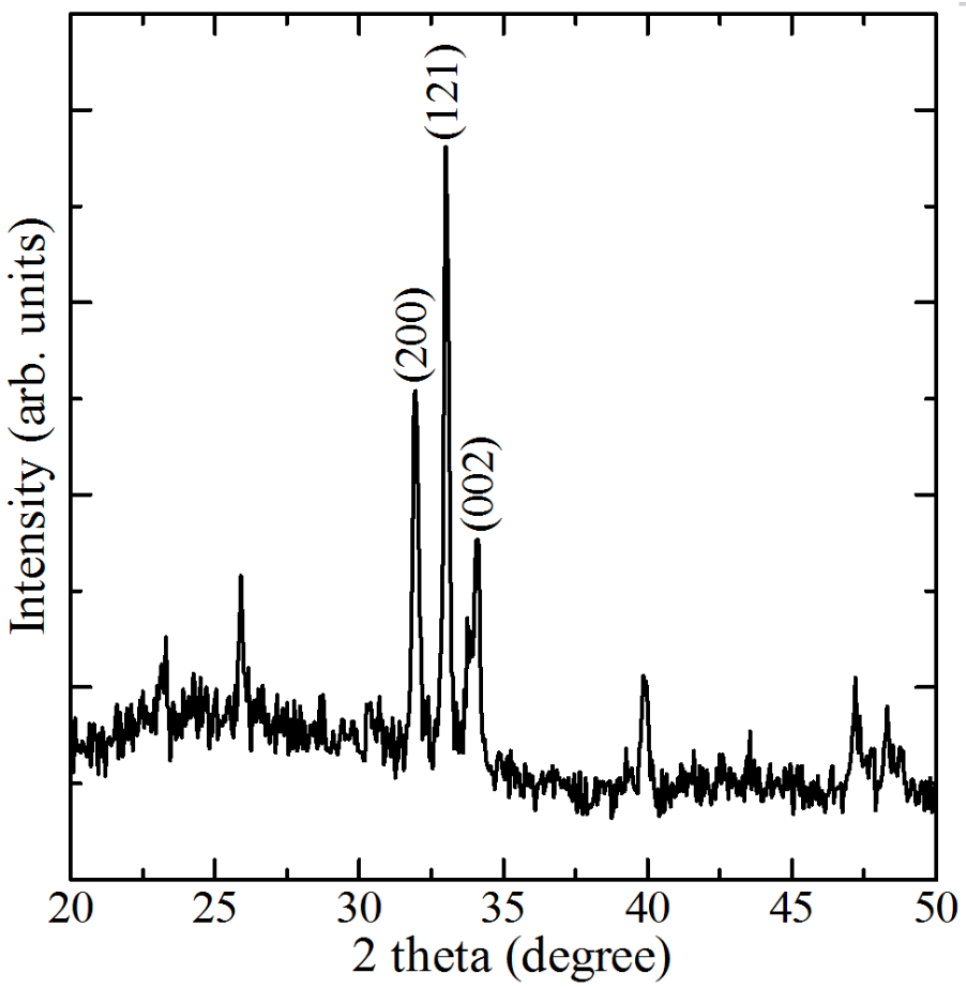

Figure 2.8.3. *X-ray diffraction pattern for the $Bi_xY_{1-x}FeO_3$ (x=0.3) film with 0.8 μm thickness. Main diffraction peaks of orthorhomic yttrium orthoferrite phase (002), (121) and (002) have been detected.*

Table 4. *Derived magnetic properties for S2, S5, and S7 samples obtained from VSM* measurements.

Sample	Configuration of VSM measurement					
	In-plane			Out-of-plane		
	Saturation magnetization M_s (emu/cm^3)	Saturation field H_s (KOe)	Coercivity H_c (Oe)	Saturation magnetization M_s (emu/cm^3)	Saturation field H_s (KOe)	Coercivity H_c (Oe)
S2	-	-	37	-	-	27
S5	26.4	1.8	104	-	-	87
S7	51	1.4	76	17	0.8	110

But we also need to consider that secondary phases generation in crystal structure of the samples such as $Y_3Fe_5O_{12}$ can have their influence on the magneto-optical properties of the films. For amorphous samples and films with strong hexagonal phase almost no FR detected. As it was expected results shows that only samples with strong orthorhombic and garnet phase possess relatively high magneto-optical activity and for the samples S5 and S6 it was measured to be about 0.3 °/μm and for sample S7 it was almost twice larger 0.58 °/μm. All the data of FR angles represented in Table 3.

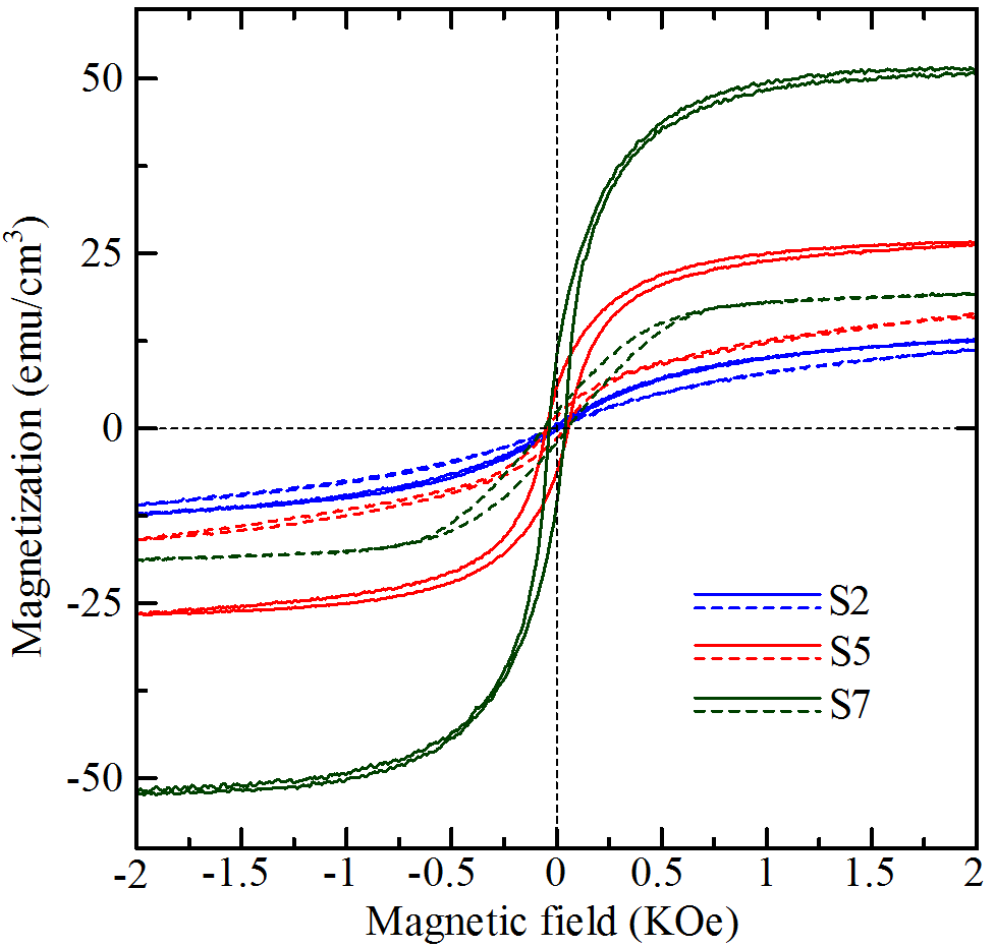

Figure 2.8.4. *Magnetization loops for the orthorhombic yttrium orthoferrite thin film (S5), for the films with a strong hexagonal phase (S2) and with a strong garnet phase (S7) under in-plane (solid lines) and out-of-plane (dashed lines) applied magnetic fields.Non saturating behaviour of a hexagonal S2 sample and weak ferromagnetic behaviour of a Sample S5 is in good agreement with a data presented in Fig. 2.7.2.*

Figure 2.8.4 shows the magnetization curves for films in the plane and the out of plane directions. We compared magnetic properties for the film with the strong orthorhombic phase (S5) with the sample showing strong hexagonal peaks (S2) and the sample with the strong garnet phase (S7). Because of weak magnetic properties of prepared samples we subtracted VSM data of the glass substrate and sample holder from VSM data of films In order to obtain accurate results. The data for coercivity H_c, saturation magnetization M_s and magnetic field H_s obtained from VSM measurements is summarized in Table 4. The highest M_s was measured for S7 for both in-plane and out-of-plane measurements. We assigned these results as we also did for high FR of S7 to the secondary garnet phase which appeared in XRD pattern of the sample. Sample S5 saturates at weaker magnetic when it's applied along the surface of the film which means S5 has in-plane easy axis. The value of coercivity of sample S5 is in good agreement with the data reported for yttrium orthoferrite powders in Ref. [83] but dramatically low compared to the data for the yttrium orthoferrite thin films reported in Ref. [84,85]. We attribute these results to the garnet phase which we think exists in the crystal structure of the sample. The main reasons for this suggestion is the in plane easy axis of garnet thin films prepared by the MOD method on glass substrates [42] and low coercivity of samples [85]. In Ref. [85] Schmool et al described how to identify phases appeared during preparation of orthoferrite thin films using SQUID magnetometry. . Compraed to Sample S5 in both configurations of the VSM measurement there was no saturation detected for the Sample S2, which indicates that $YFeO_3$ of different phases exhibits different magnetic properties [79].

Figure 2.8.5 shows optical absorption spectra of samples S2, S5 and S7. Sample S5 with the stronger orthorhombic phase shows lower absorption compared to the sample S2. These results can be confirmed also by the color of samples. S2 color is brown while S5 is yellow.

Optical absorption data of prepared samples is in good agreement with a data presented in Ref. [86] for polycrystalline hexagonal and orthorhombic orthoferrites which were prepared by sol-gel process. In Ref [88] optical properties of 14 different rare-earth orthoferrites in bulk crystal form have been discussed. Because of the polycrystalline nature of our prepared samples there were no chacatrestical absorption bands of monocrystalline orthoferrites in optical spectra. It was evaluated that polycrystalline thin films contain higher number of defects by ~5 orders of

magnitude comparing to bulk materials which dramatically alters optical properties of samples [88]. However prepared films are quiet transparent in visible light region which gives possibility to use them in magneto-optical experiments.

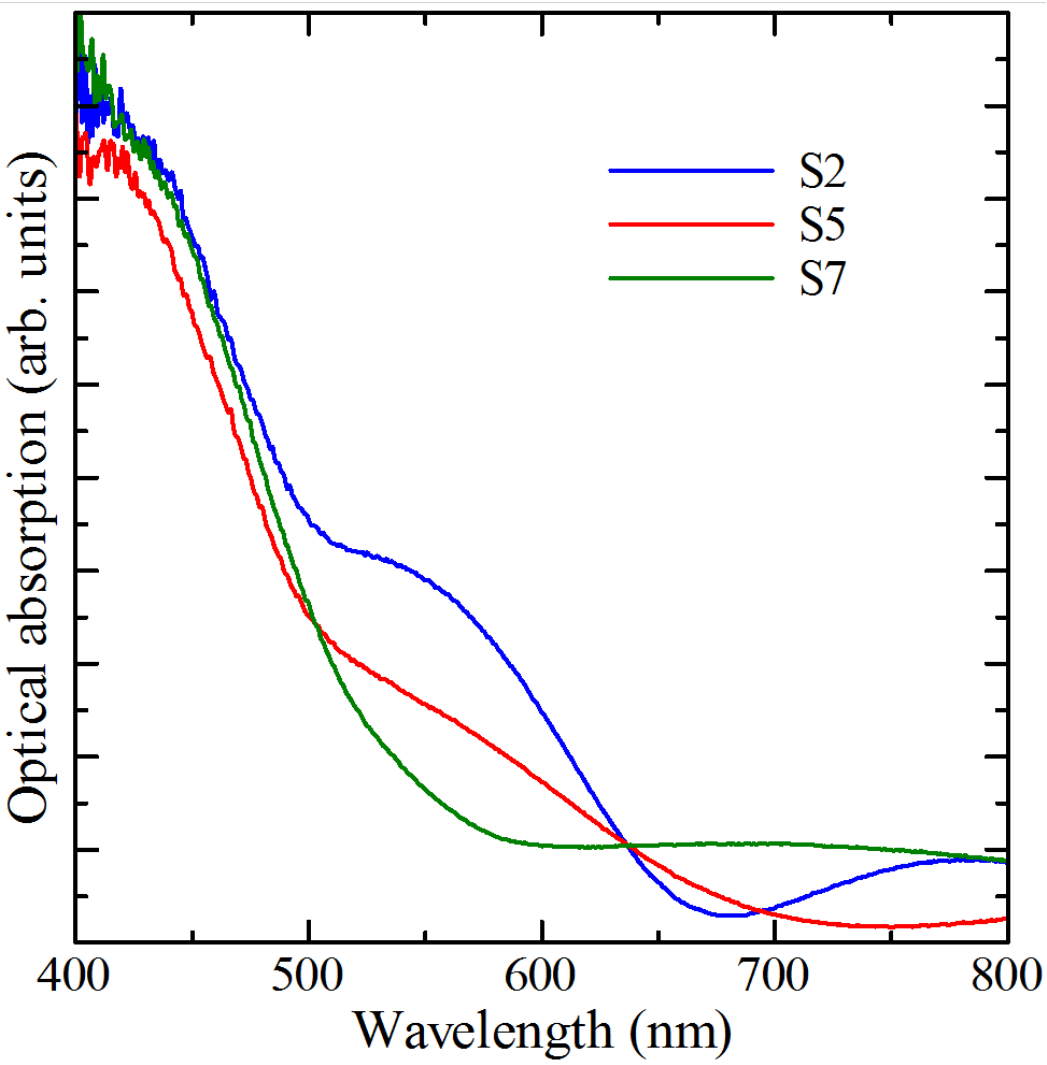

Figure 2.8.5. *Optical absorption spectras for the samples S2, S5, and S7. Similiraty of spectrum with a data presented in Fig. 2.7.3 (b) can be noticed.*

To sum up, the crystallization of $YFeO_3$ thin films substituted by different concentrations of bismuth prepared by the MOD method on a glass substrate has been studied. Crystallization of orthorhombic phase of $YFeO_3$ at 750 °C post-annealing temperature becomes possible with increasing concentration of substituted bismuth, particularly for the samples $Bi_xY_{1-x}FeO_3$ (x=0.3 and x=0.4) [70]. All the films are polycrystalline and have magnetic anisotropy parallel to the film

plane. From the VSM data we can suggest that the main contribution to the magnetic properties of the films comes from crystallization of a secondary garnet phase. Samples with a strong orthorhombic phase have lower optical absorption comparing to the films with strong hexagonal phase.

CHAPTER 3. MAGNETO-OPTICAL VISUALIZATION

§3.1. Introduction to magneto-optical imaging

MOI tools are very important in the field of nondestructive visualization of magnetic fields. As we said there are 2 types of magneto-optical imaging: based on Kerr and Faraday effects. The technique which utilizes FE is presented further. To undesrtand how MOI is possible using FE lets look to the Fig. 3.1.1, where the magneto-optical indicator is illustarted. The MO indicator consists of three different layers: a transparent substrate layer, magneto-optical Bi-YIG layer which was grown on a substrate by MOD method and finally Al mirror layer with a 40 nm thickness which was thermally evaporated on magneto-optical layer. Then MO indicator is placed on the SUT. Lets assume, SUT is a material that induces magnetic field in different directions. This eventually causes the change of magnetization of MO indicator. If we illuminate MO indicator with a linealry polzarized light the latter changes its polarization because of FE. By monitoring a change of the polarization of light using optical sensors such as charge coupled device (CCD) camera we can visualize local magnetic field distibution.

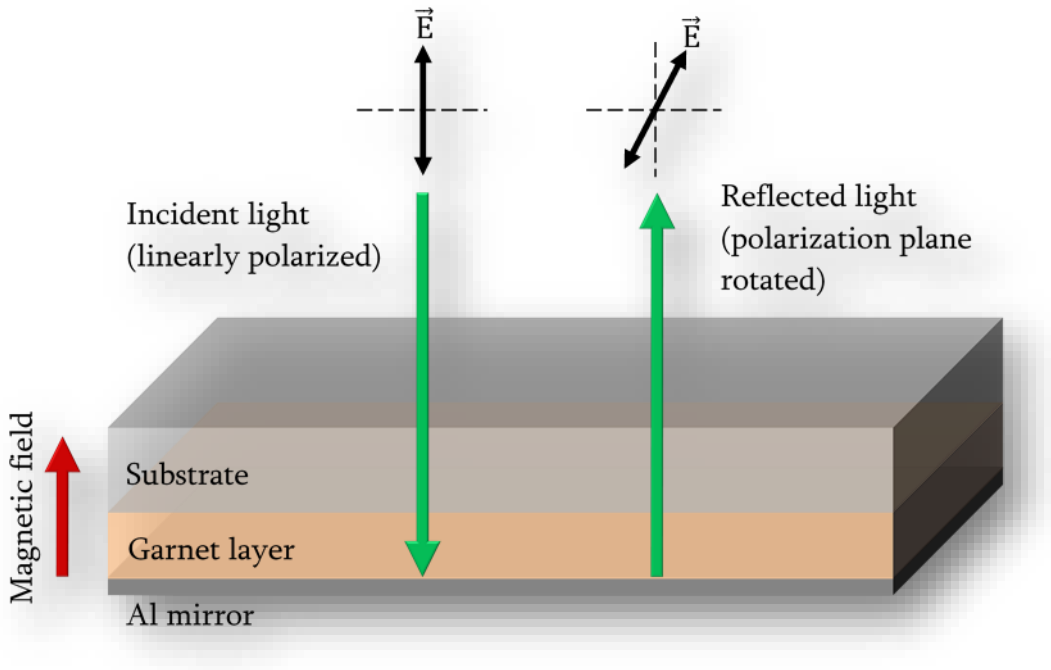

Figure 3.1.1. *The schematic diagram of the indicator film. Incident linearly polarized light is rotated by FR twice after exiting the garnet layer.*

Main advantages of magneto-optical visualization are the following:

1. Using magneto-optical microscopy technique of the visualization of magnetic fields we can reach the optical resolution limit, where the spatial resoltion of magneto-optical images can be about 0.5 μm [88].
2. The response of the change of the polarization of the light to the magnetic field is very fast (~GHz) so the real-time imaging of magnetic field distrubution can be achieved by using rapid responsible optical instruments [89].
3. One of the most impornat advantages of magneto-optical imaging comapring to other magnetic field detection methods such as SQUID or MFM is that the magneto-optical visualization is simple, easy to implement and inexpensive. The experimental setup which will be presented in next paragraph does not require any expensive instruments such as a precise stage or specially designed sensor and a complicated data analysis of the measurement results [2, 3, 91].
4. Large imaging area which can be accomplished using indicator films with large surface area. Especially MOD method gives the possibilty to easily prepare such indicators just by chosing the appropriate size of the substrate and adjusting the conditions of deposition of MOD solution.

It was reported by Kato *et al.* in Ref. [11] that with the use of Kerr rotation microscopy it was possible to detect the spin Hall effect in Gallium Arsenide (GaAs) and Indium Gallium Arsenide (InGaAs) semiconductors. Spin Hall effect, which is the spin accumulation with opposite directions on the lateral surfaces of an electric current currying sample, was predicted by Russian physicists Dyakonov and Perel in 1971 [91]. Figure 3.1.2 shows the experimental system and the two dimensional magneto-optical images of the GaAs film. The Fig. 3.1.2 (b) shows spin polarization localized at the 2 edges of the film with opposite directions. Spin density n_s is proportional to magneto-optical Kerr rotation. These results indicate that for in the new emerging field of spintronics magneto-optical visualization can be a great tool for the nondestructive testing of spintronic devices.

MOI finds its application also in the field of inspection of surface cracks in commercial and military aircrafts [92, 93]. This technique is based on eddy current excitation. So the magneto-optical visualizer gives the current images of corrosion and subsurface cracks.

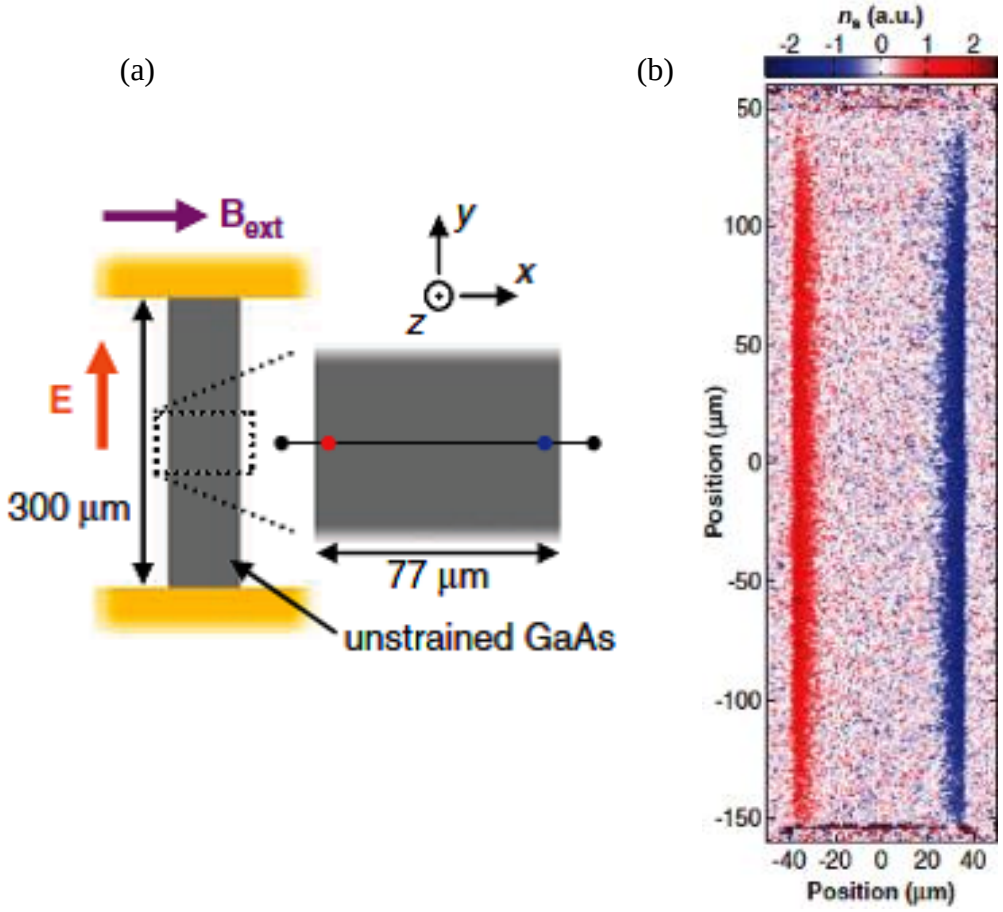

Figure 3.1.2 *(a) Schematic diagram of a GaAs sample and the experimental system, (b) two dimensional image of spin density n_s. B_{ext} - external magnetic field, E - alternating electric field. Experiments were done for the unstrained GaAs at T=30K temperature. From Ref. [11]*

MOI technique also allows to investigate the magnetic properties of superconductors. In particular magnetic vortex imaging becomes possible. The extensive studies on this topic can be found in Ref. [94-98].

The magnetic field created by a microwave propagating through a microstrip line was measured using magneto-optical measurement technique [99]. So the use of magneto-optical mediums makes it possible to measure not only static magnetic fields but also the magnetic field distribution of GHz frequency range.

As indicators for the magneto-optical imaging setup we will use films prepared by the condtions for the S2 Bi-YIG thin film presented in paragraph 2.6, because these films have superior magneto-optical properties comparing to other films prepared by MOD method.

In the next paragraph MOI setup will be presented. Several applications such as imaging of magnetic domains of magnetic materials and real-time detection of magnetic fields will be presented using synthesized magneto-optical indicator films.

§3.2. Magneto-optical imaging setup

The schematic diagram of MOI setup which utilzes cross polarization approach is shown in Fig. 3.2.1. Fig. 3.2.1 (b) illustrates the photograph of imaging setup. As a light source we used Thorlabs LED M530L2 which has a dominant wavelength of 530 nm. From the source the light passes through the polarizer then by using a beam splitter it is directed to the indicator placed in front of the SUT. The plane of the linearly polarized light rotates by θ_F under the influence of the magnetic field which is orthogonally directed to the surface of the film. Then the light is reflected by the mirror deposited on the film and passes through the magneto-optical medium for the second time [100].

Because the magneto-optical medium is non-reciprocal the plane of the linearly polarized light rotates by θ_F in the same direction one more time. Hence the light exits the indicator rotated by $2\theta_F$ which is finally received by the CCD camera through the beam-splitter and the analyzer. Polarizer and analyzer are installed in the crossed position. Using Jones calculus it is possible to derive measured light intensity by CCD camera. In the Jones calculus, polarized light and linear optical elements are represented by Jones vector and matrices, respectively, and the polarization of the light passed through an optical element calculated by taking the product of Jones matrix of the optical element and Jones vector of the incident light. In the cross polarization technique of a measurement the detected light intensity by CCD camera will be given by Malus' law:

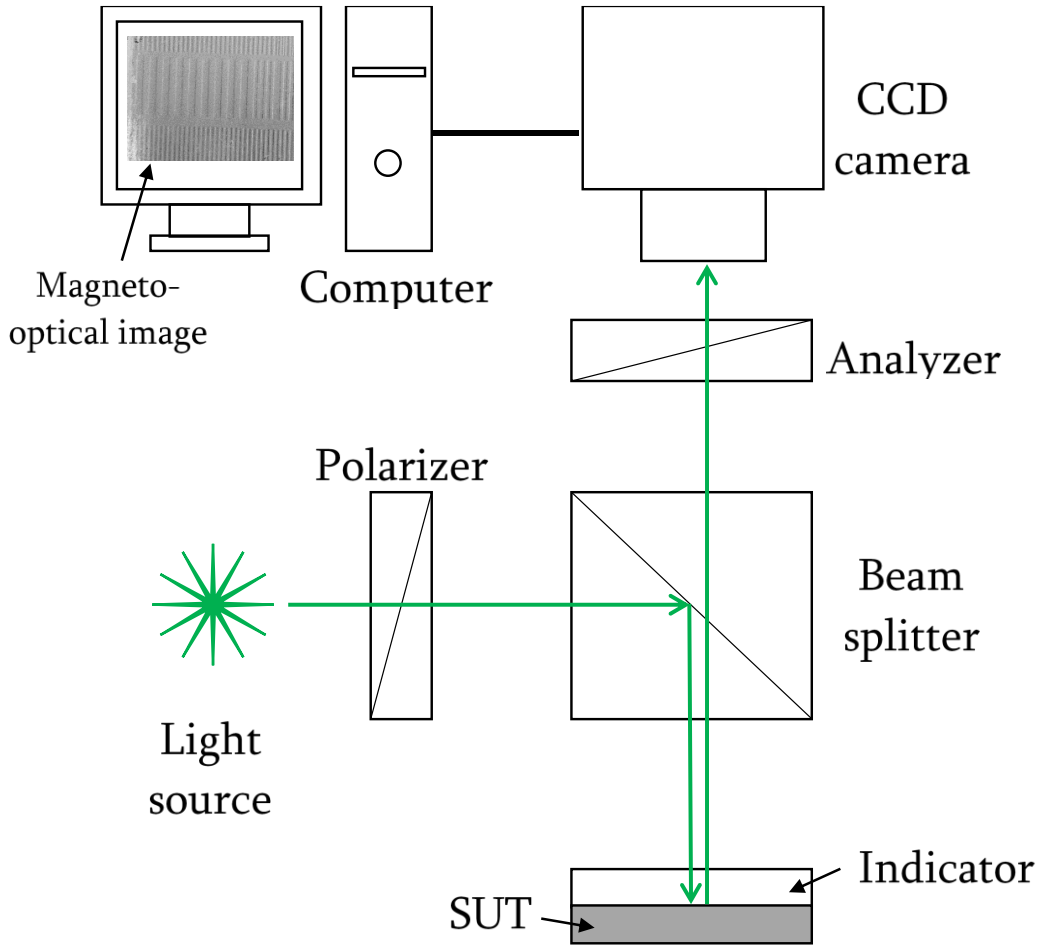

(a)

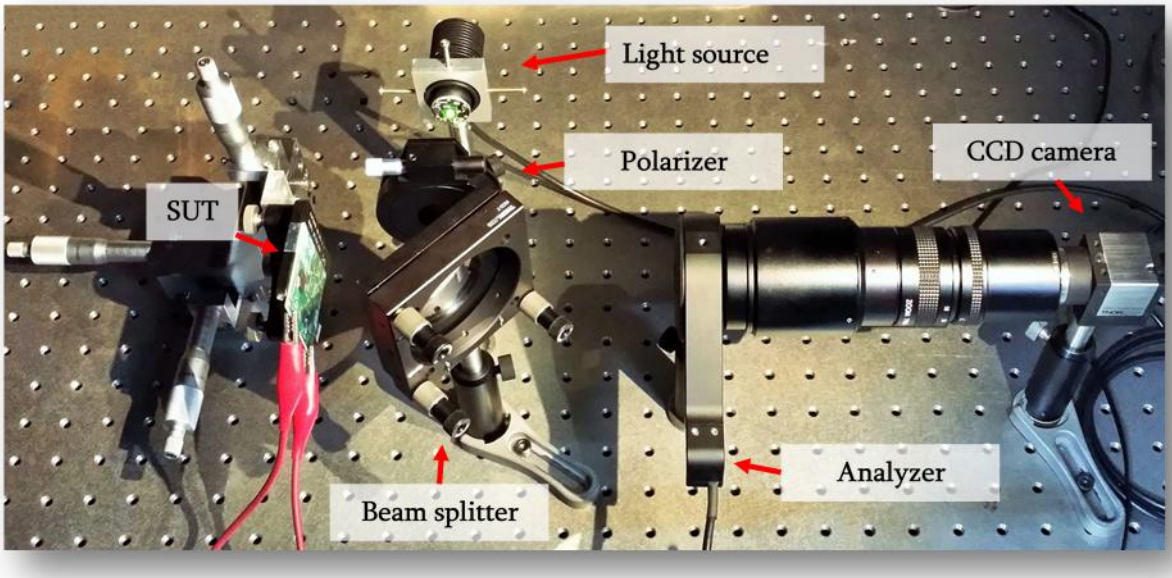

(b)

Figure 3.2.1. *The schematic diagram (a) and the photograph (b) of the magneto-optical imaging setup.*

$$I = I_0 \cos^2 2\theta_F \quad (3.2.1)$$

If the analyzer is rotated at an angle of $\pi/2$-θ compared to the polarizer, the measured light intensity will be:

$$I = I_0 \sin^2(\theta - 2\theta_F) \quad (3.2.2)$$

where I and I_0 is the detected and the initial light intensity, respectively, and θ_F is the FR angle.

§3.3. Magneto-optical visualization of static magnetic fields

First we tried to check the range of the magnetic field values which can be detected by the prepared indicator films (dynamic range of the MOI setup). Fig. 3.3.1 shows the magnetic field source with a ring shape which we used as a SUT. The intensity of magnetic field changed from 0-1000 Oe by applying appropriate range of the current using programmable power supply.

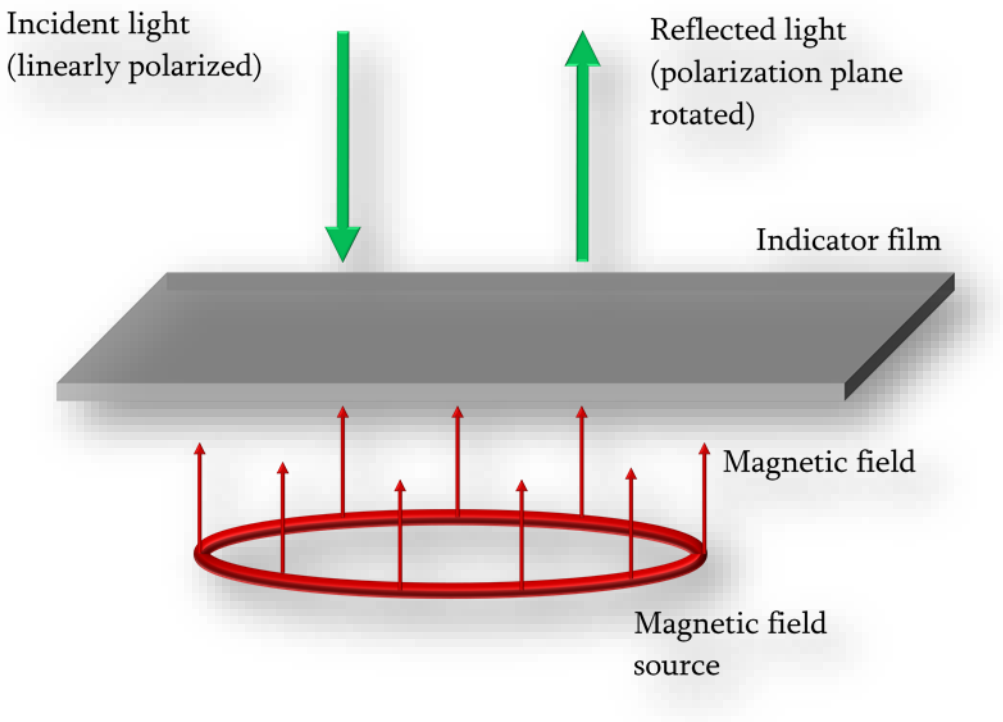

Figure 3.3.1. *The schematic diagram of the magneto-optical imaging of the ring shape magnetic field source.*

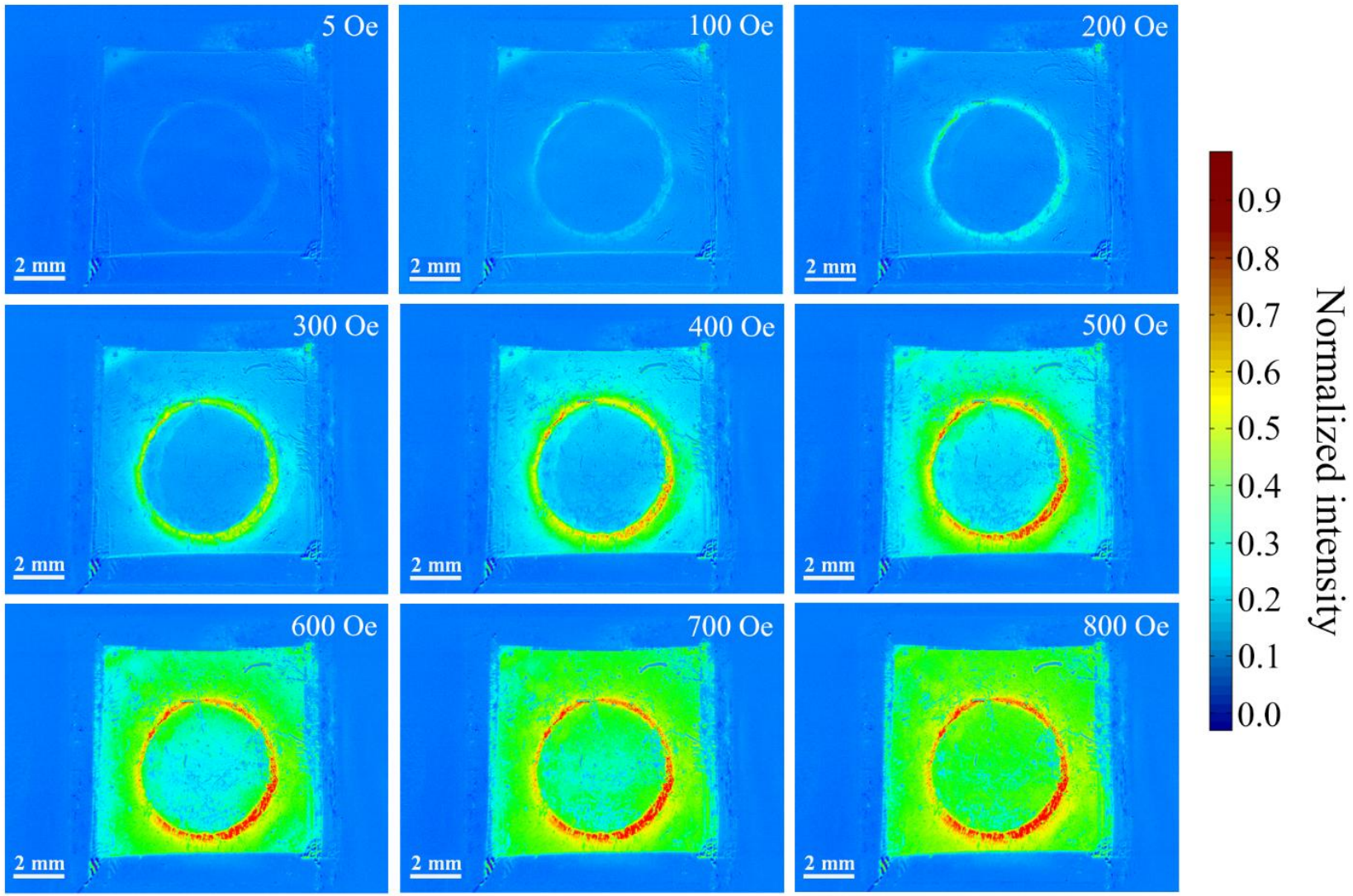

Figure 3.3.2. *Magneto-optical images of magnetic field distribution with S2 indicator film created by a ring shape electromagnet with different magnetic field intensities [100]. Saturation of the magneto-optical image can be noticed after 700 Oe magnetic field values.*

Because of FE only the normal component of the magnetic field can be detected. For the calibration of results we subtracted the background image, which was taken when the applied magnetic field was zero, from the image taken with applied magnetic field. The measurement speed of MO imaging is about 10 ms per image. In order to increase sensitivity of the visualization and to improve signal-to-noise ratio, an averaging process was applied. The minimum detectable magnetic field intensity was about 5 Oe (Fig. 3.3.2). Each presented image is the result of averaged 1000 images with 1024x768 pixels resolution. Size of each pixel is about 4.65 μm^2.

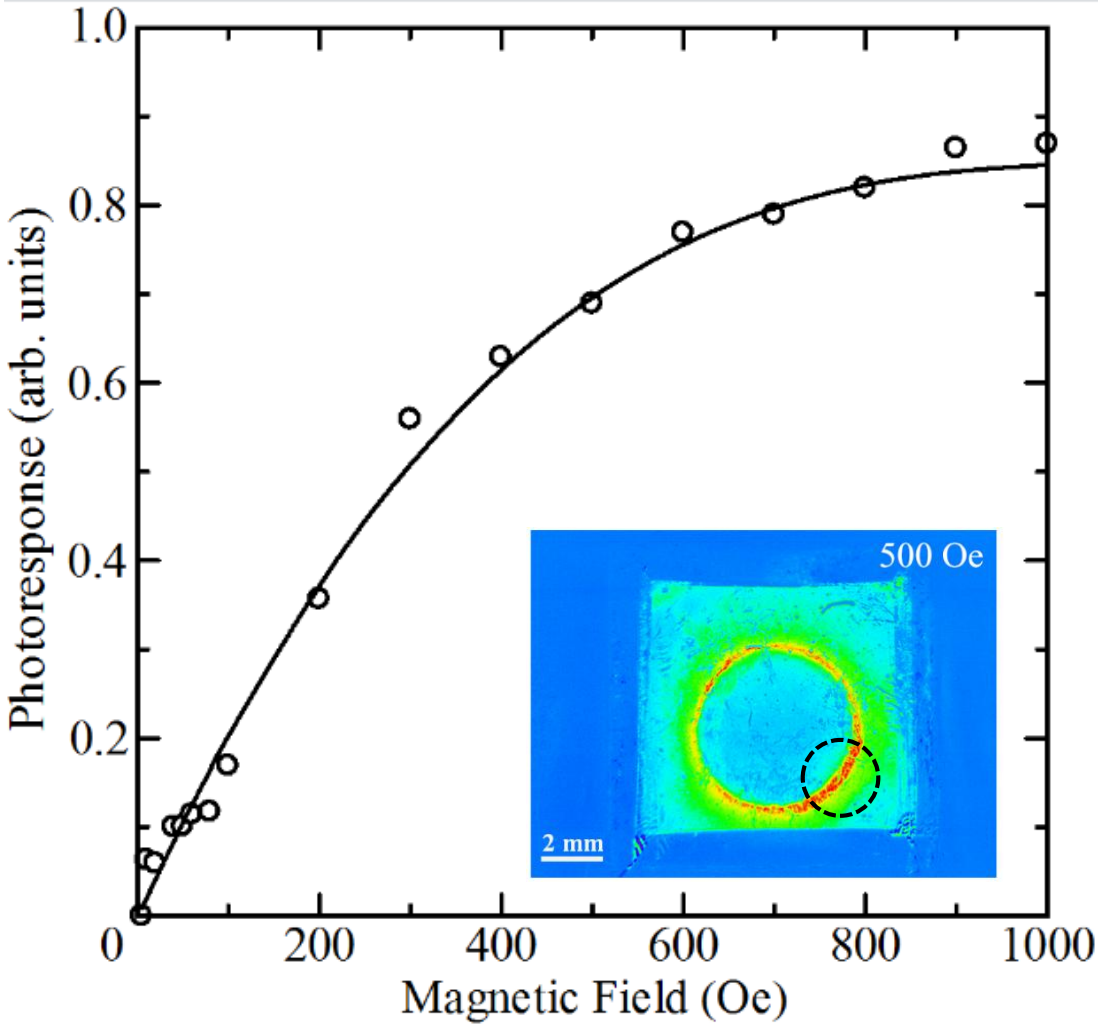

Figure 3.3.3. *(a) Illustration of the geometrcial range where photoresponse was averaged, (b) average photoresponse of S2 film around the highest detected intensity vs. applied magnetic field.*

Figure 3.3.3 shows the measured average photoresponse of the CCD camera around the highest detected intensity (Fig. 3.3.3 inset shows that range) dependence on the magnitude of the normal component of the magnetic field. As can be seen from the figure, the signal is almost saturated at a value of 800 Oe. This value is the upper value of the magnetic field measurement range of the developed imaging system. In order to increase the linear range (0-800 Oe), further research on the composition of MOD solutions and preparation conditions needs to be done. The minimum detectable magnetic field value i.e. sensitivity, can be improved by samples with higher FOM. The upper value can be increased by the control of magnetic properties which can be achieved by the change of chemical composition of the garnet thin films. For example by adding several magnetic materials as buffer layers during the preparation of $Y_{0.5}Bi_{2.5}Fe_5O_{12}$ on glass substrates by the MOD method, FR can be saturated at higher intensities of external magnetic field in comparison with S2 [49].

§3.4. Magneto-optical visualization of magnetic domains

The black magnetic stripe on a general credit card contains magnetized material with domains aligned in two opposite directions. In this way information is stored in the structure of the magnetic domains. Figure 3.4.1 shows the schematic representation of the principle of measurement of the magnetic domains using an indicator film. The magnetization directions of magnetic domains in the magnetic stripe are aligned parallel to the indicator film which means there is no FR detected by the CCD camera. However, out-of-plane stray field is formed at the magnetic domain walls because of the opposite directions of magnetization. At the medium of the indicator film, with this stray field, FE appears, which affects the polarization of the light detected by the CCD camera. Parallel and anti-parallel magnetic fields to the direction of the propagation of the light make areas of detected image dark and bright respectively [100].

Figure 3.4.2 is the illustration of a structure of a general credit card and its magnetic stripe which consists of 3 tracks. Each track contains different kind of data. For example because of the higher bit density of Track 1 comparing to the Track 2 it is the only track that may contain the cardholder's name. Track 3 is less used for credit and debit cards.

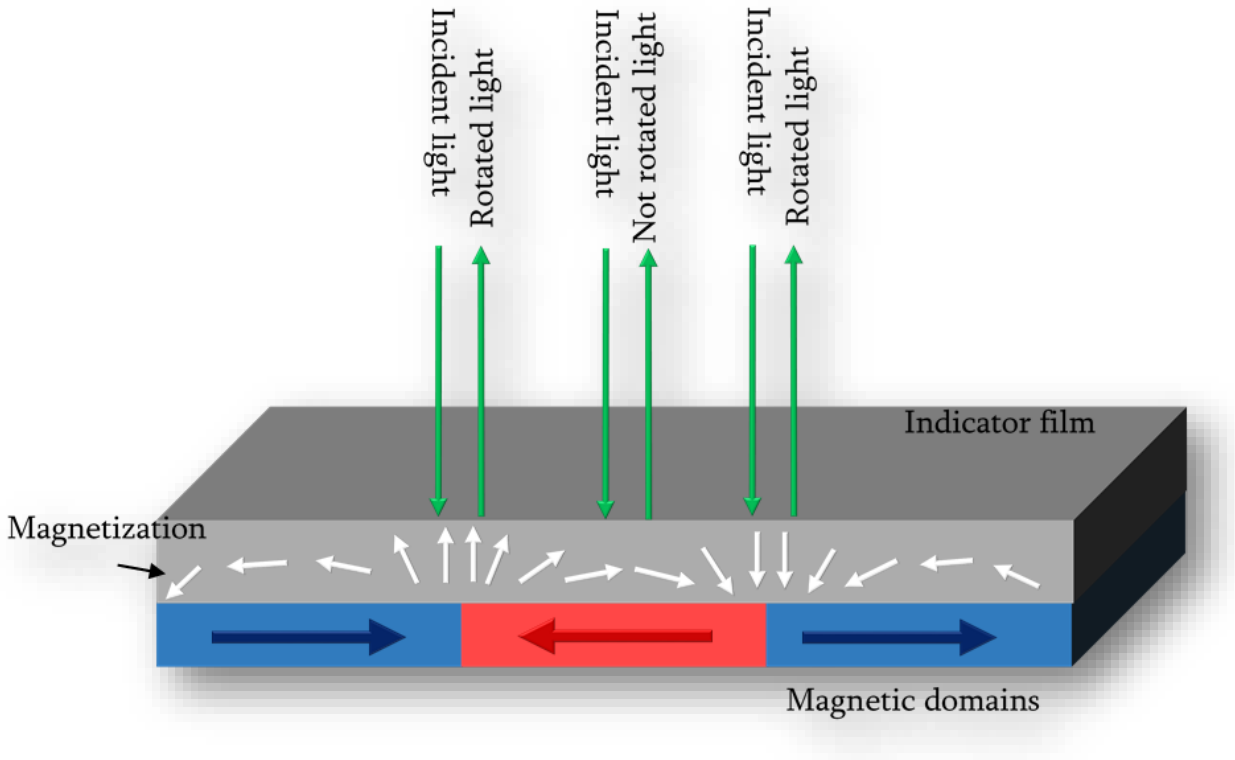

Figure 3.4.1. *Illustration of the principle of measurement of the magnetic domains using an indicator film. Depending on the magnetization of a garnet layer (region with grey color) light changes its polarization state. After exiting the garnet layer light is detected by CCD camera.*

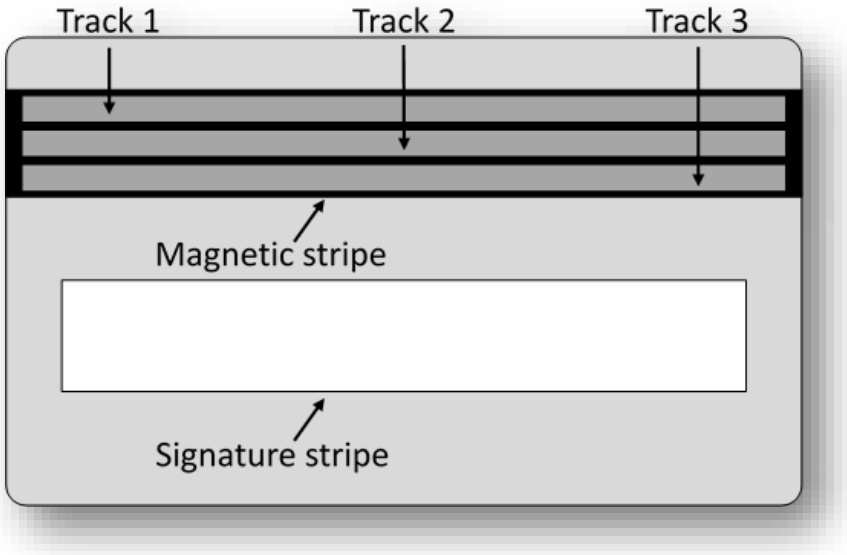

Figure 3.4.2. *Schematic representation of a general credit card and magnetic stripe. Track 1, 2 and 3 of a magnetic stripe possess the information in a form of magnetized magnetic domains with different density.*

Figure 3.4.3 (a) shows a magnetic stripe on which a garnet indicator film is placed. Using the magneto-optical imaging system we visualized magnetic domains of the credit card as shown in Fig. 3.4.3 (b). Magneto-optical image was the subtraction result of two images which were taken when the analyzer was rotated 2° clockwise and counter clockwise perpendicular to the polarizer.

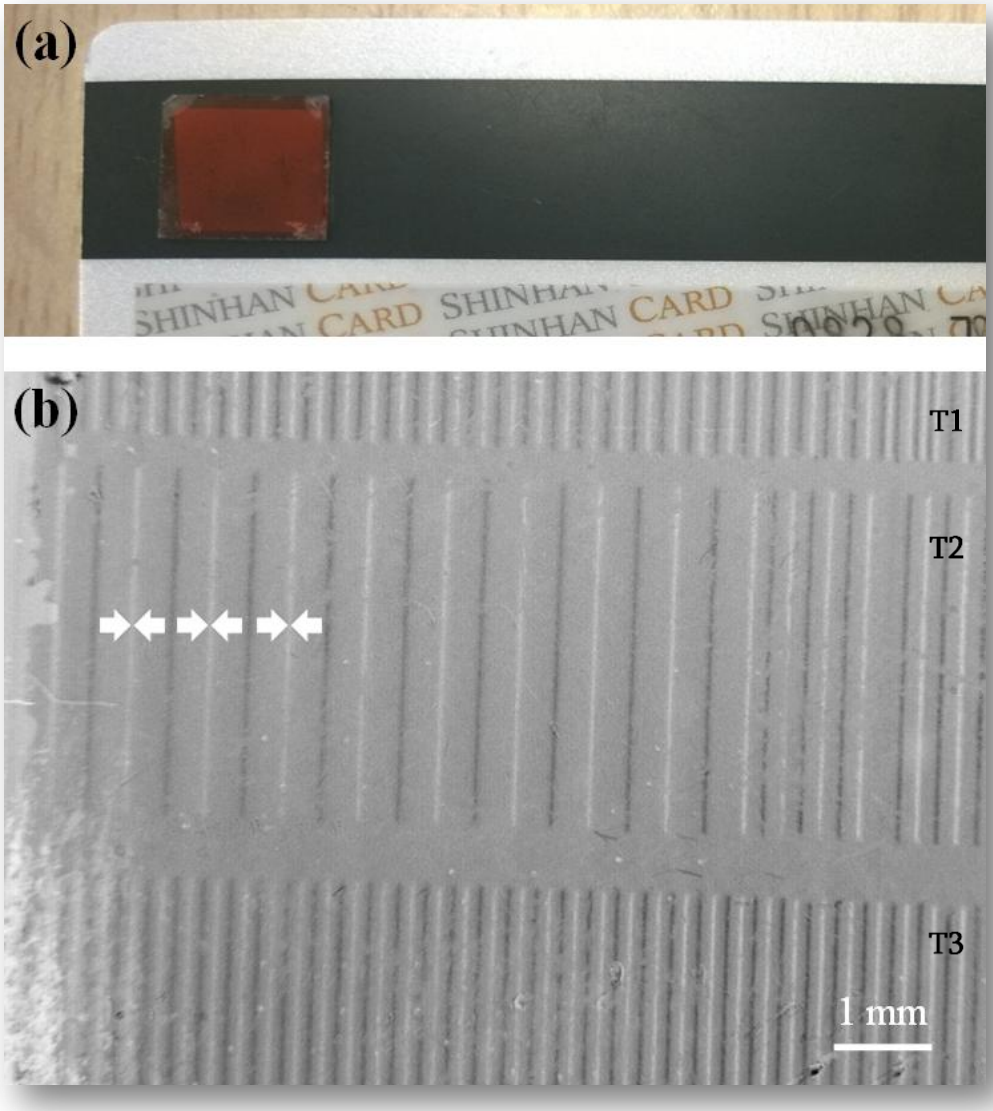

Figure 3.4.3. *(a) Photograph of the credit card studied with the indicator film and (b) magneto-optical image of the magnetic domains in the magnetic stripe of the credit card. White arrows indicate the direction of magnetizations of magnetic domains. T1, T2 and T3 indicate postions of Track 1, Track 2 and Track 3 respectively.*

Fig. 3.4.4 shows the process of subtraction of magneto-optical images and orientation of optical axes for polarizer and analyzer. Although magneto-optical images can be seen in real-time (see Fig. 3.4.4 (b), (d)) without subtraction, this simple step gives the image with high contrast. Arrows on Fig. 3.4.3 (b) indicate the directions of the magnetization of magnetic domains.

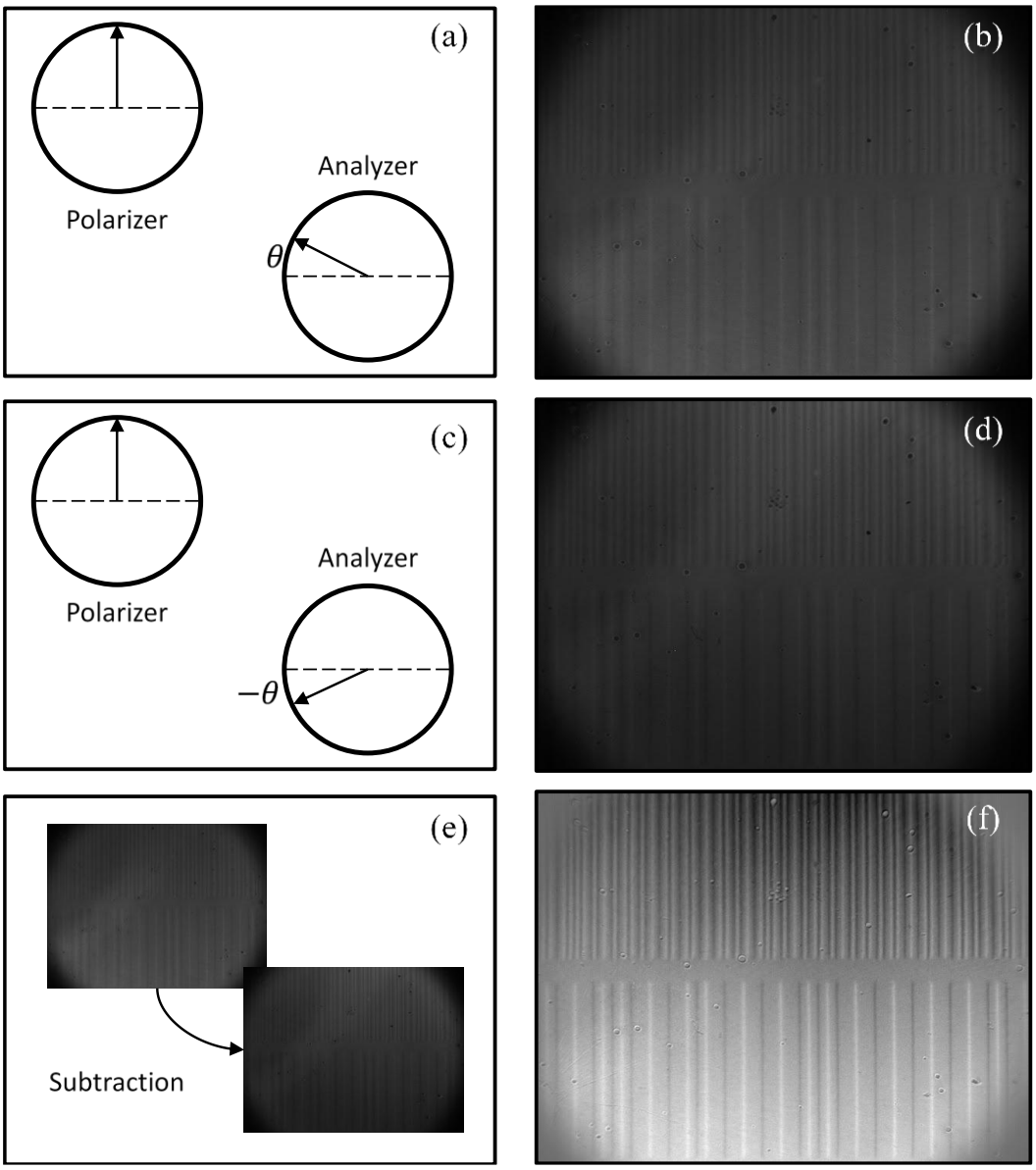

Figure 3.4.4. *(a) Analyzer is rotated by 90-θ to the polarizer, (b) magneto-optical image for 90-θ position, (c)) Analyzer is rotated by 90+θ to the polarizer, (d) magneto-optical image for 90+θ position, (e) subtraction of (b) and (d) magneto-optical images, (f) final magneto-optical image*

From Fig. 3.4.3 (b) we can see the higher density of domains of Track 1 comparing to the Track 2. So the gemotrical information for the quality control of credit cards can be obtained. Defects of worn out cards can be clearly detected this way.

Fig. 3.4.5 shows the amplitudes of magnetic stray field created by oppositely directed magnetic domains for Track 1 and Track 2. This way a quality control and an investigation of frauding or other kinds of manipulations can be done.

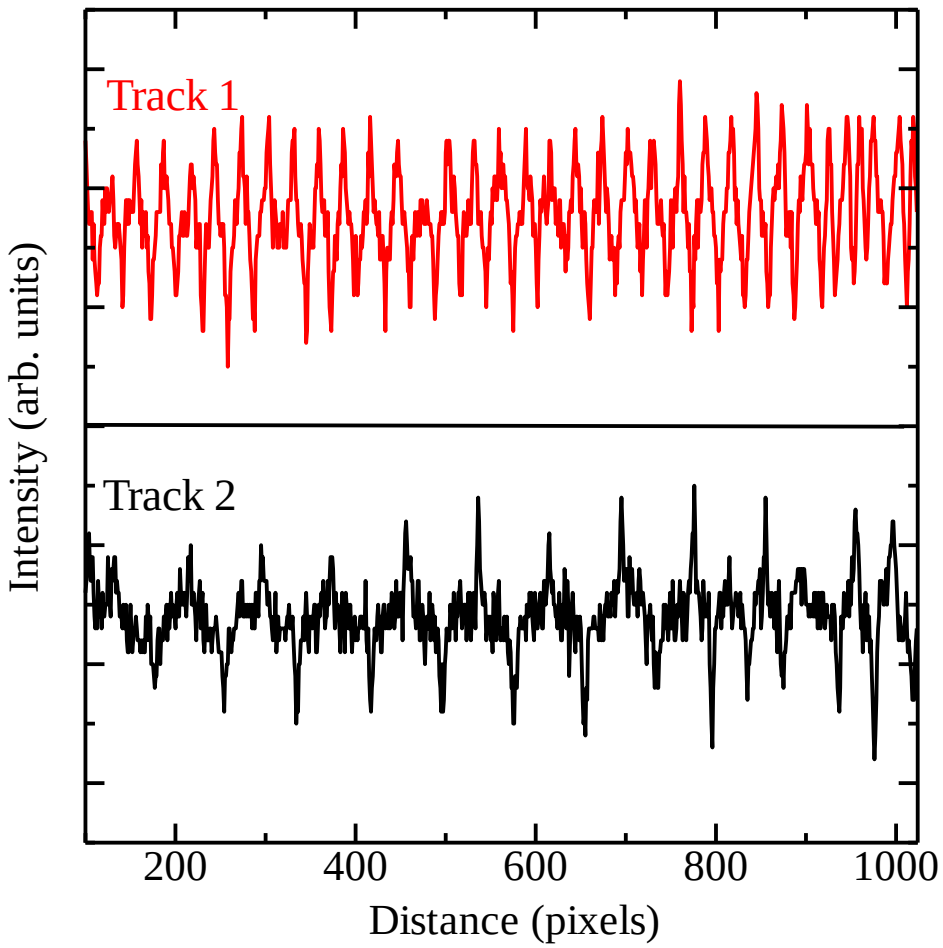

Figure 3.4.5. *Intensity of detected signal by CCD camera along the lines on Track 1 and Track 2. The difference of the information density can be clearly noticed.*

A beautiful representation of the dependence of magneto-optical image clarity on the FR angle of indicator film is given in Ref. [20] in Fig. 3.4.6. Fig. 3.4.6 shows the magneto-optical

images of magnetic domains of the same credit card using indicator films from low to high values of FR angle. All films were prepared by MOD method in our laboratory.

Thus the visualization of magnetic domains with high contrast becomes possible using indicator films prepared by MOD method. Results once again demonstrate that MOI is a method of choice for the quick and precise quality control of magnetic structures.

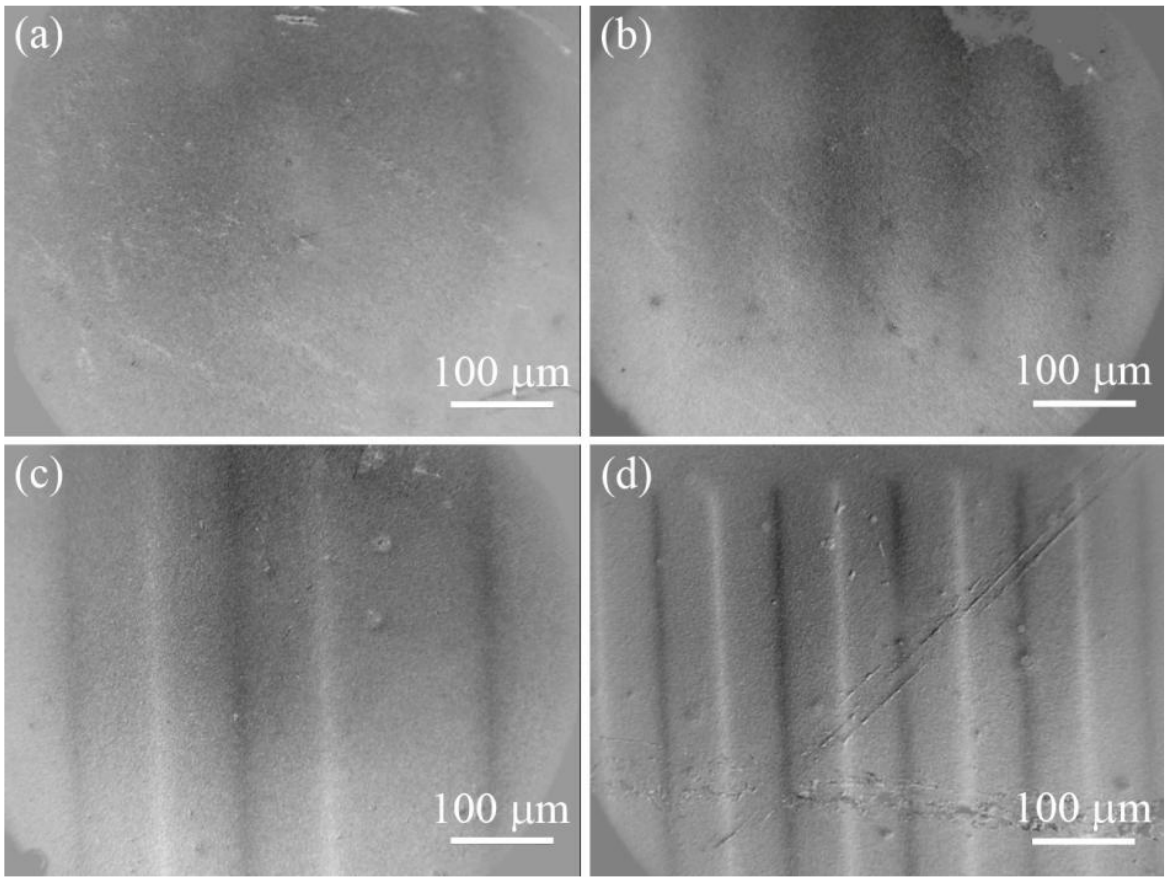

Figure 3.4.6. *Magneto-optical images of magnetic domains using (a) amorphous garnet film and films with FR angle values measured to be (b) -1°/μm; (c) -1.5 °/μm; (d) -2.5°/μm [20].*

§3.5. Magneto-optical visualization of electric currents

MOI technique was implemented for the nondestructive visualization of electric currents. Through the magnetic field created by the current it is possible to detect defects on microelectronic circuit boards. First as a SUT we used simple current wire. Fig. 4.5.1 shows the

current wire above the indicator film and magnetic field lines created around the wire. Incident linearly polarized light changes its polarization under the influence of the magnetic field.

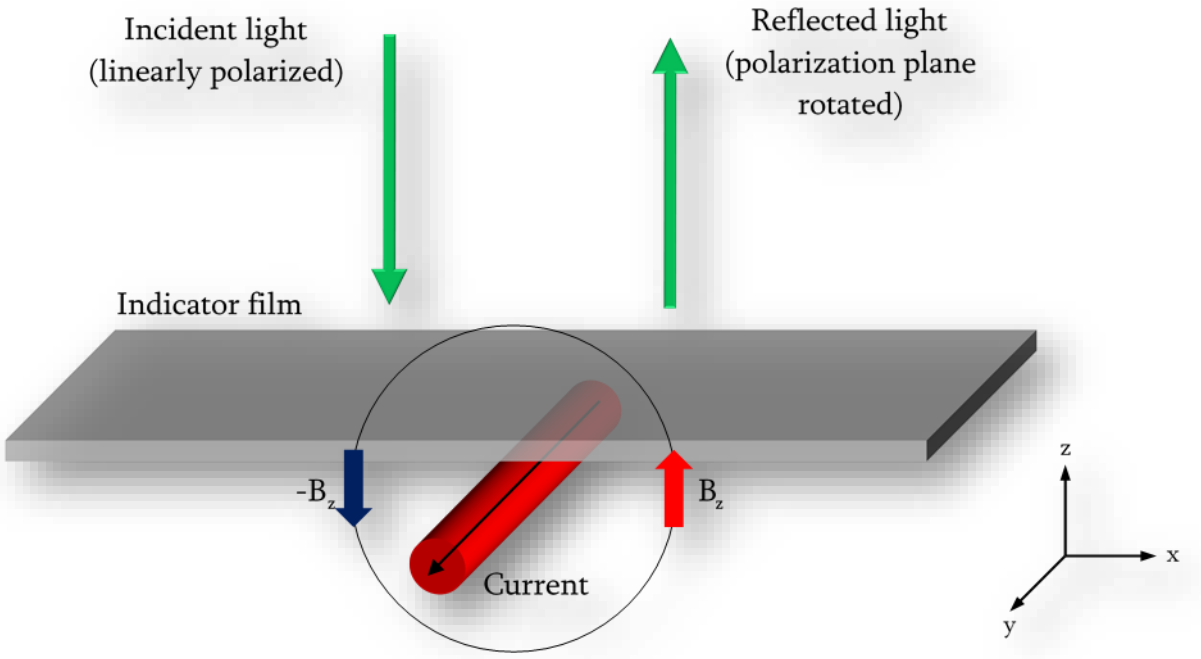

Figure 3.5.1. *The schematic diagram of the magneto-optical imaging of the electric current.*

Magnetic field induced from the infinitely long straight current wire with round shaped cross section can be represented by Ampere's law. Z-component of magnetic field B_z along the X-axis will be:

$$B_z(x) = B\cos(\alpha) = \frac{\mu_0 J}{2\pi} \cdot \frac{x}{x^2 + r^2} \cdot \tag{4.4.1}$$

where μ_0 is the permeability of free space $\left(\mu_0 = 4\pi \cdot 10^{-7}\ H/m\right)$, J and r are the current and the diameter of the wire respectively. Fig. 3.5.2 shows magneto-optical image of current wire with a 240 μm diameter and 1A current was applied to flow through the current using programmable power supply. Blue and red regions on the left and right sides of the wire represent opposite directions of B_z magnetic field created around the current wire. All magneto-optical images for current wires were obtained using a different imaging processing technique comparing to the method which was described for the imaging of magnetic domains. Thorough description of the

imaging technique and processing was done by the Sh. Arakelyan *et al.* and will be published in near future.

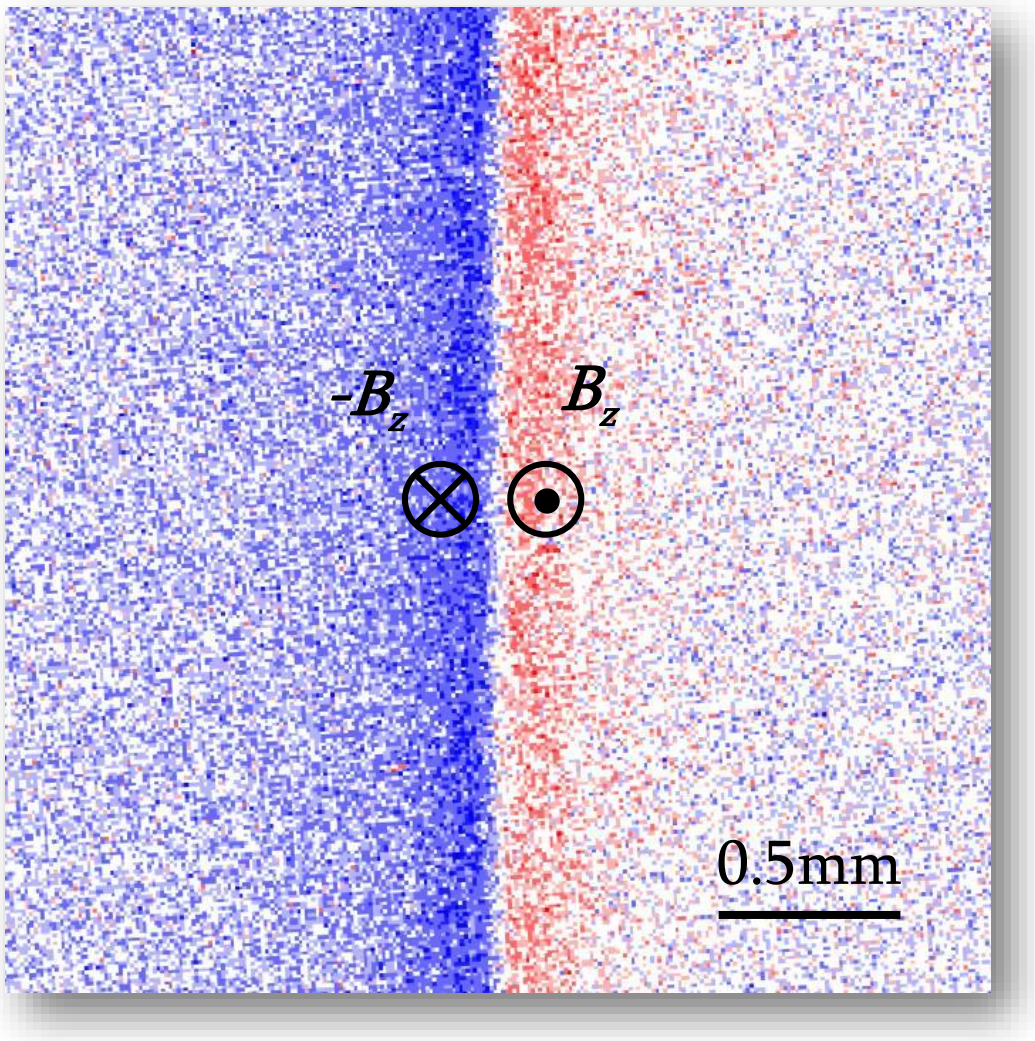

Figure 3.5.2. *Magneto-optical image of a current wire with 240 μm diamter carrying 1A current. Blue and red regions indicate two different directions of magnetic field created by a current wire which is the white region at the boundary of the blue and red regions.*

Fig. 3.5.3 shows the normalized magnetic field intensity distribution along the line shown in inset (which is miniaturized Fig. 3.5.2) for the experimental data (black line) and for the simulation data (red line) acquired using COMSOL Multiphysics simulator. We can clearly see the agreement of two kinds of data.

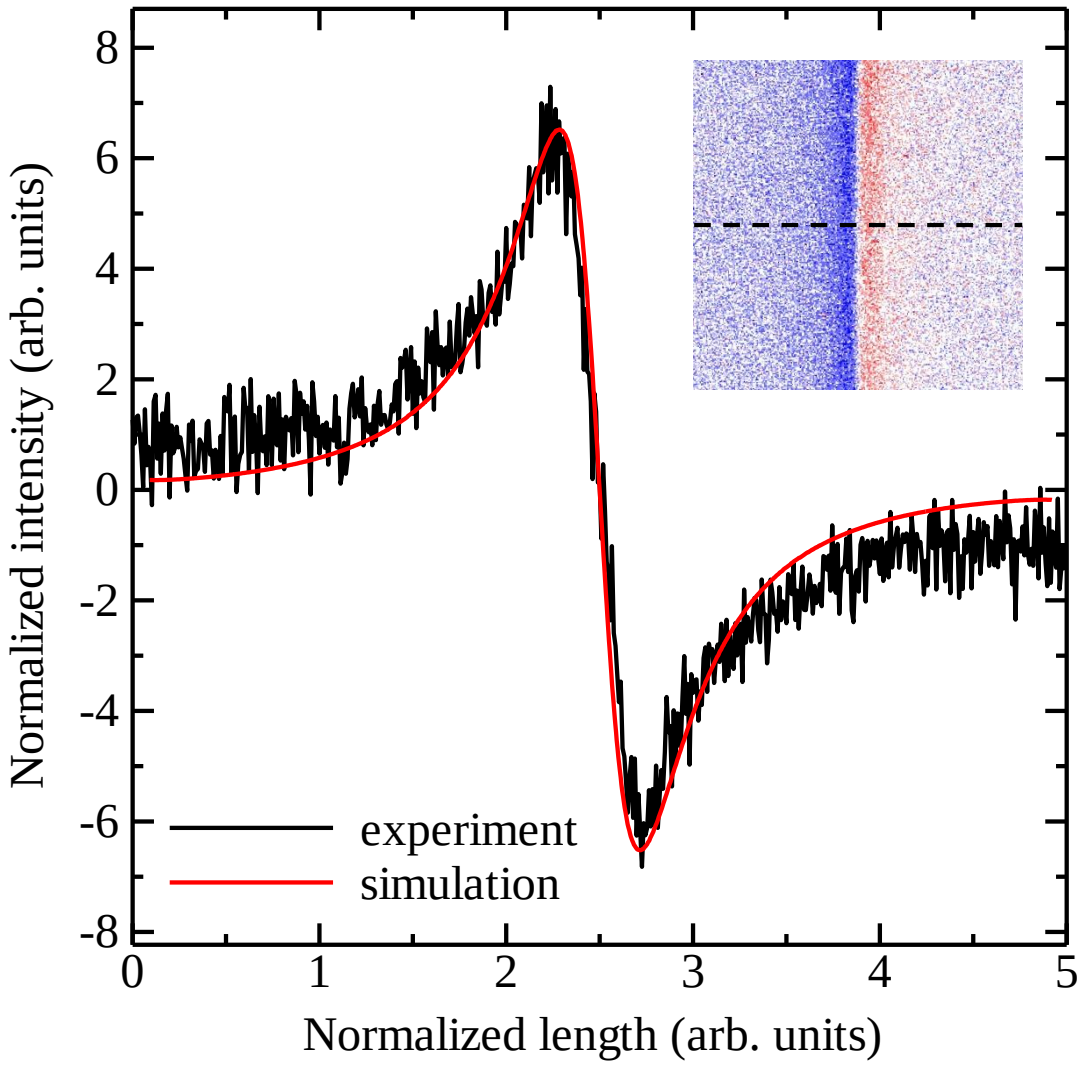

Figure 3.5.3. *Normalized magnetic field intensity along the indicated line on the inset. Red line shows the experimental data and black line simulation data. Inset shows the magneto-optical image from Fig. 3.5.2.*

Fig. 3.5.4 shows moving average of a normalized intensity of a magnetic field along the indicated line in Fig. 3.5.4 inset which shows magneto-optical image of a wire with 100 μm diameter and 32 mA flowing current. Using this data detected magnetic field was calculated to be (using eq. (4.4.1)) 0.6 Oe. This value of magnetic field is a minimum detectable magnetic field using our experimental setup.

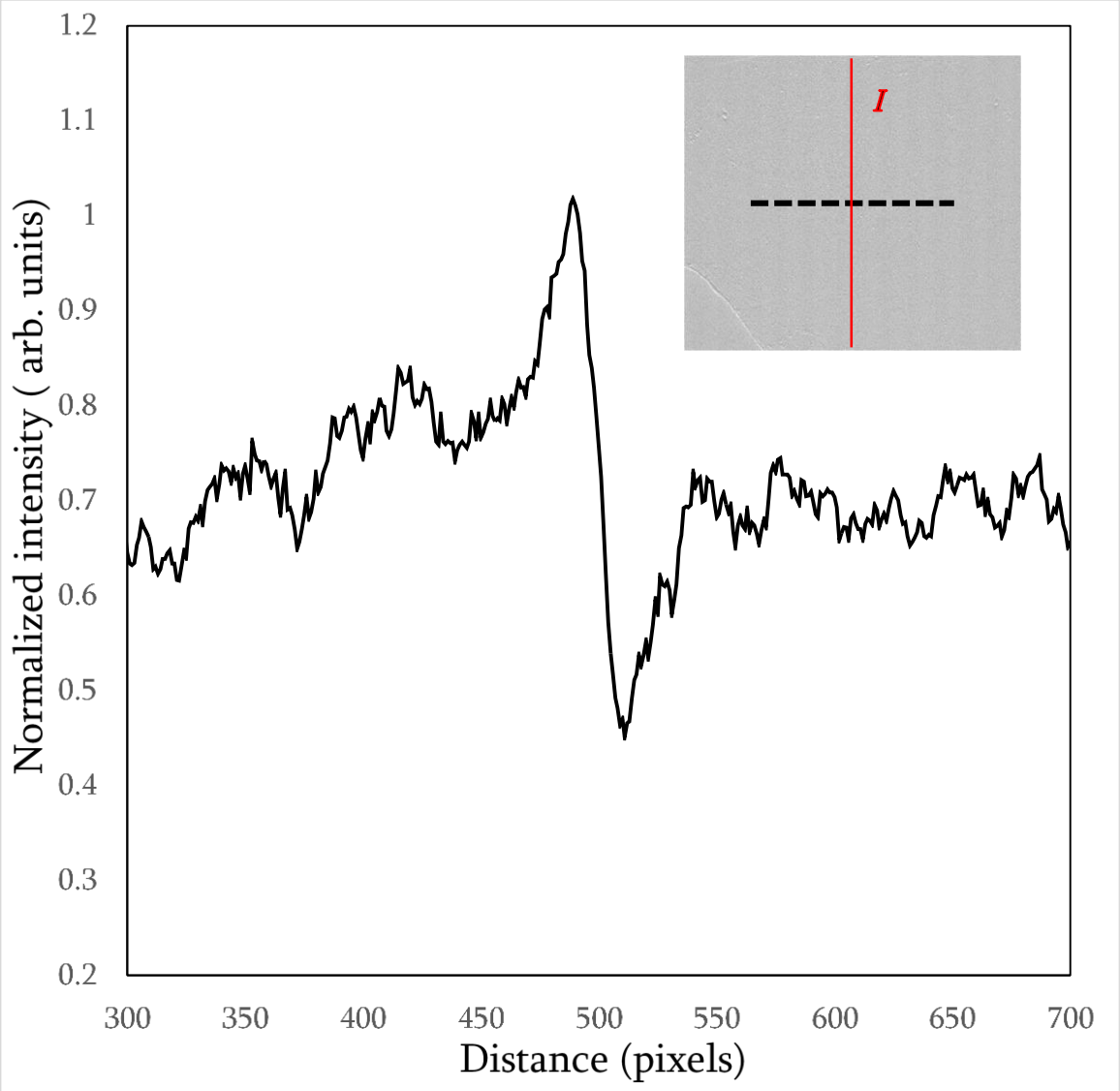

Figure 3.5.4. *Normalized magnetic field intensity along the indicated line on the inset. Inset shows magneto-optical image of a wire with 100 μm.*

Fig. 3.5.5 shows optical image of the printed circuit board (PCB) with an indicator thin film on it and magneto-optical image which clearly shows the local magnetic field distribution. Current was flowing through the wires which are indicated on Fig. 3.5.5 (a). This data shows that analysis of PCBs is possible using MOI technique.

The described MOI technique for current imaging gives the possibility for the designers and investigators of microelectronic devices to diagnose, design failures and determine local

current ranges. Such universal and low-cost setup, including the indicator film preparation, could be successfully used to express analysis of microelectronic circuits and devices.

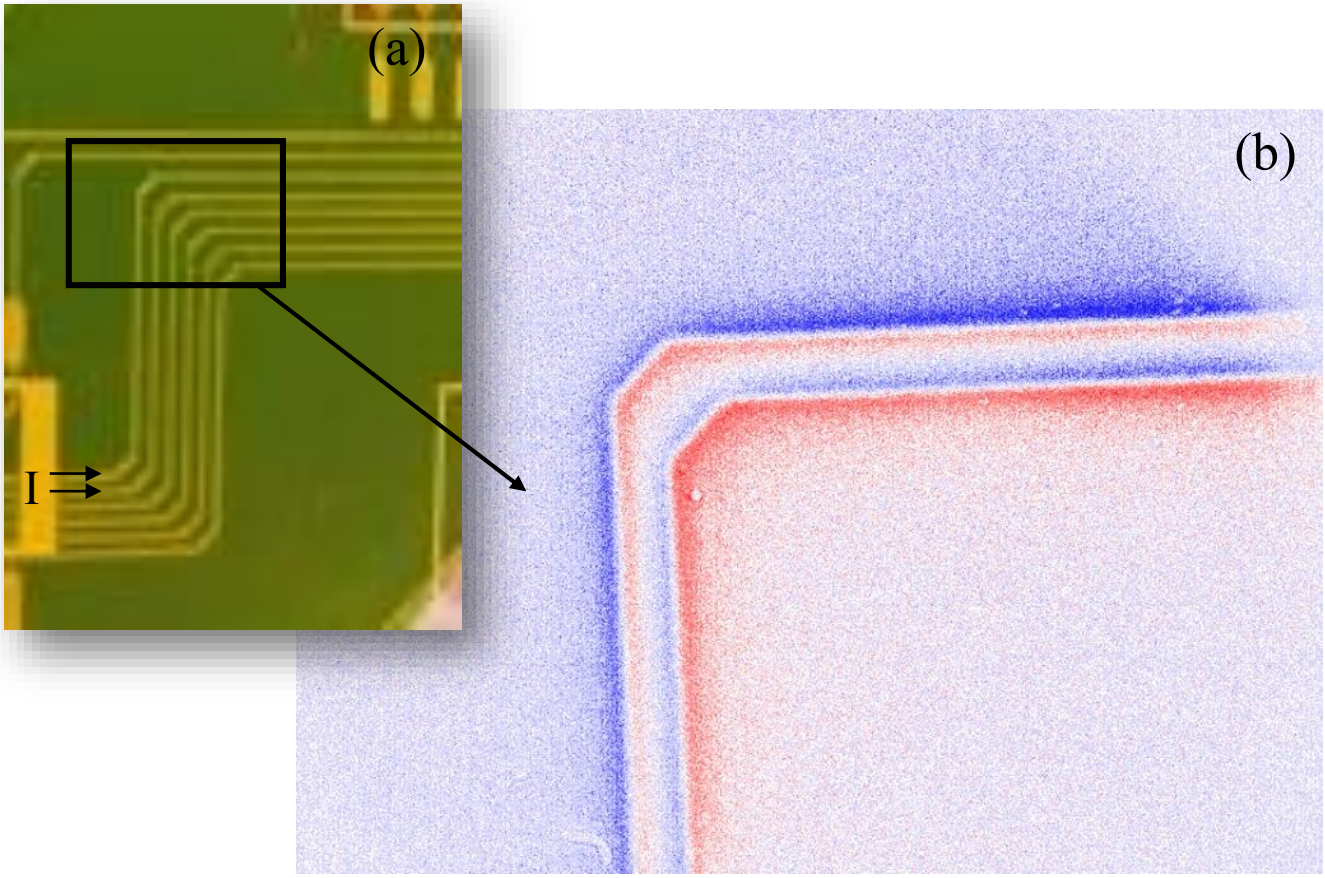

Figure 3.5.5. *(a) Photograph of the PCB with an indicator film on it, (b) magneto-optical image of the PCB. Blue and red regions on the magneto-optical image represents opposite directions of magnetic fields.*

CONCLUSION

The main obtained results in dissertation are the following:

- MOI setup which utilizes FE for the visualization of magnetic fields has been developed. Using our prepared indicator thin films with high FOM and in-plane magnetic anisotropy, the visualization of magnetic fields and magnetic domains becomes possible. Minimum detectable magnetic field was measured to be about 0.6 Oe and the spatial resolution of magneto-optical indicators prepared by MOD can achieve 0.5 μm. These results give the opportunity to use MOI for nondestructive monitoring applications where the magnetic fields visualization is required.
- After intensive studies on the preparation of Bi-YIG indicator thin films we succeed in the synthesis of films with high magneto-optical activity and low optical absorption. By improving the MOD heat treatment routine and adding the pre-crystallization step, high quality polycrystalline Bi-YIG thick films have been prepared. Pre-crystallization process enhances surface effects in the crystallization of thick films which makes it possible to fabricate thicker films using thin film preparation conditions.
- Using buffer layer deposition technique, Bi-YIG films with high levels of doped Bi have been fabricated on glass substrates. $Bi_xY_{3-x}Fe_5O_{12}$ (x=1) thin films which were prepared without buffer layer showed better crystallinity and magneto-optical activity using post-annealing temperatures for about 750 °C. While for the $Bi_xY_{3-x}Fe_5O_{12}$, x=2, 2.5) films a better quality was obtained by using lower 620 °C post-annealing temperatures.
- We prepared high concentration $Bi_xY_{3-x}Fe_5O_{12}$ (x=2) thin films with -11 °/μm FR angle on glass substrate without additional magnetic buffer layers, using 620-640 °C crystallization temperatures. To the best of our knowledge there are no publications on the preparation of MOD (x=2) $Bi_xY_{3-x}Fe_5O_{12}$ films with such FR values and post-annealing temperatures. Not only polycrystalline but also single crystalline $Bi_xY_{3-x}Fe_5O_{12}$ (x=2) thin films were prepared which have comparable crystalline characteristics with LPE-YIG films.

- For the first time we report on the possibility to prepare orthorhombic $YFeO_3$ thin films (by MOD method) at 750 °C post-annealing temperature by increasing concentration of substituted bismuth, particularly for the samples $Bi_xY_{1-x}FeO_3$ (x=0.3 and x=0.4). Films with strong hexagonal phase of $YFeO_3$ were obtained for $Bi_xY_{1-x}FeO_3$ (x=0) samples, so as a result, the selective crystallization of an o-$YFeO_3$ or h-$YFeO_3$ phases can be obtained by adjusting the level of Bi substitution.

LIST OF ABBREVIATIONS

Abbreviation	-	Meaning
BIG	-	Bismuth iron garnet
Bi-YIG	-	bismuth substituted yttrium iron garnet
CSD	-	chemical solution deposition
DC	-	direct current
FE	-	Faraday effect
FMR	-	ferromagnetic resonance
FR	-	Faraday rotation
FOM	-	figure of merit
FWHM	-	full width half maximum
GGG	-	gadolinium gallium garnet
IFE	-	Inverse Faraday effect
LCP	-	left circularly polarized light
LPE	-	liquid phase epitaxy
MFM	-	magnetic force microscopy
MOI	-	magneto-optical imaging
MOCVD	-	metal-organic chemical vapor deposition
MOD	-	metal-organic decomposition
PCB	-	printed circuit board
PLD	-	pulsed laser deposition
RCP	-	right circularly polarized light
SUT	-	specimen under test
SQUID	-	superconducting quantum interface device

UV-vis	-	ultraviolet-visible
VSM	-	vibrating sample magnetometer
XRD	-	x-ray diffractometry
YIG	-	yttrium iron garnet

ACKNOWLEDGEMENTS

This work would not have been possible without the time, support and dedication of many people who were involved in this research over the past three years. I want to express my sincere gratitude to my supervisor Arsen Hakhoumian. You have critically and encouragingly supported my academic development over the past few years and lighten my way to the professional career. I am also grateful to my supervisor Professor Kiejin Lee who supported my research and accommodation in Korea where I did most of my experiments and research. I am extremely thankful to Hanju Lee and Arsen Babajanyan for sharing expertise, valuable guidance and encouragement. I also want to express my gratitude to my friends: Jongwon Park, Yeonsop Lee and Shant Arakelyan, who helped me a lot during my research. Special thanks goes to my family and all my friends for the warmth and support during my PhD studies.

REFERENCES

1. M. Faraday, “Faraday’s diary of experimental investigation”, HR Direct, USA, 2008
2. U. Hartmann, “Magnetic Force Microscopy”, Rev. Mater. Sci., 29, 1999, pp. 53-87
3. J. R. Kirtley, “SQUID microscopy for fundamental studies”, Physica C, 368, 2002, pp. 55-65
4. E. Ramsden, “Hall-effect sensors: theory and application”, Newnes, 2011.
5. P. P. Freitas, R. Ferreira, S. Cardoso, F. Cardoso. "Magnetoresistive sensors." Journal of Physics: Condensed Matter 19, no. 16, 2007, 165221.
6. A. N. Egorov, S. V. Lebedev, “Magneto-optical observation of surface currents in microelectronic circuits”, J. Appl. Phys. 87, 2000, pp. 5362-5364.
7. M. Grechishkin, M.Yu. Goosev, S.E. Ilyashenko, N.S. Neustroev “High-resolution sensitive magneto-optic ferrite-garnet films with planar anisotropy”, J. Magn. Magn. Mater. 157, 1996, pp. 305-306
8. Y. H Cheng, Z. F. Zhou, G. Y. Tian, “Enhanced magneto-optic imaging system for nondestructive evaluation, NDT&E INT 40, 2007, pp. 374-377.
9. S. Kahl, A. M. Grishin, S. I. Khartsev, K. Kawano, J. S. Abell, “Bi3Fe5O12 Thin Film Visualizer”, IEEE Trans. Magn. 3, 2001, pp. 2457-2459.
10. S. A. Crooker, M. Furis, X. Lou, C. Adelmann, D. L. Smith, C. J. Palmstrøm, P. A. Crowell, “Imaging Spin Transport in Lateral Ferromagnet/Semiconductor Structures”, Science 300, 2005, pp. 2191-2195.
11. Y. K. Kato, R. C. Myers, A. C. Gossard, D. D. Awschalom, “Observation of the spin hall effect in semiconductors”, Science 306, 2004, pp. 1910-1913.
12. Aichele, T., A. Lorenz, R. Hergt, P. Görnert. "Garnet layers prepared by liquid phase epitaxy for microwave and magneto-optical applications–a review." Crystal Research and Technology 38, no. 7-8, 2003, pp. 575-587.
13. Sung, S. Y., Qi, X., Stadler, B. J. (2005). Integrating yttrium iron garnet onto nongarnet substrates with faster deposition rates and high reliability. Applied Physics Letters, 87, 12, 121111.
14. T. Tepper, C.A. Ross, “Pulsed laser deposition and refractive index measurement of fully substituted bismuth iron garnet films” J. Cryst. Growth 255, 2003, pp. 324-331.

15. Matsumoto, K., K. Yamaguchi, T. Fujii. “Synthesis of YIG and Bi-substituted YIG by Sol-Gel method and magnetooptical properties of spin-coated thin films”, Magnetics in Japan, IEEE Translation Journal on 6.7, 1991, pp. 614-623.
16. M. Okada, S. Katayama, K. Tominaga, “Preparation and magneto-optic properties of Bi-substituted yttrium iron garnet thin MOCVD”, J. Appl. Phys. 69, 1991, pp. 3566-3570.
17. A. Azevedo, S. Bharthulwar, W. Eppler, M. Kryder, “Deposition of Garnet thin Films by Metallo-organic decomposition method (MOD)”, IEEE Trans. Magn. 30, 1994, pp. 4416-4418.
18. Shoji, Y., Mizumoto, T., Yokoi, H., Hsieh, I. W., Osgood Jr, R. M., “Magneto-optical isolator with silicon waveguides fabricated by direct bonding”, Applied Physics Letters, 92(7), 2008, 071117.
19. S. Wittekoek, T. Popma, J. Robertson, P. Bongers, “Magneto-optic spectra and the dielectric tensor elements of bismuth-substituted iron garnets at photon energies between 2.2-5.2 eV.”, Physical review B 12, no. 7, 1975, pp. 2777-2788.
20. H. Lee, T. Kim, S.Kim, Y. Yoon, S. Kim, A. Babajanyan, T. Ishibashi, B. Friedman, K. Lee. "Magneto-optical imaging using a garnet indicator film prepared on glass substrates." Journal of Magnetism and Magnetic Materials 322, no. 18 (2010), pp. 2722-2727.
21. A. V. Kimel, A. Kirilyuk, P. A. Usachev, R. V. Pisarev, A. M. Balbashov, Th. Rasing, “Ultrafast non-thermal control of magnetization by instantaneous photomagnetic pulses”, Nature 435, 2005, pp. 655-657
22. S. Kahl, “Bismuth iron garnet films for magneto-optical photnic crystals”, Doctoral Dissertation, Royal Institute of Technology, Stockholm (2004).
23. О.А. Котельникова, Н.С. Перов, Шапаева Т.Б., Е.Е. Шалыгина “Эффект фарадея в ферритах в диапазоне СВЧ”, Спецпрактикум кафедры магнетизма МГУ, Москва (2013).
24. A. R. Taussig, “Growth and characterization of bismuth pervskite thin films for integrated magneto-optical isolator applications”, A. B. Physics, Harvard University (2005).
25. G. F. Dionne, G. A. Allen, P. R. Haddad, C. A. Ross, B. Lax, “Circular Polarization and Nonreciprocal Propagation in Magnetic Media” LLABJ 15, 2005, pp. 323-340
26. Zvezdin, A. K., & Kotov, V. A.. Modern magnetooptics and magnetooptical materials. (1997) CRC Press.

27. G. F. Dionne, G. A. Allen, “Spectral origins of giant Faraday rotation and ellipticity in Bi-substituted magnetic garnets”, Journal of Applied Physics, 73(10), 1993 pp. 6127-6129.
28. M. A. Gilleo, S. Geller. “Magnetic and Crystallographic Properties of Substituted Yttrium-Iron Garnet, 3 Y 2 O 3· x M 2 O 3·(5-x) Fe 2 O 3.” Physical Review 110.1 (1958), p. 73-78.
29. Geller, S., and M. A. Gilleo. "The crystal structure and ferrimagnetism of yttrium-iron garnet, Y 3 Fe 2 (FeO 4) 3." Journal of Physics and Chemistry of Solids 3.1, 1957, 30-36.
30. B. Lei, J. Hu, L. Kimerling, C. A. Ross. “Fabrication and characterization of As2S3/Y3Fe5O12 and Y3Fe5O12/SOI strip-loaded waveguides for integrated optical isolator applications.” In OPTO, International Society for Optics and Photonics, 2010, p. 760406.
31. Paroli, P. "Magneto-optical devices based on garnet films." Thin Solid Films114, no. 1, 1984, 187-219.
32. Y. Shoji, T. Mizumoto, H. Yokoi, I. W. Hsieh, R. M. Osgood Jr, Magneto-optical isolator with silicon waveguides fabricated by direct bonding. Applied Physics Letters, 92(7), 2008 071117.
33. H. Hayashi, S. Iwasa, N. J. Vasa, T. Yoshitake, K. Ueda, S. Yokoyama, S. Higuchi, H. Takeshita, M. Nakahara. "Fabrication of Bi-doped YIG optical thin film for electric current sensor by pulsed laser deposition." Applied surface science 197, 2002, pp. 463-466.
34. S. H. Wemple, S. L. Blank, J. A. Seman, W. A. Biolsi. "Optical properties of epitaxial iron garnet thin films." Physical Review B 9, no. 5, 1974, pp. 2134.
35. S. Geller, “Magnetic Behavior of Substituted Ferrimagnetic Garnets”, Journal of Applied Physics 37, 3, 1966, 1408-1415.
36. P. Hansen, W. Tolksdorf, R. Krishnan. "Anisotropy and magnetostriction of cobalt-substituted yttrium iron garnet." Physical Review B 16.9, 1977, pp. 3973-3986
37. P. Hansen, K. Witter, "Magneto-optical properties of gallium-substituted yttrium iron garnets." Physical Review B 27, 3, 1983, pp. 1498-1506.
38. P. Hansen, J. Schuldt, W. Tolksdorf. "Anisotropy and magnetostriction of iridium-substituted yttrium iron garnet." Physical Review B 8, 9, (1973), pp. 4274-4287.
39. C. F. Buhrer, "Faraday rotation and dichroism of bismuth calcium vanadium iron garnet." Journal of Applied Physics 40, 11, 1969 pp. 4500-4502.

40. P. Hansen, K. Witter, Tolksdorf. "Magnetic and magneto-optic properties of bismuth-and aluminum-substituted iron garnet films." Journal of Applied Physics 55, 4, 1984, pp. 1052-1061.
41. M. Laulajainen, P. Paturi, J. Raittila, H. Huhtinen, A. B. Abrahamsen, N. H. Andersen, and R. Liho. "BixY3– xFe5O12 thin films prepared by laser ablation for magneto-optical imaging of superconducting thin films." Journal of Magnetism and Magnetic Materials 279, no. 2, 2004, pp. 218-223.
42. A. A. Serga, A. V. Chumak, B. Hillebrands. "YIG magnonics." Journal of Physics D: Applied Physics 43, 26, 2010, 264002.
43. I. Žutić, , H. Dery. "Spintronics: Taming spin currents." Nature materials 10, 9, 2011, pp. 647-648.
44. WS Ishak, KW Chang. "Tunable microwave resonators using magnetostatic wave in YIG films." Microwave Theory and Techniques, IEEE Transactions on 34, no. 12, 1986, pp. 1383-1393.
45. G. Qiu, CS Tsai, Bert ST Wang, Yun Zhu. "A YIG/GGG/GaAs-based magnetically tunable wideband microwave band-pass filter using cascaded band-stop filters." Magnetics, IEEE Transactions on 44, no. 11, 2008, pp. 3123-3126.
46. S. M. Gillette, A. L. Geiler, Z. Chen, Y. Chen, T. Arruda, C. Xie, L. Wang et al. "Active tuning of a microstrip hairpin-line microwave bandpass filter on a polycrystalline yttrium iron garnet substrate using small magnetic fields."Journal of Applied Physics 109, no. 7, 2011, 07A513.
47. X. Yang, J. Wu, S. Beguhn, T. Nan, Y. Gao, Z. Zhou, N. X. Sun. "Tunable bandpass filter using partially magnetized ferrites with high power handling capability." Microwave and Wireless Components Letters, IEEE 23, no. 4, 2013, pp. 184-186.
48. R. C. Linares, "Epitaxial growth of narrow linewidth yttrium iron garnet films." Journal of Crystal Growth 3, 1968, pp. 443-446.
49. T. Ishibashi, T.Yoshida, T. Kobayashi, S. Ikehara, T. Nishi. "Preparation of Y0. 5Bi2. 5Fe5O12 films on glass substrates using magnetic iron garnet buffer layers by metal-organic decomposition method." Journal of Applied Physics 113, no. 17, 2013, 17A926.

50. R. Hergt, H. Pfeiffer, P. Görnert, M. Wendt, B. Keszei, and J. Vandlik. "Kinetic segregation of lead impurities in garnet LPE films." Physica status solidi (a), 104, no. 2, 1987, pp. 769-776.
51. H. M. Smith, A. F. Turner. "Vacuum deposited thin films using a ruby laser." Applied Optics 4, no. 1, 1965, pp. 147-148.
52. D. Dijkkamp, T. Venkatesan, X. D. Wu, S. A. Shaheen, N. Jisrawi, Y. H. Min-Lee, W. L. McLean, M. Croft. "Preparation of Y-Ba-Cu oxide superconductor thin films using pulsed laser evaporation from high Tc bulk material." Applied Physics Letters 51, no. 8, 1987, pp. 619-621.
53. T. Wehlus, T. Körner, S. Leitenmeier, A. Heinrich, B. Stritzker. "Magneto-optical garnets for integrated optoelectronic devices." physica status solidi (a) 208, no. 2, 2011, pp. 252-263.
54. Young-Min Kang, Sung-Hun Wee, Seong-Il Baik, Seong-Gi Min, Seong-Cho Yu, Seung-Hyun Moon, Young-Woon Kim, Sang-Im Yoo. "Magnetic properties of YIG (Y 3 Fe 5 O 12) thin films prepared by the post annealing of amorphous films deposited by rf-magnetron sputtering." Journal of applied physics 97, 10, 2005, 10A319.
55. T. Körner, A.Heinrich, M. Weckerle, P. Roocks, B. Stritzker. "Integration of magneto-optical active bismuth iron garnet on nongarnet substrates." Journal of Applied Physics 103, 7, 2008, 07B337.
56. H. Lee, , Y. Yoon, S. Kim, H. K. Yoo, H. Melikyan, E. Danielyan, A. Babajanyan, T. Ishibashi, B. Friedman, K. Lee. "Preparation of bismuth substituted yttrium iron garnet powder and thin film by the metal-organic decomposition method." Journal of Crystal Growth 329, 1, 2011, pp. 27-32.
57. H. Lee, Y. Yoon, H. Yoo, S. A. Choi, K. Kim, Y. Choi, H. Melikyan, T. Ishibashi, B. Friedman, K. Lee. "Magnetic and FTIR studies of Bi x Y 3– x Fe 5 O 12 (x= 0, 1, 2) powders prepared by the metal organic decomposition method." Journal of Alloys and Compounds 509, 39, 2011, pp. 9434-9440.
58. O. Galstyan, H. Lee, S. Lee, N. Yoo, J. Park, A. Babajanyan, B. Friedman, K. Lee. "Effect of pre-crystallization on the preparation of thick Bi-YIG films by the metal–organic decomposition method." Journal of Magnetism and Magnetic Materials 366, 2014, pp. 24-27.

59. R. Lux, A. Heinrich, S. Leitenmeier, T. Körner, M. Herbort, B. Stritzker. "Pulsed-laser deposition and growth studies of Bi3Fe5O12 thin films." Journal of Applied Physics 100, 11, 2006, 113511.
60. EHG Backus, M. Bonn. "Theory of bulk, surface and interface phase transition kinetics in thin films." The Journal of chemical physics 121, 2, 2004, pp. 1038-1049.
61. R. W. Schwartz, T. Schneller, R Waser, "Chemical solution deposition of electronic oxide films. Comptes Rendus Chimie", 7, 5, 2004, pp. 433-461.
62. D. S. Schmool, N. Keller, M. Guyot, R. Krishnan, M. Tessier. "Magnetic and magneto-optic properties of orthoferrite thin films grown by pulsed-laser deposition." Journal of applied physics 86, 10, 1999, pp. 5712-5717.
63. K. Matsumoto, S. Sasaki, Y. Asahara, K. Yamaguchi, T. Fujii. "Highly bismuth substituted yttrium iron garnet single crystal films prepared by sol-gel method." Journal of Magnetism and Magnetic Materials 104, 1992, pp. 451-452.
64. O. Galstyan, "Dependence of Magneto-Optical Properties of Bi-YIG Thin Films on Post-Annealing Temperature", Armenian Journal of Physics, Vol. 8, no. 1, 2015, pp. 21-29.
65. Gomi, M., K. Utsugi, and M. Abe. "RF sputtered films of Bi-substituted garnet for magneto-optical memory." Magnetics, IEEE Transactions on 22, no. 5, 1986, pp. 1233-1235.
66. Roumie, M., B. Abdel Samad, M. Tabbal, M. Abi-Akl, M-F. Blanc-Mignon, and B. Nsouli. "Effect of deposition temperature on the properties of sputtered YIG films grown on quartz." Materials Chemistry and Physics 124, no. 1, 2010, pp. 188-191.
67. Grechishkin, R. M., M. Yu Goosev, S. E. Ilyashenko, and N. S. Neustroev. "High-resolution sensitive magneto-optic ferrite-garnet films with planar anisotropy."Journal of magnetism and magnetic materials 157, 1996, pp. 305-306.
68. Adachi, Nobuyasu, and Toshitaka Ota. "Crystallinity and magnetic properties of Bi 3 Fe 5 O 12 thick film prepared by MOD technique." Journal of the Ceramic Society of Japan 122, no. 1421, 2014, pp. 40-43.
69. Kaewkhao, J., W. Siriprom, S. Insiripong, T. Ratana, C. Kedkaew, and P. Limsuwan. "Structural and magnetic properties of glass doped with iron oxide." In Journal of Physics: Conference Series, vol. 266, no. 1, p. 012012. IOP Publishing, 2011.

70. O. Galstyan, H. Lee, S. Lee, N. Yoo, J. Park, A. Babajanyan, B. Friedman, K. Lee, "Influence of bismuth substitution on yttrium orthoferrite thin films preparation by the MOD method" Journal of Magnetism and Magnetic Materials, UNDER REVIEW
71. Maiti, Ramaprasad, Soumen Basu, and Dipankar Chakravorty. "Synthesis of nanocrystalline YFeO 3 and its magnetic properties." Journal of Magnetism and Magnetic Materials 321, no. 19, 2009, pp. 3274-3277.
72. Kahn, Frederic J., P. S. Pershan, and J. P. Remeika. "Ultraviolet magneto-optical properties of single-crystal orthoferrites, garnets, and other ferric oxide compounds." Physical review 186, no. 3, 1969, 891.
73. Didosyan, Yuri S., Hans Hauser, Holger Wolfmayr, Johann Nicolics, and P. Fulmek. "Magneto-optical rotational speed sensor." Sensors and Actuators A: Physical 106, no. 1, 2003, pp. 168-171.
74. Didosyan, Yuri S., V. Y. Barash, N. A. Bovarin, Hans Hauser, and Paul Fulmek. "Magnetic field sensor by orthoferrites." Sensors and Actuators A: Physical 59, no. 1 (1997): 56-60.
75. Didosyan, Yuri S., Hans Hauser, and Georg A. Reider. "Magnetooptic switch based on domain wall motion in orthoferrites." IEEE transactions on magnetics 38, no. 5, 2002, pp. 3243-3245.
76. Medek, R., J. Nicolics, and H. Hauser. "Recent Progresses on the Development of an Yttrium Orthoferrite Based Optical Switch." In Electronics Technology, 30th International Spring Seminar on IEEE, 2007, pp. 361-366.
77. Lü, Xiaomeng, Jimin Xie, Huoming Shu, Jun Liu, Changqing Yin, and Jiamin Lin. "Microwave-assisted synthesis of nanocrystalline YFeO3 and study of its photoactivity." Materials Science and Engineering: B 138, no. 3, 2007, pp. 289-292.
78. S. Mathur, M. Veith, R. Rapalaviciute, H. Shen, G. F. Goya, W. L. M. Filho, T. S. Berquo. "Molecule derived synthesis of nanocrystalline YFeO3 and investigations on its weak ferromagnetic behavior." Chemistry of materials 16, 10, 2004, pp. 1906-1913.
79. L. Wu, C. Yu Jimmy, L. Zhang, X. Wang, S. Li. "Selective self-propagating combustion synthesis of hexagonal and orthorhombic nanocrystalline yttrium iron oxide." Journal of Solid State Chemistry 177, 10, 2004, pp. 3666-3674.

80. Wood, D. L., J. P. Remeika, and E. D. Kolb. "Optical spectra of rare-earth orthoferrites." Journal of Applied Physics 41, no. 13, 1970, pp. 5315-5322.
81. Tabor, W. J., A. W. Anderson, and L. G. Van Uitert. "Visible and Infrared Faraday Rotation and Birefringence of Single-Crystal Rare-Earth Orthoferrites." Journal of Applied Physics 41, no. 7, 1970, 3018-3021.
82. Buscaglia, V., F. Caracciolo, C. Bottino, M. Leoni, and P. Nanni. "Reaction diffusion in the Y 2 O 3-Fe 2 O 3 system." Acta materialia 45, no. 3, 1997, 1213-1224.
83. Gil, Diego M., M. Carolina Navarro, M. Cristina Lagarrigue, J. Guimpel, Raúl E. Carbonio, and M. Inés Gómez. "Synthesis and structural characterization of perovskite YFeO 3 by thermal decomposition of a cyano complex precursor, Y [Fe (CN) 6]· 4H 2 O." Journal of thermal analysis and calorimetry 103, no. 3, 2011, pp. 889-896.
84. R. Krishnan, A. Lisfi, M. Guyot, V. Cagan," Preparation and some properties of pulsed laser deposited YFeO3 films." J. Magn. Magn. Mater. 147, 1995, L221.
85. D. S. Schmool, N. Keller, M. Guyot, R. Krishnan, M. Tessier. "Magnetic and magneto-optic properties of orthoferrite thin films grown by pulsed-laser deposition." Journal of applied physics 86, 10, 1999, pp. 5712-5717.
86. Y. Zhang, J. Yang, J. Xu, Q. Gao, Z. Hong. "Controllable synthesis of hexagonal and orthorhombic YFeO 3 and their visible-light photocatalytic activities." Materials Letters 81 2012, pp. 1-4.
87. N. Kaiser, "Review of the fundamentals of thin-film growth." Applied optics 41, 16, 2002, pp. 3053-3060.
88. T. Ishibashi, Z. Kuang, S. Yufune, T. Kawata, M. Oda, T. Tani, Y. Iimura, K. Sato, Y. Konishi, K. Akahane, X. Zhao, T. Hasegawa. "Magneto-optical imaging using polarization modulation method." Journal of applied physics 100, 9, 2006, p. 093903.
89. H. Lee, "Research on the visualization of magnetic field and temperature by optical indicator technique", PhD thesis, Sogang University, Korea, 2014
90. L. A. Knauss, S. I. Woods, A. Orozco. "Current imaging using magnetic field sensors." Microelectronics Failure Analysis Desk Reference 5, 2004, pp. 303-311.
91. M. I. D'yakonov, V. I. Perel. "Possibility of orienting electron spins with current." Soviet Journal of Experimental and Theoretical Physics Letters 13, 1971, p. 467.

92. G. L. Fitzpatrick, D. K. Thome, R. L. Skaugset, W. C. L. Shih. "Magneto-optic/Eddy current imaging of subsurface corrosion and fatigue cracks in aging aircraft." In Review of progress in quantitative nondestructive evaluation, Springer US, 1996, pp. 1159-1166.
93. Y. Deng, Xin Liu, Yuan Fan, Zhiwei Zeng, Lalita Udpa, and William Shih. "Characterization of magneto-optic imaging data for aircraft inspection." Magnetics, IEEE Transactions on 42, 10, 2006, pp. 3228-3230.
94. Ch. Jooss, J. Albrecht, H. Kuhn, S. Leonhardt, H. Kronmüller. "Magneto-optical studies of current distributions in high-Tc superconductors." Reports on progress in Physics 65, 5, 2002, p. 651.
95. P.E. Goa, H. Hauglin, M. Baziljevich, E. Il'yashenko, P. L. Gammel, T. H. Johansen. "Real-time magneto-optical imaging of vortices in superconducting NbSe2." Superconductor Science and Technology 14, 9, 2001, p. 729.
96. M. R. Koblischka, R. J. Wijngaarden "Magneto-optical investigations of superconductors." Superconductor Science and Technology 8, 4, 1995, p. 199.
97. T. H. Johansen, M. Baziljevich, H. Bratsberg, Y. Galperin, P. E. Lindelof, Y. Shen, and P. Vase. "Direct observation of the current distribution in thin superconducting strips using magneto-optic imaging." Physical Review B 54, 22, 1996, p. 16264.
98. Goa, P. E., H. Hauglin, Å. AF Olsen, M. Baziljevich, T. H. Johansen. "Magneto-optical imaging setup for single vortex observation." Review of scientific instruments 74, 1, 2003, pp. 141-146.
99. M. Takahashi, K. Kawasaki, H. Ohba, T. Ikenaga, H. Ota, T. Orikasa, N. Adachi, K. Ishiyama, K. I. Arai. "Electromagnetic near field measurements by using magnet garnet crystal." Journal of Applied Physics 107, 9, 2010, 09E711.
100. O. Galstyan, H. Lee, A. Babajanyan, A. Hakhoumian, B. Friedman, K. Lee. "Magneto-optical visualization by Bi: YIG thin films prepared at low temperatures." Journal of Applied Physics 117, 16, 2015, p. 163914.